



Universität  
Rostock



Universitätsmedizin  
Rostock

# Establishment of a Human 3D Kidney Tissue Model Using Decellularized Rat Kidney Slices

A dissertation submitted by

Haitham Salti

*In fulfillment of the requirements for the degree of  
Doctor of Medical Sciences (Dr. rer. hum.)*

University of Rostock  
Rostock University Medical Center  
Department of Internal Medicine  
Division of Nephrology  
Director: Prof. Dr. med. Steffen Mitzner

Rostock, 04.01.2024

Advisors:

1. Prof Dr. med. Steffen Mitzner, Division of Nephrology, Department of Internal Medicine, Rostock University Medical Center
2. PD Dr. Kirsten Peters, Institute of Cell Biology, Center for Medical Research (ZEMFO), University Medicine Rostock
3. Prof. Dr. med. Kerstin Amann, Department of Nephropathology, Universitätsklinikum Erlangen, Friedrich-Alexander University Erlangen-Nürnberg (FAU)

Date of submission: 05.01.2024

Date of defense: 12.11.2024

This research project is part of the HOGEMA consortium and supported by the European Social Fund (ESF), reference: ESF/14-BM-A55-0014/18, and the Ministry of Education, Science and Culture of Mecklenburg-Vorpommern, Germany

## **For my parents**

For their unwavering support and endless encouragement, without which this journey would not have been possible

## Summary

The global rise in chronic kidney disease underscores the pressing need for innovative treatments for end-stage renal disease (ESRD) beyond transplantation and dialysis. The use of tissue engineering to develop bioartificial kidneys may offer an alternative path. The extracellular matrix (ECM) obtained by decellularization provides scaffolds with the natural complex architecture of the target organ. However, whole kidney de- and recellularization by perfusion are highly complex processes that require intensive optimization of various parameters. Precision-cut kidney slices (PCKS) were utilized as a source of natural scaffolds. Since chemical reagents have a damaging effect on the ECM, this study aimed to investigate the impact of physical treatments on the efficacy of PCKS immersion decellularization (PCKS-Imm) in chemical reagents. Physical methods involved pretreatment of PCKS-Imm with high hydrostatic pressure (HHP) or freezing-thawing cycles (FTC) followed by immersion decellularization with a protocol involving only chemical reagents (CHEM-Imm). The evaluation of decellularization included assessing the preservation of ECM components and removal of residual DNA, alongside histological assessment. In comparison to decellularization by CHEM-Imm alone, FTC-Imm (FTC + CHEM-Imm) was the most effective in reducing DNA while preserving glycosaminoglycan content (GAG) in the ECM. Conversely, despite pretreatment with pressure (200 MPa), HHP200-Imm (HHP200 + CHEM-Imm) was the least effective in DNA removal. To assess variations in the ability of decellularized rat PCKS-Imm to support recellularization, the scaffolds were seeded with human immortalized renal proximal tubular epithelial cells (RPTEC/TERT1). All recellularized scaffolds, regardless of the decellularization method, demonstrated cell growth over time (7 days). Notably, FTC-Imm scaffolds exhibited the highest expression of the tight junction protein zonula occludens 1 (ZO-1), suggesting a better cell interaction with the scaffold.

Insights gained from the immersion decellularization of PCKS-Imm were extended to perfusion decellularization of whole rat kidneys. Decellularization involved the use of either chemical reagents (CHEM-Prf) alone or a pretreatment with FTC or HHP (200 MPa), followed by decellularization with CHEM-Prf. FTC-Prf demonstrated the highest reduction in DNA but also a significant reduction in GAGs content. On the other hand, HHP200-Prf was the least effective in DNA removal. For further comparison, PCKS prepared from whole decellularized kidneys by perfusion (PCKS-Prf) were recellularized with RPTEC/TERT1 cells. The viability of seeded cells in CHEM-Prf and FTC-Prf scaffolds followed a similar growth pattern compared to their immersion counterparts (CHEM-Imm and FTC-Imm). Interestingly, similar to the immersion approach, FTC-Prf showed superior results regarding

ZO-1 expression. Furthermore, artificial neural networks (ANN) were utilized to investigate the specificity of recellularization, providing a novel method for a location-specific assessment of the seeded cells on the scaffolds. It was demonstrated that, regardless of the decellularization method used, at least 96% of RPTEC/TERT1 cells avoided unspecific attachment to the Bowman capsules. This observation provides crucial clues, indicating that the decellularized ECM possesses instructive memory, which influences the migration of immortalized cells (RPTEC/TERT1) to their specific locations.

All results were integrated into a scoring system, which revealed that FTC-Imm and FTC-Prf received the highest scores. Thus, highlighting the potential of using FTC for whole kidney tissue engineering. In summary, this research underscores the significance of using PCKS as a model for the initial investigation of de- and recellularization methods, thereby reducing the number of sacrificed animals. Moreover, this model can potentially serve as a tool for drug testing and nephrotoxicity assessments. The findings presented in this thesis contribute significantly to the ongoing progression toward the development of a fully engineered kidney.

## Zusammenfassung

Der weltweite Anstieg von chronischen Nierenerkrankungen unterstreicht die dringende Notwendigkeit innovativer Behandlungen für terminale Niereninsuffizienz (ESRD), die über Transplantation und Dialyse hinausgehen. Die Verwendung von Tissue Engineering zur Entwicklung bioartifizieller Nieren könnte einen alternativen Ansatz bieten. Die extrazelluläre Matrix (ECM), die durch Dezellularisierung gewonnen wird, bietet Gerüste mit der natürlichen, komplexen Architektur des Zielorgans. Die De- und Rezellularisierung von ganzen Nieren durch Perfusion sind jedoch hochkomplexe Prozesse, die eine intensive Optimierung verschiedener Parameter erfordern. Nierenpräzisionschnitte (PCKS) wurden als Quelle natürlicher Gerüste verwendet. Da chemische Reagenzien eine schädigende Wirkung auf die ECM haben, zielte diese Studie darauf ab, den Einfluss von physikalischen Behandlungen auf die Wirksamkeit der Immersionsdezellularisierung von PCKS (PCKS-Imm) in chemischen Reagenzien zu untersuchen. Physikalische Methoden umfassten die Vorbehandlung von PCKS-Imm mit hohem hydrostatischem Druck (HHP) oder Gefrier-Auftau-Zyklen (FTC), gefolgt von der Immersionsdezellularisierung mit einem Protokoll, das nur chemische Reagenzien (CHEM-Imm) verwendet. Die Bewertung der Dezellularisierung umfasste die Evaluierung der Erhaltung von ECM-Komponenten und der Entfernung von Rest-DNA sowie eine histologische Auswertung. Im Gegensatz zur ausschließlichen Dezellularisierung mittels CHEM-Imm erwies sich FTC-Imm (FTC + CHEM-Imm) als besonders effektiv sowohl in der Reduzierung von DNA als auch in der gleichzeitigen Erhaltung des Gehalts an Glykosaminoglykanen (GAG) in der ECM. Im Gegensatz dazu war HHP200-Imm (HHP200 + CHEM-Imm), trotz Vorbehandlung mit Druck (200 MPa), am wenigsten effektiv bei der DNA-Entfernung. Zur Beurteilung von Variationen in der Fähigkeit von dezellulierten PCKS-Imm aus Ratten zur Unterstützung der Rezellularisierung wurden die Gerüste mit humanen immortalisierten renalen proximalen tubulären Epithelzellen (RPTEC/TERT1) rezellularisiert. Alle rezellulierten Gerüste, unabhängig von der Dezellularisierungsmethode, zeigten über die Inkubationszeit (7 Tage) Zellwachstum. Bemerkenswert war, dass FTC-Imm-Gerüste die höchste Expression des Tight Junction-Proteins Zonula Occludens 1 (ZO-1) aufwiesen, was auf eine bessere Zellinteraktion mit dem Gerüst hindeutet.

Die Erkenntnisse aus der Immersionsdezellularisierung von PCKS-Imm wurden auf die Perfusionsdezellularisierung von ganzen Rattennieren erweitert. Die Dezellularisierung erfolgte entweder nur mit chemischen Reagenzien (CHEM-Prf) oder mit einer Vorbehandlung mit FTC oder HHP (200 MPa), gefolgt von der Dezellularisierung mit CHEM-Prf. FTC-Prf zeigte die höchste Reduktion von

DNA, aber auch eine signifikante Reduktion des GAG-Gehalts. Andererseits war HHP200-Prf am wenigsten effektiv bei der DNA-Entfernung. Für einen weiteren Vergleich wurden PCKS, die aus ganzen dezellularisierten Nieren durch Perfusion hergestellt wurden (PCKS-Prf), mit RPTEC/TERT1 Zellen rezellularisiert. Die Viabilität der besiedelten Zellen in CHEM-Prf und FTC-Prf Gerüsten folgte einem ähnlichen Wachstumsmuster im Vergleich zu den Immersionsgerüsten (CHEM-Imm und FTC-Imm). Interessanterweise zeigte FTC-Prf, ähnlich wie der Immersionsansatz, überlegene Ergebnisse hinsichtlich der Expression von ZO-1. Darüber hinaus wurden künstliche neuronale Netzwerke (ANN) verwendet, um die Spezifität der Rezellularisierung zu untersuchen, und bieten eine neuartige Methode für eine ortsspezifische Bewertung der besiedelten Zellen auf den Gerüsten. Es wurde gezeigt, dass unabhängig von der verwendeten Dezellularisierungsmethode mindestens 96% von RPTEC/TERT1 Zellen eine unspezifische Anheftung an die Bowman-Kapseln vermieden. Diese Beobachtung liefert wichtige Hinweise darauf, dass die dezellularisierte ECM ein instruktives Gedächtnis besitzt, die die Wanderung immortalisierter Zellen (RPTEC/TERT1) an ihre spezifischen Standorte beeinflusst.

Alle Ergebnisse wurden in ein Scoring-System integriert, das zeigte, dass FTC-Imm und FTC-Prf die höchsten Scores erhielten. Dies unterstreicht das Potenzial von FTC für die Tissue Engineering von ganzen Nieren. Zusammenfassend betont diese Forschung die Bedeutung der Verwendung von PCKS als Modell für die anfängliche Untersuchung von De- und Rezellularisierungsmethoden, um die Anzahl geopferter Tiere zu reduzieren. Darüber hinaus könnte dieses Modell potenziell als Werkzeug für die Untersuchung von Medikamenten und Nephrotoxizitätsbewertungen dienen. Die in dieser Dissertation präsentierten Erkenntnisse tragen erheblich zum laufenden Fortschritt bei der Entwicklung einer vollständig bioartifiziellen Niere bei.

# Contents

<b>1</b>	<b>Introduction</b>	<b>1</b>
1.1	The need for kidney models.....	1
1.2	The kidney.....	3
1.2.1	Structure and function.....	3
1.2.2	Extracellular matrix of the kidney.....	4
1.3	Kidney tissue engineering.....	7
1.3.1	Decellularization.....	7
1.3.2	Recellularization.....	10
<b>2</b>	<b>Aims of this work</b>	<b>12</b>
<b>3</b>	<b>Materials and Methods</b>	<b>13</b>
3.1	Investigation of the effect of physical treatment on PCKS.....	13
3.1.1	Optical characteristics of PCKS after HHP treatment.....	13
3.1.2	Histological assessment of PCKS after physical treatment.....	13
3.1.3	Assessment of the effect of physical treatment on collagen.....	14
3.2	Immersion decellularization.....	14
3.2.1	Kidney retrieval and preparation of PCKS.....	14
3.2.2	Decellularization protocols.....	15
3.3	Perfusion decellularization.....	16
3.3.1	Kidney retrieval.....	16
3.3.2	Decellularization protocols.....	16
3.3.3	Preparation of PCKS from whole decellularized kidneys.....	17
3.4	Optimization of perfusion decellularization after HHP treatment.....	18
3.4.1	Kidney retrieval.....	18
3.4.2	Decellularization protocols.....	18
3.5	Assessment of decellularization effectivity.....	18
3.5.1	Quantification of DNA, GAG and collagen.....	18
3.5.2	Evaluation of ECM structure.....	19
3.5.3	Perfusate analysis.....	20
3.6	Recellularization of PCKS.....	20

3.6.1	Cell Culture .....	20
3.6.2	Cell seeding .....	21
3.7	Characterization of recellularized PCKS .....	22
3.7.1	Analysis of the cell culture medium .....	22
3.7.2	Analysis of the recellularized scaffolds .....	23
3.8	Scoring system .....	26
3.9	Reactivity of PBMCs to native and decellularized kidneys .....	27
3.10	Statistical analysis .....	27
<b>4</b>	<b>Results</b>	<b>28</b>
4.1	Optical characteristics of PCKS after HHP treatment .....	28
4.2	Histological assessment of PCKS after physical treatment .....	29
4.3	Assessment of the effect of physical treatment on collagen .....	30
4.4	Immersion decellularization .....	32
4.4.1	Quantification of DNA, GAG and collagen .....	32
4.4.2	Histological evaluation of decellularized PCKS-Imm .....	34
4.4.3	Evaluation of the ultrastructure in decellularized PCKS-Imm .....	35
4.4.4	Immersion decellularization score .....	37
4.5	Perfusion decellularization .....	37
4.5.1	Quantification of DNA, GAG and collagen .....	37
4.5.2	Perfusate analysis .....	39
4.5.3	Histological evaluation of decellularized PCKS-Prf .....	41
4.5.4	Evaluation of the ultrastructure of PCKS-Prf .....	42
4.5.5	Perfusion decellularization score .....	43
4.6	Characterization of recellularized PCKS-Imm .....	44
4.6.1	Macroscopic assessment of recellularized PCKS-Imm .....	44
4.6.2	Analysis of the cell culture medium .....	45
4.6.3	Analysis of the scaffolds .....	49
4.6.4	Morphological evaluation of the seeded cells with SEM .....	53
4.7	Characterization of recellularized PCKS-Prf .....	55
4.7.1	Analysis of the cell culture medium .....	55
4.7.2	Analysis of the scaffolds .....	58
4.7.3	Morphological evaluation of the seeded cells with SEM .....	62
4.8	Recellularization score .....	63

4.9	Total score performance .....	63
4.10	Optimization of perfusion decellularization after HHP treatment.....	64
4.11	Reactivity of PBMCs to native and decellularized kidneys .....	67
<b>5</b>	<b>Discussion</b>	<b>68</b>
5.1	Unveiling the effects of HHP and FTC on kidney tissues .....	68
5.2	Immersion decellularization.....	69
5.2.1	FTC-Imm: optimal DNA reduction and GAGs preservation.....	69
5.2.2	Insights into DNA reduction and ECM Quality .....	71
5.3	Perfusion decellularization .....	72
5.3.1	Comparing HHP-Prf and FTC-Prf.....	72
5.3.2	FTC-Prf: highest DNA reduction but lowest GAG preservation.	73
5.3.3	Perfusate analysis: SDS reduced GAGs content significantly ..	74
5.3.4	Understanding perfusate volume dynamics.....	75
5.3.5	Perfusion decellularization: insights into protocol optimization .	76
5.4	Recellularization of PCKS .....	76
5.4.1	Shrinkage of recellularized PCKS .....	77
5.4.2	Cell culture medium analysis: metabolic insights.....	78
5.4.3	Analysis of ZO-1 reveals predominance of FTC scaffolds .....	80
5.4.4	Factors affecting cell viability in recellularized PCKS-Prf.....	81
5.4.5	HHP200-Prf scaffolds: residual DNA and seeded cells viability	82
5.4.6	All recellularized PCKS supported cell migration .....	83
5.4.7	Seeded cells growth: renal vs. intestinal epithelial cells.....	83
5.4.8	Artificial intelligence revealed specific recellularization.....	84
5.4.9	Seeded cells exhibited the ability for directed migration .....	85
5.4.10	SEM reveals microvilli in recellularized PCKS .....	86
5.5	Optimization of perfusion decellularization after HHP treatment.....	86
5.6	Reactivity of PBMCs to native and decellularized kidneys .....	87
<b>6</b>	<b>Conclusions and future aspects</b>	<b>89</b>
<b>7</b>	<b>References</b>	<b>91</b>
<b>8</b>	<b>List of abbreviations</b>	<b>111</b>

<b>9 List of figures</b>	<b>112</b>
<b>10 List of supplementary figures</b>	<b>113</b>
<b>11 List of supplementary tables</b>	<b>113</b>
<b>12 Appendix</b>	<b>114</b>
12.1 Materials .....	114
12.2 Number of replicates.....	118
12.3 Histology protocols .....	119
12.4 Scoring system: calculation of the translated scores.....	120
12.5 Scoring system: subcategories results.....	122
12.6 Kidney harvest and perfusion reactor: representative images .....	124
12.6.1 Kidney harvest .....	124
12.6.2 Perfusion reactor.....	124
12.7 Further morphological evaluation of the seeded cells with SEM.....	126
12.8 Resazurin standard curve .....	128
12.9 Further fluorescence analysis of recellularized scaffolds.....	128
12.10 Isolation of peripheral blood mononuclear cells (PBMCs) .....	130
<b>13 Acknowledgments</b>	<b>132</b>
<b>14 Declaration</b>	<b>134</b>

# 1 Introduction

## 1.1 The need for kidney models

The global prevalence of chronic kidney disease (CKD) is progressing rapidly and affects 13% of the world population attributed in part to the rise in risk factors, such as obesity and diabetes mellitus [1]. The 2013 Global Burden of Disease (GBD) report revealed an increase of 41.5% in the global mortality rate linked to CKD between 1990 and 2017 [2]. Successive GBD reports highlighted the escalating prominence of CKD as a cause of death, with rankings of 19<sup>th</sup> in 2013, 13<sup>th</sup> in 2016, and 12<sup>th</sup> in 2017 [1]. CKD is expected to become the fifth leading cause of death by 2040 [3], marking a substantial change from its 36<sup>th</sup> place in 1990 [1]. Current treatment options for end-stage renal disease (ESRD) include dialysis, which have significant shortcomings, for either medical or patient well-being reasons [4,5]. However, dialysis does not replace all kidney functions such as hormone release, homeostasis and immune regulation and modulation [6,7]. Hence, transplantation represents the preferred method of restoring organ function in ESRD patients [8,9]. However, the shortage of donor organs fails to meet the increasing demand and individuals in need of kidney transplantation represent more than 80% of all patients on the waiting list [10]. For instance, 1,966 kidneys were transplanted in Germany in 2022, whereas 6,683 patients remained on the waiting list [11]. Moreover, recipients must remain on immunosuppressants and up to 10% will experience some form of rejection within the first postoperative year [12].

The use of tissue engineering (TE) to develop whole bioengineered kidneys may offer an alternative path to treat ESRD patients [13]. Scaffolds produced by decellularization preserve vital intrinsic properties of the kidney. The ECM includes the natural complex architecture as well as structural and functional proteins needed to promote recellularization and differentiation [14,15]. In parallel, the field of TE explores bottom-up approaches, such as utilizing organoids for kidney construction. This involves building kidneys by assembling smaller functional units, providing an alternative perspective to the top-down approach of decellularization [16]. Simultaneously, xenotransplantation of genetically modified pig kidneys into human recipients may offer a potential solution to ESRD and kidney organ scarcity, although it is still under investigation [17].

Whole kidney de- and recellularization is a complex approach that requires optimization of several parameters [18,19]. It faces several challenges such as developing the decellularization method, identification of an appropriate cell source and the optimization of in vitro culture requirements including medium and GF combinations [9,10]. However, the primary challenge in whole kidney TE is ensuring cell coverage of the whole vascular network and tubular system during recellularization to prevent thrombosis and ensure proper functionality [9]. Therefore, pursuing development and optimization of de- and recellularization strategies on whole kidneys requires sacrificing a huge number of animals. Rat precision-cut kidney slices (PCKS) provide a promising source of natural scaffolds, serving as a model for TE purposes, which facilitates the development of de- and recellularization methods while minimizing the use of animals.

Additionally, PCKS can serve as a model for drug nephrotoxicity testing when de- and recellularized with human kidney cells. Drug-induced acute kidney injury (AKI) is a significant cause of drug failures in clinical trials [20]. It is estimated that 25% of clinically observed acute kidney failures are drug-induced [21]. Although in preclinical drug research, only 2% of tested compounds drop out due to renal toxicity, it is responsible for almost 20% of failures in phase III clinical trials [22–24]. Proximal tubule epithelial cells make up around 65% of all cells in the kidney [25]. In addition, although renal damage can manifest in various regions such as the vascular network, glomerulus, and collecting ducts, the proximal convoluted tubule (PCT) is highly susceptible to injury and linked to a diverse spectrum of kidney diseases [26,27]. Furthermore, drugs and their metabolites tend to accumulate in the PCT [27], making it a primary site of nephrotoxicity [28]. While many AKI cases are reversible, some drugs can induce CKD leading to tubular necrosis, tubulointerstitial inflammation and fibrosis [29].

Current preclinical drug testing mainly relies on two-dimensional (2D) cell cultures and animal models. However, 2D models are incapable of reliably predicting the effects of drugs in clinical studies [27,30]. At the same time, currently available three-dimensional (3D) kidney models (e.g., organ-on-chips, bio-printed tubules and organoids) provide an improved 3D structure but do not closely mimic the complexity of the native tissue [27]. These models typically consist of only one of the kidney's major functional units, either the glomerular filtration barrier (GFB) or the PCT. They often contain one or two cell types and lack the inherent microarchitecture crucial for organ functionality [27,30–34]. Moreover, although kidney organoids show promise as model systems, they are not optimal due to their immature phenotype and lack of the intricate 3D structure found in the ECM [35]. Conversely,

decellularized PCKS already include the locations for all functional units, which can be recellularized with the respective cell types.

In summary, PCKS can serve as a promising model for both TE applications and drug testing. Understanding the intricate structure of the kidney and its diverse functional units is fundamental to developing a 3D kidney model that accurately recapitulates the complexity of the organ.

## 1.2 The kidney

### 1.2.1 Structure and function

The human kidney is a complex organ, which consists of over 30 different cell types [36]. It performs a range of functions, including blood pressure regulation, metabolite excretion, electrolyte control, acid-base balance maintenance, and regulation of essential metabolic and endocrinological processes. Each adult kidney consists of over a million filtration units called nephrons, which perform three main functions: filtration, reabsorption, and secretion. Each nephron consists of a glomerulus, a tuft of high-pressure capillaries encased by the Bowman's capsule (BC), and a renal tubule that drains into the collecting duct (Figure 1) [37].

#### 1.2.1.1 Glomerular filtration

The glomerulus is the filtration site and the GFB comprises three layers. The first layer consists of specialized endothelial cells lining the glomerular capillaries, with highly fenestrated cell bodies that prevent the filtration of blood cells and large proteins while allowing the passage of positively charged substances up to 4-8 nm in size [38]. The second layer is the glomerular basement membrane (GBM), while the third layer is composed of podocytes, featuring finger-like arms known as pedicels that cover the capillaries and create filtration slits. These three components act together in allowing the flow of filtrate through 70 nm pores, ultimately passing to the PCT through the BC, which is lined by parietal cells (squamous epithelial cells) [37,39].

#### 1.2.1.2 Renal tubular system

Approximately 180 liters of filtrate pass through the nephrons daily, with nearly 99% being reabsorbed in the tubular system. It starts with the PCT, where around 67% of water is reabsorbed [37]. The PCT is lined with cuboidal epithelial cells, which have microvilli on their apical luminal surface forming a brush border that increases the surface area for reabsorption [40,41]. On its basal surface,

it faces the tubular basement membrane (TBM). Sodium-potassium pumps on the basolateral side establish an ion gradient essential for the secondary active transport of glucose, amino acids,  $\text{Cl}^-$ , and  $\text{Ca}^{2+}$  through symport mechanisms, while,  $\text{K}^+$ , and  $\text{Mg}^{++}$  ions diffuse transcellularly [37]. The remaining filtrate proceeds to the loop of Henle, composed of descending and ascending limbs. The descending limb is characterized by squamous epithelial cells allowing water to pass through aquaporins but not solutes. In contrast, the ascending limb consists of cuboidal epithelium and lacks aquaporins. It actively reabsorbs ions while remaining impermeable to water [37,39,42]. Subsequently, the filtrate enters the distal convoluted tubule (DCT), where urine composition is adjusted [39,43]. Finally, around six distal tubules drain into a collecting duct, which consists of two main types of epithelial cells: principal cells, responsible for  $\text{Na}^+$  and water reabsorption via aquaporin-2 insertion, and intercalated cells, which help maintain acid-base balance. Ultimately, the final urine moves through into the renal pelvis, passing through the ureter into the bladder [37,39].

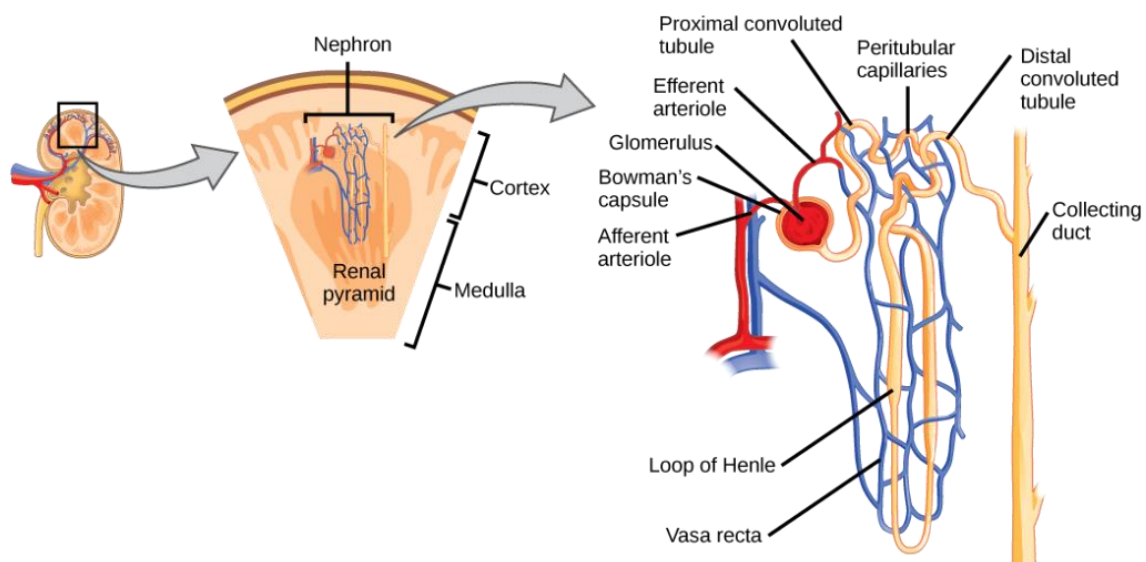


**Figure 1: Human kidney is divided into two main regions, the cortex, and the medulla.** A closer view of a nephron reveals the glomerulus, convoluted tubules and collecting ducts. Adapted from [37]

### 1.2.2 Extracellular matrix of the kidney

The extracellular matrix (ECM) is the non-cellular component found in all tissues, serving as a structural support to surrounding cells. The ECM plays a pivotal role in triggering biochemical and biomechanical signals necessary for tissue development, cell proliferation, differentiation, and homeostasis [44,45]. Notably, each organ has a distinct ECM composition and structure, which evolves through interactions with cells and can provide signaling information to the cells [46].

The vital role of the ECM becomes evident when disruptions occur, leading to various disorders, such as connective tissue disorders, muscular dystrophy, fibrosis, and cancer [46,47]. Genetic disorders related to the kidney's ECM include Alport or Pierson syndromes [48].

The ECM is primarily composed of two main components: the interstitial matrix (IM) and the basement membrane (BM) [46,49]. These structures are built from a combination of proteins such as collagens, proteoglycans (PG), elastin, laminins, fibronectin, and other glycoproteins [50]. PGs consist of a protein core with negatively charged glycosaminoglycans (GAGs). The IM occupies the spaces between cells and is composed of several fibrous proteins with collagen accounting for 30% of all ECM proteins. The gaps within these fibrous networks in the IM are filled with PGs and water [44,46,51]. On the other hand, BMs are specialized, flat, sheet-like ECMs primarily composed of collagen type IV (Col-IV) [46,49]. Additionally, cells secrete various growth factors (GF), cytokines, and chemokines that become deposited within the ECM, which are released in response to cell-mediated forces [52,53]. Moreover, proteins of the kidney ECM are formed by different cells. While mesangial cells produce the mesangial ECM, fibroblasts, myofibroblasts, and pericytes contribute to the IM of the tubulointerstitium. In contrast, BMs are synthesized by the cells that line them. This includes podocytes and endothelial cells for the GBM, parietal epithelial cells for the BC, and tubular epithelial and endothelial cells for the BM of the tubular and peritubular capillaries, respectively [48].

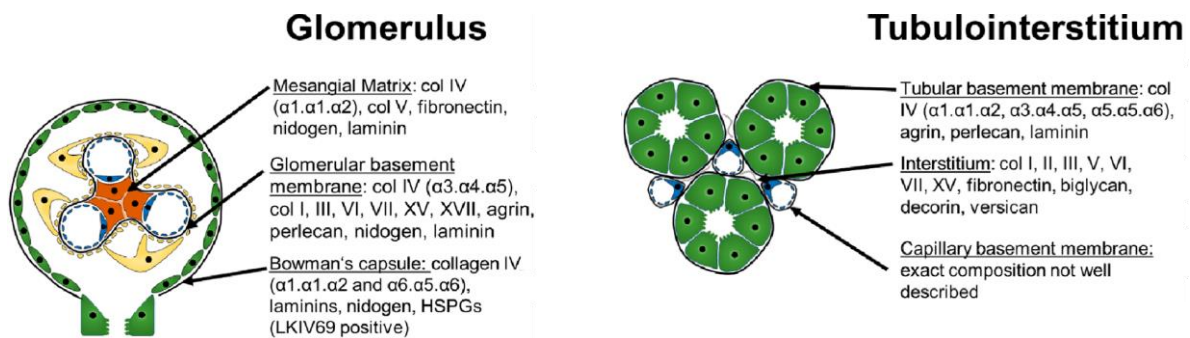


**Figure 2: Representation of the glomerular and tubular ECM components.** Adapted from [48]

In the kidney, different regions in the ECM vary in composition and abundance. For example, the GBM, TBM as well as the BMs of the mesangial matrix, and BC share some common elements like Col-IV and laminin. However, there are components unique to each of these BMs. For instance, the GBM contains nidogen, perlecan, and agrin, while TBM includes only perlecan and agrin.

The BM of the mesangial matrix consists of fibronectin and nidogen, and the BM of the BC comprises only nidogen [48,54]. In contrast, the IM of the kidney (tubule-interstitium), includes collagen types I, II, III, V, VI, VII, XV, fibronectin, biglycan, decorin, and versican (Figure 2) [45,48,54]. These components serve specific functions. For instance, collagens provide primarily structural support, while also imparting elasticity and stability. PGs (e.g., biglycan, decorin, perlecan, agrin, versican) serve both structural and biological roles, as they resist compression, maintain hydration, and trap GFs in the ECM [45,50]. Collagen and glycoproteins like fibronectin and laminin establish connections with the cells via integrins, which are the first point of contact for the cells with the ECM [55].

### **1.2.2.1 Integrins and directional cell migration**

Integrins are part of the focal adhesion complex (FAC) within the cells acting as mechanical sensors upon adhesion and engaging with the ECM. FAC comprises proteins like FAK, paxillin, vinculin and talin, which provide a structural link between integrins and the actin cytoskeleton (Figure 3) [55–57]. This connection results in ECMs coordinating various signaling processes with the cells, working in both inside-out and outside-in manners [50]. The FAC's signaling cascades interact with actomyosin to generate traction forces, facilitating cell migration through cytoskeletal rearrangements [55–57]. This involves the formation of lamellipodia, which generate forces that propel the cell forward. Furthermore, actin de- and polymerization is crucial for the formation and retraction of cellular protrusions during cell movement [58,59].

Directional cell migration refers to the movement of individual cells in a particular direction, usually towards a specific target or along a predetermined path. This type of migration is essential for various biological processes, including embryonic development, tissue repair, and immune response. Cells use various mechanisms to sense the direction of movement, such as chemotaxis, haptotaxis, topotaxis and electrotaxis [60]. Chemotaxis is the process by which cells move towards or away from a chemical gradient, while haptotaxis is the movement of cells in response to gradients of adhesive molecules present in the ECM such as fibronectin, laminin, collagen or specific cytokines [61]. Topotaxis, refers to the migration guided by physical cues, such as stiffness or topographical features of the substrate [62].

In summary, creating a functional in vitro kidney model depends on the accurate reproduction of nephron architecture and the precise arrangement of diverse renal cell types.

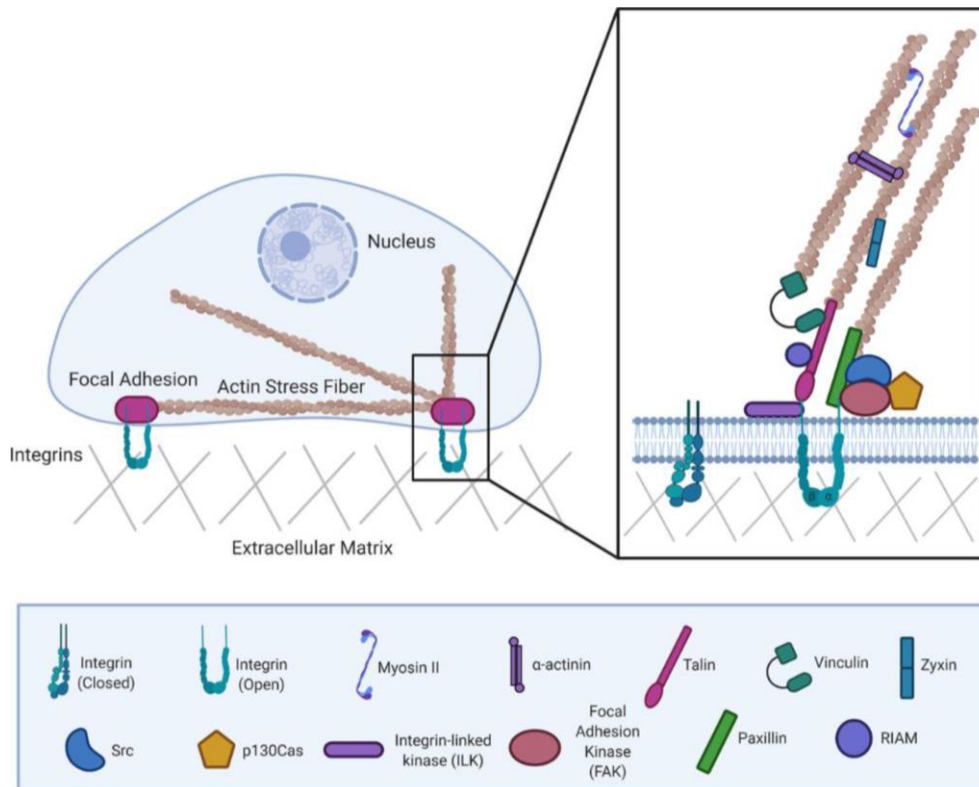


**Figure 3: Illustration of a focal adhesion complex in a cell.** Integrin receptors are attached to the extracellular matrix. The inset shows specific proteins that make up a focal adhesion. Adapted from [63]

### 1.3 Kidney tissue engineering

Tissue engineering (TE) involves the development of functional biological tissues or organs to replace or repair damaged or dysfunctional ones. This requires employing *in vivo* or *ex vivo* approaches using natural or synthetic scaffolds, cells, GF, gene manipulation or a combination of all mentioned elements [64]. The role of scaffolds is to provide mechanical support as well as chemical and physical cues to drive cell proliferation and differentiation. The ECM, which is typically derived by decellularization, is considered an ideal natural scaffold [64,65].

#### 1.3.1 Decellularization

Decellularization is a process used to remove cells, including cellular components, debris and genetic material, from a tissue or organ while preserving the ECM. In this process a combination of physical, chemical, and enzymatic methods are used. However, hitting a balance between removing

cells and preserving the ECM is the utmost challenge of decellularization. There are mainly two approaches of decellularization: either by immersion or by organ perfusion [65,66].

Decellularization by immersion entails submerging the tissue in chemical reagents. The reagents enter the tissue by passive diffusion and the efficiency of the process depends largely on tissue thickness and cell density [66,67]. This process requires long incubation times in chemical reagents and extensive washing steps for an effective decellularization and removal of the chemical reagents. However, this increases the risk of damaging the ECM and losing its components [67]. On the other hand, the invention of perfusion decellularization in 2008 by Ott et al allowed the generation of tissue-engineered scaffolds from entire organs [68]. It involves perfusing the chemical reagents through the vascular network to allow for a better penetration in the entire tissue. While immersion decellularization is sufficient for simple tissues like heart valves and cornea, it is not effective for whole organs [69,70]. Perfusion decellularization allows a more uniform removal of cells throughout larger and more complex tissues, leading to a more consistent composition and mechanical properties of the resulting scaffold [19].

Various chemical reagents have been used for decellularization including ionic detergents, non-ionic detergents and protease enzymes. While non-ionic detergents (e.g. Triton X-100) disrupt DNA-protein and lipid-protein interactions without destroying the native protein structures, ionic detergents (e.g. sodium dodecyl sulfate; SDS, sodium deoxycholate; SDC) dissolve cell and nucleic membranes and completely denature proteins. Proteases such as trypsin cleave peptide bonds to detach cells from the tissue surface, but prolonged exposure to these enzymes causes damage to collagen [65,71,72]. Side effects of decellularization reagents include reducing mechanical properties, damaging ECM structure and lowering the potential to provide structural support for seeded cells.

Physical treatment methods have been described to be potentially less damaging to the ECM [73,74]. Freezing–thawing-cycles (FTC) is frequently applied in decellularization protocols [72,75]. Freezing causes intracellular ice crystal formation, which disrupts cellular membranes leading to cell lysis [72,73,75]. High hydrostatic pressure (HHP) is widely used in the food industry for the inactivation of microorganisms. It pushes water molecules into protein cavities destroying their tertiary and quaternary structures without breaking covalent molecular bonds [76]. Nevertheless, FTC and HHP are typically not sufficient for complete decellularization and are often employed as a pretreatment for cell devitalization.

Subsequently, they are followed by chemical reagents for thorough decellularization [73]. Kishida and his colleagues used HHP (980 MPa) for the devitalization of bones, bone marrow, blood vessels, corneas, heart valves, uterine tissues, menisci and cartilage [77–82]. It was reported that cellular material and DNA were effectively removed from these tissues while maintaining the ECM integrity. Moreover, the application of ultrasound at frequencies above 20 kHz has also been used in TE [73]. Ultrasound waves cause an alternating stress, which creates small cavitation bubbles. After reaching a critical size, the bubbles implode. Thus, creating high shear forces, which facilitate medium penetration into the tissue and assist in cell lysis and removal of cell debris [83].

The development of a transplantable kidney relies on the de- and recellularization of the entire organ by perfusion. Several perfusion decellularization protocols have been tested for rodents, human and porcine kidneys [84–89]. Nevertheless, the immersion approach was used in several studies involving precision-cut kidney slices (PCKS) for testing de- and recellularization methods [10,90–93]. Applying physical treatments on kidney tissues to devitalize the cells prior to decellularization could be a suitable approach to reduce the incubation time in chemical reagents [73,74]. While FTC and ultrasound were used in connection with kidney decellularization [94–98], HHP has not been reported for the same application. Each decellularization method can result in different effects on the ECM integrity [64]. Therefore, evaluating the scaffold after decellularization is crucial to determine the effectiveness of the chosen method.

A primary focus for the evaluation of decellularization effectiveness is to assess the extent to which DNA has been removed from the tissue. Residual cellular material in the scaffold causes cytocompatibility problems *in vitro* upon recellularization and adverse host responses *in vivo* [99–102]. The investigation of host responses upon scaffold implantation showed that adverse responses can be avoided if the amount of residual DNA stays below a specific level [99–102]. Therefore, reaching a maximum amount of DNA of 50 ng/mg of dry tissue is considered an important threshold for the evaluation of decellularization [65]. Moreover, this evaluation includes morphological and histological analysis, along with the assessment of ECM mechanical properties and remaining components (e.g. GAG, GF, collagen) [65].

### 1.3.2 Recellularization

Recellularization is the process of seeding cells into synthetic or natural ECM scaffolds to create functional tissues. The choice of appropriate cell sources such as stem cells or differentiated cells and the optimal seeding density, play a crucial role in ensuring adequate cell distribution and coverage. Furthermore, the choice of medium and GFs impact cell viability, proliferation, and differentiation. The evaluation of recellularization involves histological and immunofluorescence analyses to assess cell distribution and expression of specific proteins. Additionally, measuring lactate dehydrogenase (LDH) release upon cell damage [103,104], or using resazurin, which is converted to the fluorescent dye resorufin by viable cells are both widely used indicators [105]. Moreover, the metabolic activity of seeded cells can be evaluated by measuring lactate release and glucose consumption. An increase in lactate release indicates cellular stress caused by hypoxia, tissue repair, oxidative stress, or mitochondrial disturbances [106]. Moreover, functional assays are vital to monitor the tissue's ability to perform specific functions [107].

PCKS serve as a model for the development of decellularization methods, as well as the optimization of recellularization techniques [91,92,108–110]. However, recellularization of PCKS encounters challenges related to limited cell survival within the core of the scaffolds, particularly when the culture medium is not actively circulated under static culture conditions [64,111]. Thus, hindering effective mass transport, as passive diffusion is limited to short distances (100-200  $\mu\text{m}$ ), resulting in inadequate nutrient and oxygen supply leading to necrosis [64,111]. To enhance mass transport, bioreactors have proven effective for improving cell proliferation and differentiation within recellularized tissues like muscles, tendons, and bones [112–117].

Developing a transplantable kidney necessitates the de- and recellularization of the whole kidney through perfusion. The kidney's distinctive characteristic lies in its accessibility for perfusion recellularization through three distinct points: the renal artery and vein as well as the ureter [9,118]. This has made perfusion-based recellularization of kidneys the most reported method. [9]. In a study by Song et al., decellularized rat kidneys were recellularized by perfusing primary endothelial cells through the artery and primary epithelial cells through the ureter. Subsequently, these recellularized kidneys were capable of producing urine upon transplantation [119]. Nonetheless, stem cells are preferred over primary cells due to their higher proliferation capacity [9]. Various patient-derived cell sources have emerged for kidney recellularization, including renal stem or progenitor cells from adult kidneys, pluripotent stem cells like embryonic stem cells (ESC) and induced pluripotent stem cells

(iPSC) as well as fetal and adult stem cells like amniotic fluid stem cells and mesenchymal stem cells (MSC) [9,118,120]. Given the kidney's composition of around 30 different cell types, location-specific cell differentiation is crucial for a successful recellularization [9,36].

### **1.3.2.1 ECM provides an instructive memory for a location-specific cell differentiation**

The ECM provides signals that guide not only cell attachment and migration but also differentiation [14,15,44]. To explore whether decellularized ECM retains instructive memory capable of influencing phenotype-specific differentiation, decellularized human kidney and heart tissues were recellularized with human embryonic mesodermal precursor cells. In order to assess the inherent potential of the ECM to induce cell differentiation, no additional GFs were added to the cell culture medium. The study demonstrated that cells seeded on kidney scaffolds differentiated only into renal cells, while only cardiac cells were observed on heart scaffolds [121]. Similar observations have been reported in other studies involving decellularized kidney or lung tissues, where ESCs or nephrosphere cells (renal stem-like cells) were seeded [10,90,92]. Additionally, in a separate study, whole decellularized kidneys were recellularized with endothelial cells derived from human iPSCs. Surprisingly, the adherent endothelial cells demonstrated specialization by forming a fenestrated endothelium specifically within the glomerular capillaries, but not in the vascular capillaries [122]. These findings suggest that the ECM possesses intrinsic factors that can guide cell differentiation in a tissue-specific manner.

## 2 Aims of this work

The work of this project is centered around the development of a 3D kidney tissue model using rat kidney tissues. The specific aims can be summarized as follows:

1. Investigation of the impact of physical treatments (FTC and HHP), on the optical and histological characteristics of kidney tissues as well as on collagen denaturation.
2. Immersion decellularization of precision-cut kidney slices (PCKS-Imm) to investigate the overall effectiveness of three physical treatment methods (HHP, UBS, and FTC) in combination with chemical-based immersion decellularization.
3. Perfusion decellularization of whole rat kidneys to investigate the overall effectiveness of two physical treatment methods (HHP and FTC) in combination with chemical-based perfusion decellularization.
4. Recellularization of rat PCKS-Imm and PCKS obtained from whole rat kidneys decellularized by perfusion (PCKS-Prf) with immortalized human renal proximal tubular epithelial cells (RPTEC/TERT1) to determine variations in the ability of decellularized PCKS-Imm and PCKS-Prf to support recellularization.

## **3 Materials and Methods**

All materials used within this project are listed in the appendix (section 12.1).

### **3.1 Investigation of the effect of physical treatment on PCKS**

#### **3.1.1 Optical characteristics of PCKS after HHP treatment**

The effect of HHP on the optical characteristics of kidney tissues was assessed immediately after the treatment. The PCKS were exposed to different pressure levels: 10, 50, 100, 200, 400, and 600 MPa for 10 min at 37 °C (n = 2) each. Subsequently, the PCKS subjected to HHP were decellularized following the CHEM-Imm protocol described in section 3.2.2. Photographs of individual PCKS after HHP treatment and after each decellularization step were captured to examine their optical characteristics. These images were acquired using a Nikon camera within a specially designed setup for consistent lighting conditions.

#### **3.1.2 Histological assessment of PCKS after physical treatment**

The PCKS were evaluated histologically immediately after the physical treatment, and before any additional decellularization with CHEM-Imm protocol described in section 3.2.2. PCKS were subjected to three HHP treatments (either 10, 100 or 600 MPa). Similarly, PCKS were subjected to three different freezing and thawing cycles: either one cycle (1 FTC), three cycles (3 FTC) or six cycles (6 FTC). One cycle includes freezing at -80 °C for 1 h and thawing at 4 °C for 30 min. After these treatments, the PCKS were fixed with 4% paraformaldehyde (PFA) in phosphate-buffered saline (PBS) overnight at room temperature (RT). The fixed samples underwent a series of steps including dehydration and paraffin infiltration using a tissue processor, following the protocol outlined in Table S 12. Afterwards, the samples were embedded in paraffin blocks and sliced into sections measuring 4 µm in thickness. Subsequently, the sections were stained with hematoxylin and eosin (H&E) according to the protocol shown in Table S 13. The changes in the total area of non-cellular spaces (NCS) in H&E stained sections corresponding to interstitial, luminal (e.g. tubules and vessels) and BC spaces was investigated. Five images were taken for each slice at different locations in the kidney cortex using the 20x objective with a light microscope. NCS were measured by ImageJ. Image processing began by grouping all images into a stack and converting them to grayscale (8-bit).

The threshold tool was used to determine the area of the NCS. The area was normalized to NCS in native PCKS.

### **3.1.3 Assessment of the effect of physical treatment on collagen**

The impact of physical treatments (FTC and HHP) on collagen denaturation was investigated using the fluorescently-labeled collagen hybridizing peptide (F-CHP), which binds to denatured collagen. Native rat tendons obtained from rat tails were employed as the negative control, while tendons heated to 60 °C served as the positive control. Tendons were subjected to four FTC (-80 °C for 1 h and 4 °C for 30 min). HHP treatment was also administered, with tendons exposed to 600 MPa pressure for 10 min at 30 °C. For comparison with the physical treatments, tendons were incubated in a 12 well plate with 1% SDS or 1% Triton X-100 (2 ml) for 2 h on a shaker (130 rpm), followed by washing 2x with PBS. Following treatment, the tendons were fixed using 4% PFA overnight. Subsequently, histological processing and preparation of paraffin slices were carried out as described above. The sections were deparaffinized (2x xylol, 5 min) and rehydrated (2x 96% ethanol and 1x 70% ethanol, 1 min each). The F-CHP solution was heated to 80 °C for 5 min and then rapidly cooled to RT by placing it in an ice bath for 30 s. The tissue slices were incubated with the F-CHP solution overnight at 4 °C. Subsequently the slides were washed 3x with PBS for 5 min. A mounting medium without 4',6-diamidino-2-phenylindole (DAPI) was applied, and the slides were covered with coverslips. The stained samples were analyzed using a fluorescence microscope. Fluorescence intensity was measured using QuPath.

## **3.2 Immersion decellularization**

### **3.2.1 Kidney retrieval and preparation of PCKS**

Male Sprague Dawley rats (290-490 g) were chosen to obtain kidneys for the generation of PCKS. Kidneys were harvested after sacrificing the rats under anesthesia with a cervical dislocation. Anesthesia protocol involved a mixture of O<sub>2</sub> and N<sub>2</sub>O at rates of 0.8 and 1.6 l/min, respectively, along with Isoflurane maintained at 2.5%. Transcardial perfusion was performed after euthanasia with heparin in a PBS solution (10 I.E./ml, 150 ml) to remove the blood and prevent organ damage due to coagulation (Figure S 6). After that, the renal arteries were cannulated in situ and the kidneys were perfused upon retrieval with PBS (50 ml, 5 ml/min) for further blood removal. Harvested kidneys

were cut into 1 mm thick slices using a vibratome. Kidney retrieval from rats was performed under the guidelines of the German Animal Protection Law (§4).

#### 3.2.2 Decellularization protocols

Kidney slices that underwent immersion decellularization are denoted as PCKS-Imm. Immersion decellularization of PCKS-Imm followed a slightly modified published protocol, which in this work is simply referred to as “**CHEM-Imm**” [90]. PCKS were incubated for 1 h in 0.025% trypsin-Ethylenediaminetetraacetic acid (EDTA), followed by 2 h of 2% Triton X-100, 2 h of 2% SDC, and 15 h of 0.1% SDS. After each step of incubation, PCKS-Imm were washed 2x for 10 min with PBS. Following SDS, PCKS-Imm were washed using one of two different approaches, depending on the intended application:

1. PCKS-Imm that were not further recellularized and were only used for assessing the decellularization process were washed 3x for 10 min with PBS.
2. PCKS-Imm designated for recellularization were washed 3x for 60 min with PBS supplemented with 1% Antibiotic/Antimycotic solution for further decontamination.

All steps were performed in a 6-well plate at RT and under continuous agitation (150 rpm). To investigate the effect of physical treatment on the decellularization efficacy of PCKS-Imm, the CHEM-Imm protocol was combined with one of the following physical treatments (Figure 4):

**HHP-Imm protocol (HHP + Chem-Imm):** PCKS-Imm were placed in a falcon tube filled with PBS and inserted into the high-pressure chamber of the cold isotactic pressurization machine. PCKS-Imm were exposed to three different HHP treatments (50, 100 and 200 MPa) for 10 min at 30 °C. After HHP treatment, PCKS-Imm were decellularized using the CHEM-Imm protocol.

**FTC-Imm protocol (FTC + Chem-Imm):** PCKS-Imm were frozen at –80 °C for 1 h and thawed at 4 °C for 30 min. After performing four FTCs, PCKS-Imm were decellularized using the CHEM-Imm protocol.

**UBS-Imm protocol:** a custom designed ultrasonic bath system (UBS) was used to support the decellularization process [123]. Two bathes were connected in parallel to the same ultrasonic generator. PCKS-Imm were decellularized according to the CHEM-Imm protocol, whereas the incubation in Triton X-100 and SDC was carried out in the UBS. Each PCKS-Imm was placed in a sample

### 3 Materials and Methods

holder, which in return was placed in the UBS. Thus, allowing the treatment of three PCKS-Imm per bath. To avoid overheating of the samples, the UBS was connected to a cooling unit. Additionally, the chemical reagents were pumped in a cycle passing over an ice bath. PCKS-Imm were treated at a frequency of 28 kHz and at two different powers (30 or 60 W).

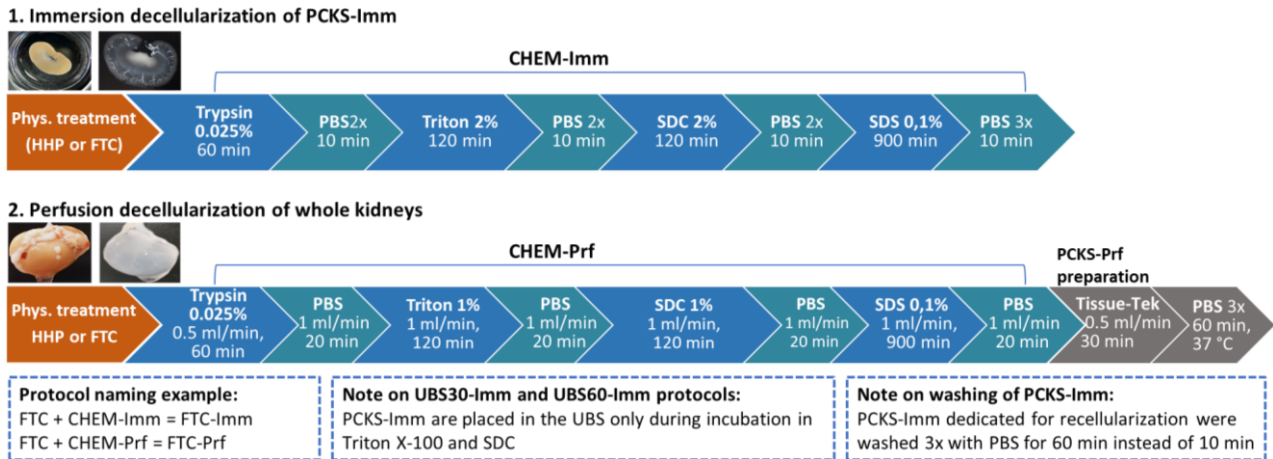


**Figure 4: Schematic representation of the decellularization protocols** for both the immersion and perfusion approaches, along with the corresponding physical pretreatments

## 3.3 Perfusion decellularization

### 3.3.1 Kidney retrieval

Male Sprague Dawley rats (275-450g) were selected for the decellularization of whole kidneys by perfusion. The rats were anesthetized using isoflurane and received intravenous heparinization via the tail at a dosage of 2000 IU/Kg. After 30 mins of circulation, the rats were sacrificed under anesthesia with a cervical dislocation, and the same procedures as described in the immersion approach were performed. The kidneys were then cannulated and decellularized by perfusion. Animal experiments and kidney retrieval were approved by the local animal care and use committee (7221.3-1-036/19).

### 3.3.2 Decellularization protocols

Whole rat kidneys were decellularized by perfusion in a perfusion bioreactor (Figure S 7) using the **CHEM-Prf** protocol, which shares similarities with CHEM-Imm with minor modifications. The cannulated kidneys were connected to a peristaltic pump and perfused with the decellularization solutions

through the renal artery. The same durations were used as in CHEM-Imm but with lower concentrations for some of the reagents. The kidneys were perfused for 60 min with 0.025% trypsin-EDTA at 0.5 ml/min, followed by 2 h of 1% Triton X-100, 2 h of 1% SDC, and 15 h of 0.1% SDS at 1 ml/min. After each perfusion step with a chemical reagent, the kidneys were perfused for 10 min with PBS. The decellularization process was completed by perfusing the kidneys for 30 min with PBS.

To explore how physical treatments, affect the decellularization effectiveness of whole rat kidneys, the CHEM-Prf protocol was combined with either FTC or HHP (200 MPa) (Figure 4):

**HHP-Prf protocol (HHP + CHEM-Prf):** cannulated whole kidneys were placed into falcon tubes with PBS and treated with HHP as described above. The kidneys were then decellularized with CHEM-Prf.

**FTC-Prf protocol (FTC + CHEM-Prf):** cannulated whole kidneys were frozen four times at -80 °C for 18 h, then thawed three times at 4 °C for 6 h, and finally thawed overnight before starting the decellularization protocol. The kidneys were then decellularized with CHEM-Prf.

#### 3.3.3 Preparation of PCKS from whole decellularized kidneys

After finishing the CHEM-Prf protocol, the kidneys were perfused with prewarmed Tissue-Tek at a flow rate of 0.5 ml/min and 37 °C for 30 min. The kidneys were then immediately placed in a falcon tube with ice cold PBS and placed on ice. They were then cut into 500 µm thick slices using the vibratome. All obtained PCKS-Prf, were washed 3x for 60 min with prewarmed PBS and supplemented with 1% Antibiotic/Antimycotic and at 37 °C. PCKS-Prf were used for two different purposes: 4 PCKS-Prf were further recellularized and the rest were used for the assessment of decellularization.

## 3.4 Optimization of perfusion decellularization after HHP treatment

### 3.4.1 Kidney retrieval

Male Sprague Dawley rats (270-450g) were used for perfusion decellularization of whole kidneys. Animal preparation and kidney harvest were conducted as described in section 3.3.1.

### 3.4.2 Decellularization protocols

A straightforward perfusion protocol was adopted, utilizing only SDS as the chemical decellularization agent. This optimization procedure comprised two approaches:

**Direct decellularization:** the kidneys were perfused with 144 ml of 1% SDS for 6 h, followed by PBS perfusion (350 ml) for 14.5 h, both at a flow rate of 0.4 ml/min. This protocol is simply referred to as SDS1%. For the physical pretreatments, the kidneys were treated with HHP (100 MPa) or FTC, as outlined in section 3.3.2, followed by decellularization with SDS1% protocol.

**Indirect decellularization:** the kidneys were initially preconditioned by perfusion with 432 ml of PBS for 18 h, followed by 144 ml of 0.5% SDS for 6 h. Subsequently, the kidneys were extensively washed by perfusion with 350 ml of PBS for 14.5 h, all at a flow rate of 0.4 ml/min. For the physical pretreatments, the kidneys were treated with HHP (150 MPa) or FTC, as outlined in section 3.3.2, followed by decellularization using the SDS0.5% protocol.

The decellularized kidneys from both approaches were immersed in liquid nitrogen (20 s) for partial solidification, making it possible to cut their soft structure in half using a scalpel.

## 3.5 Assessment of decellularization effectivity

### 3.5.1 Quantification of DNA, GAG and collagen

All decellularized kidney tissues, including PCKS (PCKS-Imm and PCKS-Prf) or kidney halves, underwent the same homogenization process. Since a single decellularized PCKS has a low weight, quantifying all parameters using just one slice is challenging. To address this limitation, decellularized PCKS-Imm or PCKS-Prf were combined and homogenized together (9000 rpm, 25 s, 3x). The homogenates were then centrifuged at 2000 g to remove excess fluid. Subsequently, the samples were freeze-dried for 8 h. A 1 mg dry homogenate was used in the following assays, and the results were normalized to the total dry tissue weight.

**DNA:** dry homogenates were digested using proteinase K (18 h, 38 °C) followed by adding 200 µl of absolute ethanol. After several washing steps with buffer reagents, DNA was extracted using a mini spin column provided in the DNeasy Blood and Tissue Kit and according to manufacturer's instructions. DNA was quantified using NanoDrop Lite spectrophotometer.

**Collagen and GAGs** were quantified using Sircol and Blyscan assays, respectively according to the manufacturer's instructions. For collagen extraction, the dry homogenates were incubated overnight in a pepsin digestion solution (0.1 mg/ml in 0.5 M acetic acid) at 4 °C. Sircol Dye Reagent (500 µl) was added to the digested samples to form a collagen-dye complex. It was then solubilized with the Alkali Reagent (250 µl) and the absorbance of the samples was measured at 562 nm. For GAGs measurement, each sample was digested at 65 °C for 3 h in a papain extraction solution. Blyscan Dye Reagent (750 µl) was then added to precipitate the GAG-dye complex. After adding the dissociation reagent (500 µl) to dissolve the dye complex, the absorbance was measured at 650 nm using a microplate reader.

#### 3.5.2 Evaluation of ECM structure

##### 3.5.2.1 Scaffolds Histology

Decellularized PCKS or kidney halves were fixed with 4% PFA overnight at RT. Histological processing was carried out according to a protocol specifically optimized for decellularized samples (Table S 14) Paraffin slices (4 µm thick) were stained with H&E as described in section 3.1.2. All images were presented using a 20x objective and a scale bar of 100 µm.

##### 3.5.2.2 Scanning electron microscopy (SEM)

Scanning electron microscopy (SEM) was used for the investigation of the ultrastructure of decellularized scaffolds as well as the morphology of seeded cells in recellularized scaffolds. Samples were fixed with a solution of 2% glutaraldehyde and 1% PFA in sodium phosphate buffer and were stored at 4 °C until further processing. The samples were then washed in 0.1 M sodium phosphate buffer (pH 7.3) and treated with 1% osmium tetroxide for 2 h. Afterwards, the samples were dehydrated in an ascending series of acetone and critical point dried. Samples were mounted on aluminum SEM-carriers with adhesive conductive carbon tape and were sputter-coated for conductivity with a thin gold layer (approximately 10-15 nm) under vacuum. The samples were analyzed with a field emission scanning electron microscope.

### 3.5.3 Perfusate analysis

Perfusate actual volume was determined by measuring its weight after each perfusion step. Perfusate samples were also collected after each step and stored at -20 °C for later analysis:

**DNA assay:** a volume of 20 µl of the liquid perfusate was used as an input for the DNA assay, without the need for prior digestion with proteinase K. DNA was extracted as described earlier.

**Collagen and GAG:** a 100 µl volume of liquid perfusate was utilized as the input for the collagen and GAG assays. However, for GAG extraction, perfusates obtained from the SDS step were diluted at a ratio of 1:2.5. The quantification of collagen and GAG was performed following the protocols described above with minor modifications. The volumes of Sircol Dye Reagent and Blyscan Dye Reagent used were adjusted to 500 µl and 750 µl, respectively.

To account for the variation in perfusion duration between different steps, obtained data were normalized to both the actual volume of the perfusate and to a duration of 60 min.

## 3.6 Recellularization of PCKS

Different scaffolds from the immersion approach (CHEM-Imm, HHP200-Imm, UBS60-Imm and FTC-Imm) and the perfusion approach (CHEM-Prf and FTC-Prf) were selected for recellularization with immortalized human RPTEC/TERT1 cells. To compare with decellularized PCKS, synthetic scaffolds made from transparent and inert glass microfibers were used. These scaffolds are in this work simply referred to as SYNTH.

### 3.6.1 Cell Culture

The RPTEC/TERT1 cells were cultured at 37 °C in Dulbecco's modified Eagle medium DMEM-HAM's F12 supplemented with 1% fetal bovine serum (FBS), 1% GlutaMax (Gibco), insulin, transferrin, selenium (ITS; I = 10 µg/ml; T = 5.5 µg/ml; S = 0.67 ng/ml), 36 ng/ml hydrocortisone, 10 ng/ml epidermal growth factor and 1% Penicillin/Streptomycin. RPTEC/TERT1 cells were cultured to a maximum of 30 passages. Cells were split every 2-3 days at 70-80% confluence using 0.05% Trypsin EDTA in DPBS. Subsequently, the cells were seeded at a concentration of  $8 \times 10^4$  cells/ml and incubated at 37 °C under conditions of 5% CO<sub>2</sub> and 95% humidity in the incubator. Cells were counted using a Trypan blue solution and a counting chamber.

### 3.6.2 Cell seeding

As described above, decellularized scaffolds (PCKS-Imm and PCKS-Prf) dedicated for recellularization were washed extensively by the end of the decellularization for the removal of residual chemical reagents and decontamination (3x for 60 min). Moreover, PCKS-Imm and PCKS-Prf as well as SYNTH scaffolds were preconditioned by incubation in RPTEC/TERT1 medium for 24 h, which allowed for additional washing and provided essential nutrients necessary for cell growth in the scaffolds. The scaffolds were then stored at 4 °C for up to 2-3 days until recellularization.

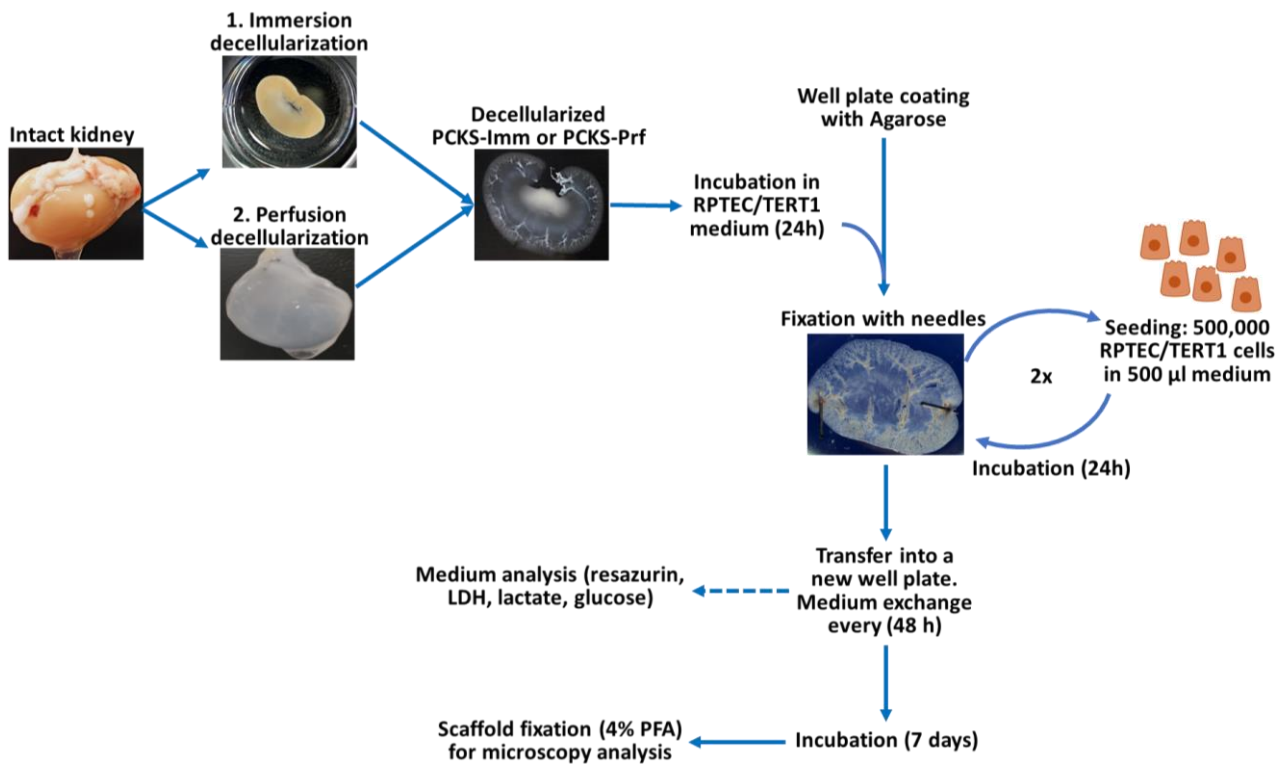


Figure 5: Schematic overview of the recellularization protocol for PCKS-Imm and PCKS-Prf

A 12 well plate was coated with agarose gel (2% in distilled water; 1.5 ml/well) and sterilized with UV light for 30 min. The decellularized PCKS and SYNTH scaffolds were then fixed in each well on the agarose layer with fine needles. The scaffolds were seeded in two steps with a total cell density of  $1 \times 10^6$  cells. In the first step 500,000 cells were suspended in 500  $\mu$ l RPTEC/TERT1 medium and gently pipetted on the middle of the scaffold. The scaffolds were incubated at 37 °C for 24 h to allow for cell attachment and initial cell migration. After that, the cell suspension was removed and the second seeding step was started. To ensure a better spread of the cells, the scaffolds were flipped over and fixed again with needles. After that, the scaffolds were seeded again under the same conditions. By the end of the incubation time of the second seeding step, the scaffolds were transferred into a new well plate and incubated for seven days with 1.5 ml RPTEC/TERT1 medium, which was changed on day 3, 5 and 7. An image was taken for each scaffold before cell seeding and by the end of the 7<sup>th</sup> day of the recellularization process with a stereomicroscope. The area of the scaffolds was measured using ImageJ as described in section 3.1.2.

To serve as a 2D monolayer control, 60,000 RPTEC/TERT1 cells in 500  $\mu$ l medium were seeded in a single step during the second seeding day of the scaffolds. Subsequently, these cells were incubated for 24 h and subjected to the same treatment as the scaffolds.

## 3.7 Characterization of recellularized PCKS

### 3.7.1 Analysis of the cell culture medium

The following assays were conducted at the time of exchanging the cell culture medium on days 3, 5, and 7 during the incubation period of the scaffolds.

#### 3.7.1.1 Resazurin reduction assay

Cellular viability in all recellularized scaffolds (PCKS and SYNTH) were assessed by quantifying the reduction of resazurin into resorufin. Sterile filtered resazurin solution was added to each well at a ratio of 1:10, resulting in a final concentration of 100  $\mu$ M, using a volume of 150  $\mu$ l per well. The plate was then incubated at 37 °C for 2 h. A 200  $\mu$ l of the cell culture medium was then transferred into a black 96 clear bottom microplate and the fluorescence of resorufin was measured at 545 nm excitation and 600 nm emission with a microplate reader. The recellularized scaffolds were subsequently washed 3x for 10 min at 37 °C with PBS and on an orbital shaker (150 rpm). Fluorescence data were normalized to the area of the scaffold before recellularization.

#### **Standard curve for converting resazurin fluorescence values into a cell number**

RPTEC/TERT1 cells were suspended and seeded into a 6 well plate at various cell densities: 31,250; 62,500; 125,000; 250,000 and 500,000 cells per well in 1 ml of RPTEC/TERT1 medium. The well plate was then incubated at 37 °C for 24 h. On the second day, 100 µl of resazurin (100 µM) was added to each well and the assay was conducted as described above. The wells were then washed with PBS and 1 ml of trypsin was added to each well, followed by incubation at 37 °C for 5 min. Upon centrifugation, the cell pellet was resuspended with RPTEC/TERT1 medium and the actual cell count was determined as described above. A standard curve was created by plotting the number of counted cells against their corresponding resazurin fluorescence values. A logarithmic regression line was used to calculate the number of cells for the fluorescence values determined from the recellularized scaffolds (Figure S 12).

#### **3.7.1.2 Measurement of glucose, lactate and LDH in the culture medium**

Glucose, lactate, and LDH concentrations were measured photometrically using the Cobas® Mira Plus. After the resazurin assay, 500 µl was collected from the remaining cell culture medium. The Glucose GOD-PAP and Lactate LOX-PAP kits were used to measure glucose and lactate concentrations, respectively. The substrates contained in the sample are converted by oxidase, releasing hydrogen peroxide, which reacts with 4-aminoantipyrine and phenol to form the dye quinonimine. The intensity of the dye is proportional to the concentration and is photometrically measured at a wavelength of 546 nm. Glucose consumption was calculated by subtracting the remaining glucose content in medium from the content of fresh medium. Data of lactate and glucose were normalized to the number of viable cells on the respective incubation day, which was determined using the resazurin standard curve described above. Moreover, LDH FS-IFCC kit was used to quantify LDH concentration in the cell culture medium. Four parts of reagent R1 and one part of reagent R2 were first mixed. The lactate contained in the mixture is converted to pyruvate by LDH. The changing extinction is measured at a wavelength of 340 nm. The Assays were carried out according to the manufacturer's instructions.

#### **3.7.2 Analysis of the recellularized scaffolds**

By the end of day 7 of the incubation time, recellularized PCKS were fixed in 4% PFA overnight at RT. Samples were histologically processed according to the protocol in Table S 14 and embedded

in paraffin. SYNTH scaffolds were stained as whole scaffolds without embedding in paraffin, as paraffin slices tended to fall off the slide during deparaffinization and staining.

#### 3.7.2.1 Investigation of migration depth of seeded cells

In order to study the migration of seeded cells towards the inner regions of the recellularized PCKS, serial paraffin sections were prepared. The PCKS were cut at a thickness of 10  $\mu\text{m}$  from three distinct layers: the first layer, second layer, and third layer.

A consistent distance of 150  $\mu\text{m}$  was maintained between each of these layers covering a maximum depth of 300  $\mu\text{m}$  of each scaffold. The paraffin sections were deparaffinized as described in Table S 13. After that the sections were mounted with Fluoromount-G containing DAPI for nuclei visualization. Imaging was performed using a fluorescence microscope. Multiple images (4-7 images) were taken for each slice at different positions in the kidney cortex using the 10x objective. The number of nuclei in all images was counted automatically using the “cell detection” function at a threshold of 8000 in QuPath version 0.2.3. The number of nuclei in each imaged position was normalized to the area of the tissue at the respective position. Tissue areas were measured by ImageJ as indicated in section 3.1.2.

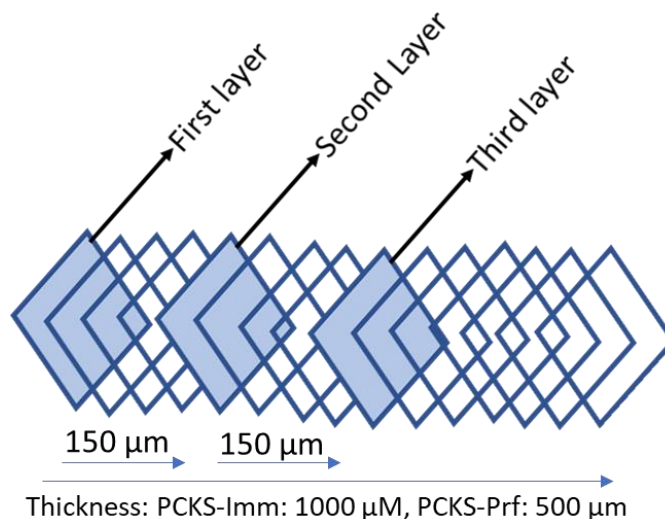


**Figure 6: Schematic representation of the serial paraffin sections** prepared for the investigation of the migration depth of seeded cells

### 3.7.2.2 Investigation of tight junction formation and cell seeding specificity

#### Immunofluorescence staining

Immunofluorescence was carried out on paraffin sections from recellularized PCKS and whole SYNTH scaffolds. Paraffin sections measuring 5  $\mu\text{m}$  in thickness and stained with zonula occludens-1 (ZO-1) were obtained from the third layer. Additionally, paraffin sections measuring 10  $\mu\text{m}$  in thickness and stained with Col-IV were obtained from both the second and third layers. After deparaffinization, the sections were washed with 0.1% Tween in PBS (PBST) for 5 min. For antigen retrieval, the sections were incubated with sodium citrate buffer (pH 6) at 92 °C for 20 min.

The sections were then washed 3x for 5 min with PBST. Next, the sections were blocked for 30 min with 5% bovine serum albumin (BSA) in PBST and for 30 min with 5% normal goat serum (NGS) in PBST. Primary antibodies were applied for 16 h at 4 °C. The primary antibodies were diluted at a 1:100 ratio in a solution consisting of 1% normal goat serum (NGS) in PBST as follows: polyclonal rabbit anti Col-IV antibody and polyclonal mouse anti ZO-1 antibody. The slides were then washed 4x for 5 min in PBST. After that, Col-IV sections were incubated with Alexa Fluor™ 647 goat anti-Rabbit secondary antibody, and ZO-1 sections were incubated in Alexa Fluor 647 goat anti-Mouse secondary antibody both in 1:200 dilution for 1 h at RT. After washing 4x for 5 min in PBST, the sections were mounted with Fluoromount-G (DAPI). Imaging was performed using a confocal microscope. Immunofluorescence for whole SYNTH scaffolds followed the same protocol with minor modifications. Small pieces of the scaffolds were prepared by cutting them into approximately 1 mm<sup>2</sup> pieces using a scissor. While the washing step after antigen retrieval was increased to 4x for 5 min, the washing steps after the incubation with all antibodies was increased to 5x for 5 min.

#### Determination of ZO-1 intensity

Fluorescence intensity of ZO-1 in recellularized PCKS was measured using QuPath version 0.2.3. After creating a full image annotation, the “cell detection” function was used to detect nuclei, which were then classified into cells with and without a ZO-1 signal using the “create single measurement classifier” function. A script was created to automate the process of nuclei and ZO-1 detection in all images. QuPath provided a measurement of the available ZO-1 intensity around each single nucleus, which was normalized to the area of cell nuclei.

#### Investigation of cell seeding specificity

The approach involves counting the number of seeded cells inside the BC relative to the total number of seeded cells, serving as an indicator of specific recellularization. To visualize the different functional units of the kidney, recellularized PCKS were stained with Col-IV. Artificial neural networks (ANN) were used for the automatic identification of the BCs. Specifically, deep learning-based algorithms for cell segmentation were employed for the analysis of Col-IV fluorescence images of recellularized scaffolds. The tissue area in the images was first annotated using OTSU thresholding in ImageJ. To ensure accurate automatic detection of BCs, Cellpose "Cyto" model was trained using 70 images of the Col-IV stained slices, where the BCs were manually annotated using QuPath (Version 0.43). The training process was conducted for 400 epochs or until the loss function no longer decreased, following the instructions provided by the Mouseland/Cellpose generalist algorithm. The BCs were then automatically identified and annotated in the remaining images using "Cellpose". The BC annotations were then imported into QuPath for further analysis. To ensure accuracy, all automatically identified BCs were confirmed by two investigators. Cells outside and inside the BCs were automatically counted using QuPath and the cell counts were normalized to the total imaged tissue area determined by QuPath.

### **3.8 Scoring system**

To facilitate a comprehensive evaluation of qualitative (microscopy) and quantitative (assays) data, a scoring system was introduced. It consists of two categories: decellularization evaluation and recellularization evaluation, each encompassing several subcategories (Table S 15).

For the decellularization evaluation, a slightly modified version of the scoring system developed by Fischer et al. [91] and Caralt et al. [124] was used to quantify descriptive histological microscopy data obtained from H&E stained sections. The decellularization category is divided into three subcategories (Table S 15). The first two subcategories: "general appearance" and "structures" include several parameters for histological evaluation and converting microscopic information into quantitative data. Three laboratory members experienced in histology and blinded to the samples performed the evaluation and scoring. Additionally, the "general appearance" category involved an assessment of scaffold shrinking, quantified using ImageJ as outlined in section 3.1.2. Shrinking refers to the reduction in NCS within the scaffold due to the impact of decellularization reagents. In the third subcategory "composition", quantitative data obtained from the biochemical assays were translated into scores allowing the calculation of a composition score that can be compared with the histology score

(see section 12.4 for a detailed description). On the other hand, the recellularization category focuses solely on quantitative data from the medium and scaffold analysis subcategories. Similar to the decellularization evaluation, these data were translated into scores, enabling the calculation of a total score for both decellularization and recellularization. Scores were assigned with “1” signifying the worst result to “4” for the best result achieved. The category score is calculated by averaging the scores in the respective category. The total score is the average of the decellularization and recellularization scores.

### **3.9 Reactivity of PBMCs to native and decellularized kidneys**

Human peripheral blood mononuclear cells (PBMC) were isolated from Buffy coats as described in section 12.10. PBMCs were placed into a 96 well plate suitable for suspension cells, at a total of  $1 \times 10^5$  cells per well in 300  $\mu$ l RPMI 1640 culture medium supplemented with 10% FBS. These cells were exposed to 0.5 mg of native or decellularized kidney homogenates, which correspond to scaffolds decellularized according to the SDS1% protocol (section 3.4). PBMCs were also incubated with 20 ng/ml of recombinant human interleukin 2 (IL-2), which served as a positive control. Meanwhile, cells cultured without any stimulating agent served as the negative control. Additionally, PBMCs were also exposed to 6% ethanol in culture medium, acting as a model for cell damage. The PBMCs were incubated at 37 °C, with conditions set at 5% CO<sub>2</sub> and 95% humidity. After 48 h of incubation, resazurin and LDH assays were conducted as described above.

### **3.10 Statistical analysis**

Statistical analysis within this study were performed with non-parametric tests, since all groups are not normally distributed as shown by the Shapiro-Wilk normality test. The data of the biochemical assays (DNA, GAG, collagen) were compared using the Mann-Whitney U-test. On the other hand, all other statistical comparisons were done using Kruskal-Wallis test followed with Dunn’s test. A p-value lower than 0.05 was considered significant. Statistical analysis was performed using GraphPad Prism version 6 for Windows, GraphPad Software, USA.

## 4 Results

### 4.1 Optical characteristics of PCKS after HHP treatment

An initial experiment was conducted to investigate the impact of a wide range of HHP levels on the optical characteristics of PCKS after HHP treatment and upon decellularization.

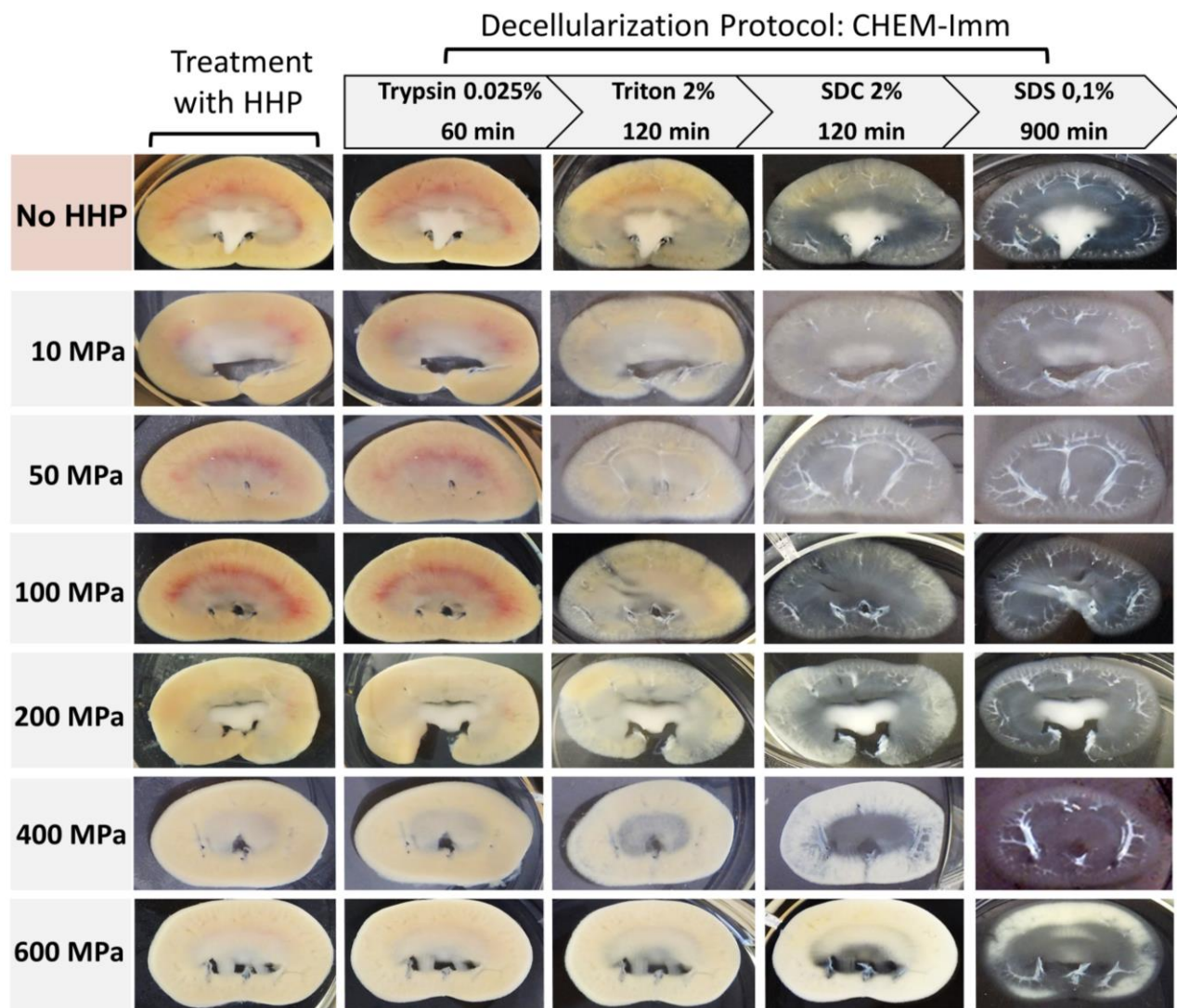


**Figure 7: Optical characteristics of PCKS following HHP treatment at varying pressures (10 - 600 MPa).** Documentation of each stage of decellularization (CHEM-Imm protocol), highlighting the influence of HHP on tissue color and decellularization. Pressure levels are denoted within gray boxes, and the decellularization protocol is represented by gray arrows (n = 2)

The primary objective was to identify potentially effective pressure levels for the decellularization process. PCKS were exposed to a range of pressure levels from 10 to 600 MPa. It became evident

that decellularization was considerably less effective when PCKS were treated with pressures of 400 MPa and 600 MPa. This was optically apparent as HHP treated PCKS exhibited a transparent appearance, indicating more complete decellularization when subjected to pressures below 400 MPa. In contrast a somewhat whitish or reddish coloration was observed in PCKS treated with 400 and 600 MPa after SDC and SDS treatments, respectively (Figure 7). Consequently, for subsequent experiments, HHP treatment of PCKS was restricted to pressure levels of 50, 100, and 200 MPa.

### **4.2 Histological assessment of PCKS after physical treatment**

To better understand potential effects of the physical treatment on the structural integrity of kidney slices, PCKS were investigated histologically directly after the physical treatment and without further decellularization with CHEM-Imm. The physical treatment of PCKS by HHP or FTC caused shrinking of the kidney slices such that the total area of NCS was smaller than prior to the physical treatment. The correlation between the intensity of the physical treatment method (HHP or FTC) and the reduction of NCS in kidney tissue was evaluated by quantifying relevant areas in the histological sections (Figure 8). The reduction in NCS is clearly visible in several vital structures of the kidney. The renal corpuscle in both 6 FTC and HHP (600 MPa) treated PCKS lost its distinctive Bowman space, such that the visceral layer of the BC and parietal layer of the glomerulus are almost in touch (Figure 8B, C, yellow arrows). While the lumen of the tubules completely disappeared in 6 FTC treated PCKS, it was partially maintained in PCKS treated with 600 MPa (Figure 8B, C, black arrows). Moreover, the pink color representing eosin appeared lighter in HHP compared to FTC treated PCKS, in which it appears more intense and darker. This could be attributed to a less infiltration of H&E due to HHP-induced compression. For a precise quantification, the images were analyzed by ImageJ. It was revealed that FTC-induced reduction of NCS is more significant than that induced by HHP. The percentage of remaining NCS after 1 FTC is 16%, while it is 83% under the highest applied pressure (600 MPa).

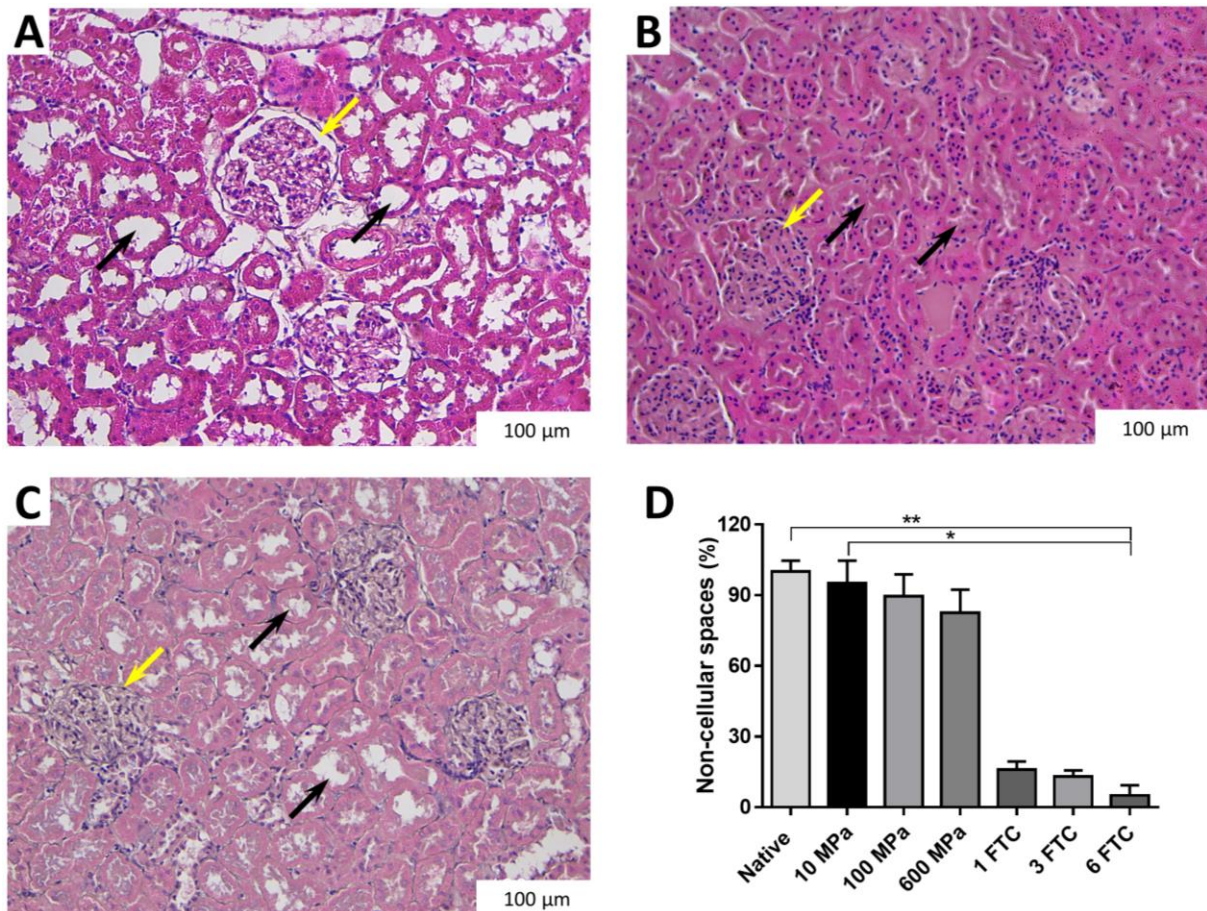
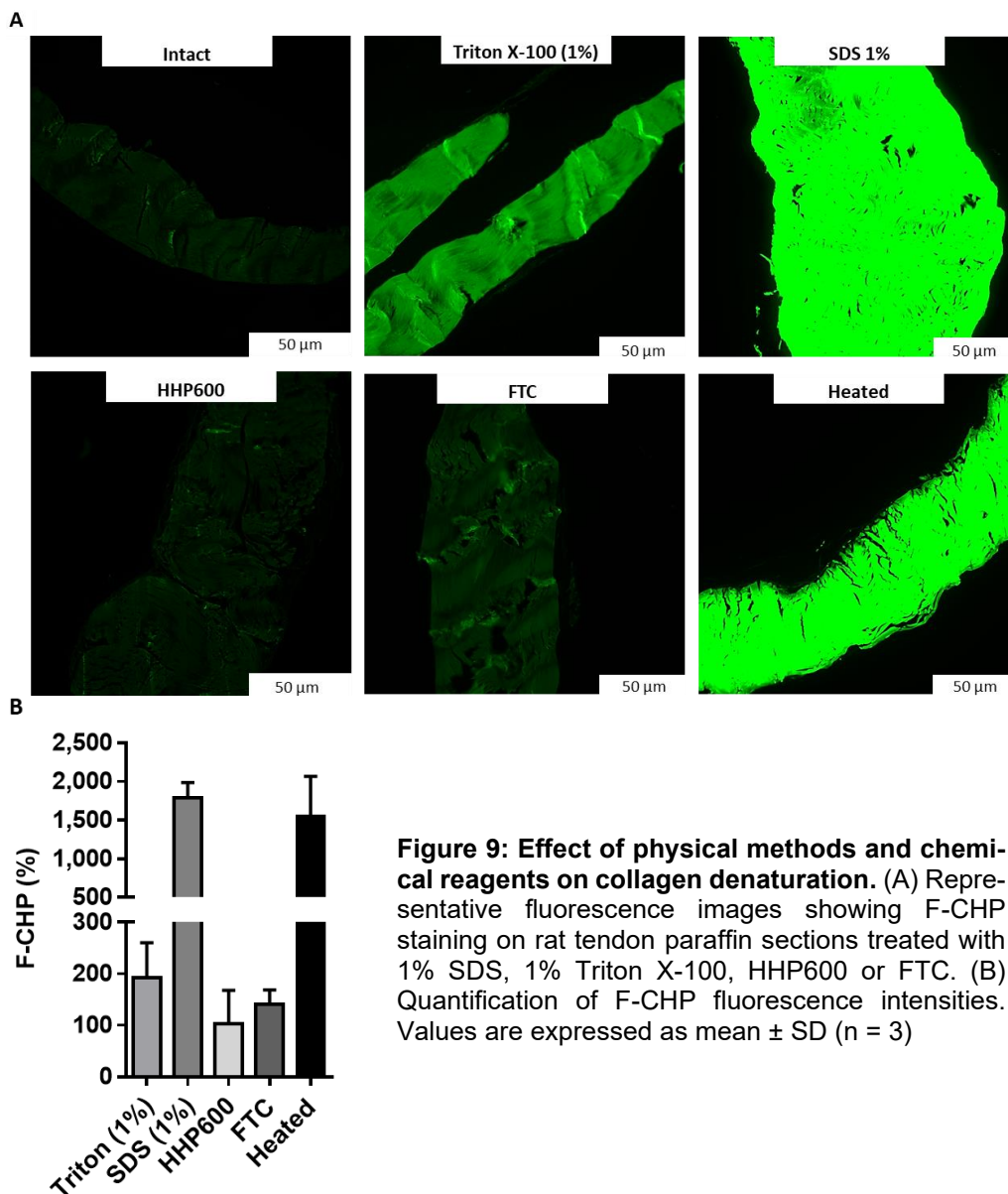


**Figure 8: Evaluation of NCS in H&E stained PCKS after HHP and FTC.** (A) Native PCKS with arrows pointing at normal NCS of the BC (yellow arrows) and the lumen of the tubules (black arrows) (B) and (C) PCKS treated with FTC and HHP respectively with arrows pointing at compressed NCS of BC and lumen of the tubules (D) NCS quantification. Groups were compared with Kruskal Wallis test followed by a pairwise analysis with Dunn's test against the native kidney. Values are expressed as mean  $\pm$  SD (native and HHP:  $n = 5$ , FTC:  $n = 3$ ). Significant differences are indicated by ( $*p \leq 0.05$ ) and ( $**p \leq 0.01$ )

### 4.3 Assessment of the effect of physical treatment on collagen

Since clear effects on tissue integrity of kidney slices were exhibited by HHP and FTC, the next step was to assess potential effects of these treatments on collagen, the main component of the ECM. Therefore, rat tendons were first investigated as an easily obtainable and highly pure collagen material to compare the effect of physical treatments. The influence of collagen denaturation by FTC and HHP was investigated and compared with those induced by chemical reagents (1% SDS and 1% Triton X-100) commonly employed in decellularization processes. Collagen denaturation was quantified using F-CHP, which selectively binds to denatured collagen sites, with the measurement based on fluorescence intensity.



The positive control, consisting of tendons heated to 60 °C, exhibited a substantial 1550% increase in intensity compared to untreated tendons. Surprisingly, tendons treated with 1% SDS revealed even more substantial denaturation, with an 1800% increase in intensity, underscoring its potency in the context of decellularization (Figure 9B). In contrast, Triton X-100 produced milder effects, resulting in a 200% increase in intensity. On the other hand, HHP treatment at 600 MPa was found to induce almost no collagen denaturation, while FTC treatment led to slight denaturation, with an intensity increase of 140% compared to untreated tendons (Figure 9B). These findings show the

varying impacts of chemical and physical treatments on the collagen structure, with SDS being a highly aggressive reagent, Triton X-100 exhibiting milder effects, and HHP and FTC causing only minimal to modest denaturation.

### 4.4 Immersion decellularization

This study aimed at better understanding the effects of physical treatments (HHP, FTC or UBS) on the overall efficacy of chemical-based decellularization (CHEM-Imm) of PCKC-Imm.

#### 4.4.1 Quantification of DNA, GAG and collagen

To assess the impact of the different decellularization methods on critical ECM components, the retention of GAG and collagen contents was evaluated, and the residual DNA content was analyzed to determine the effectiveness of each method in DNA removal (Figure 10). Treatment with HHP50-Imm followed by CHEM-Imm resulted in the least effective removal of DNA from decellularized scaffolds with a 79% reduction of the total DNA in native PCKS. In contrast, FTC-Imm yielded the highest reduction (96%), followed by UBS30-Imm (95%) and UBS60-Imm (94%) (Figure 10A). Furthermore, physical pretreatments were expected to enhance the decellularization by CHEM-Imm and lead to a higher reduction of DNA. However, both HHP50-Imm and HHP100-Imm resulted in a DNA content higher than CHEM-Imm, in spite of the pretreatment with HHP. This suggests that HHP treatment prior to CHEM-Imm seems to hinder DNA removal, although this effect was statistically not significant. On the other hand, the residual DNA content in FTC-Imm scaffolds was significantly lower than in CHEM-Imm scaffolds.

With respect to GAGs, it was found that all methods resulted in a significant loss compared to the native tissue (Figure 10B). In contrast, collagen content in decellularized PCKS-Imm was generally preserved (Figure 10C). Broadly speaking, there is an inverse correlation between the level of applied HHP and the effectiveness of removing DNA as well as retaining GAGs and collagen, such that the amounts decrease with increasing the pressure. Hence, HHP200-Imm has the lowest DNA, GAG and collagen contents among the other HHP treatments (HHP50-Imm and HHP100-Imm). On the other hand, both UBS30-Imm and UBS60-Imm resulted in the lowest amounts of retained GAGs (14% and 17%) despite securing the first and third highest composition scores, which is primarily due to the efficient DNA removal with these protocols. Moreover, HHP200-Imm and UBS60-Imm achieved comparable levels of DNA removal and GAGs preservation (Figure 10A, B).

## 4 Results

Interestingly, the retained amounts of GAGs and collagen in scaffolds decellularized with the FTC-Imm protocol were around 26% and 97% respectively, which is strikingly similar to the amounts retained in CHEM-Imm scaffolds. Among the physical treatments, FTC-Imm appears to better support the decellularization by CHEM-Imm, with regards to achieving the highest DNA removal while best retaining GAG and collagen levels leading to the second highest composition score after UBS30-Imm (Figure 10D).

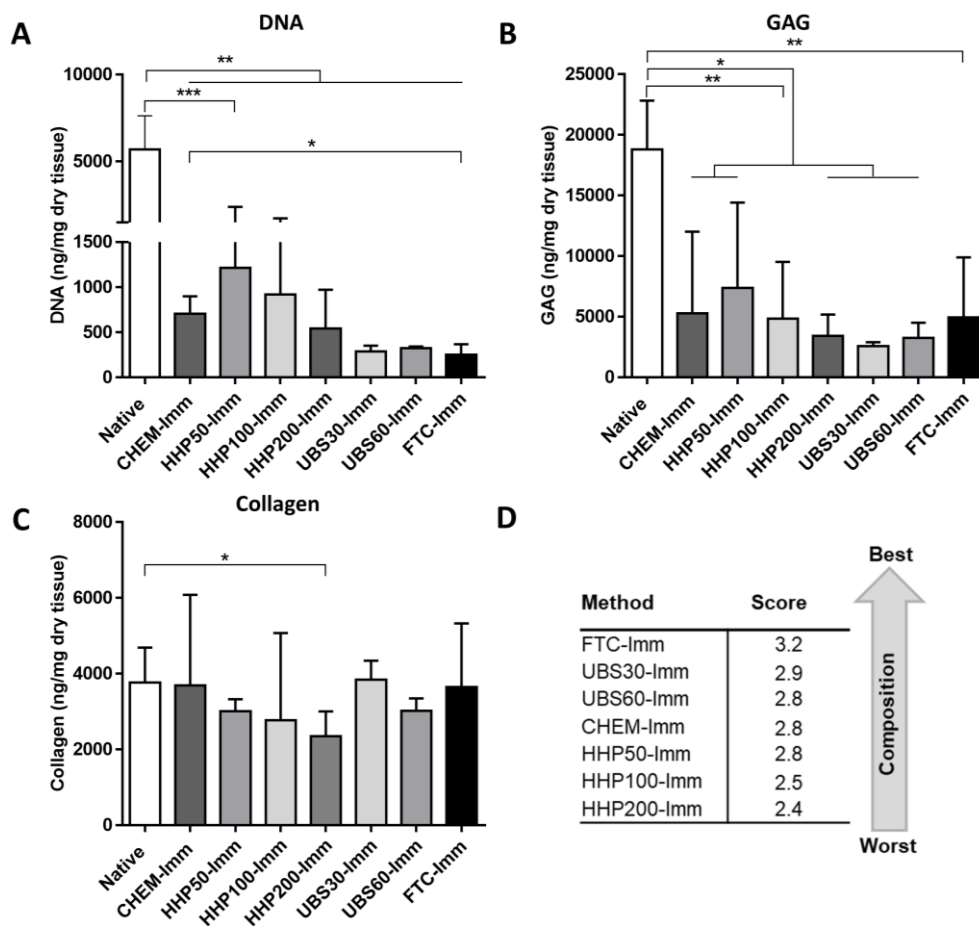


**Figure 10: Characterization of decellularized PCKS-Imm for removal of DNA and retention of GAG and collagen.** (A) DNA content (B) GAG content (C) Collagen content (D) Composition scores. Data were analyzed with Mann-Whitney U test ( $n \geq 3$ ). Values are expressed as mean  $\pm$  SD ( $n \geq 3$ ). Significant differences are indicated by (\* $p \leq 0.05$ ), (\*\* $p \leq 0.01$ ) and (\*\*\*) $p \leq 0.001$ )

#### 4.4.2 Histological evaluation of decellularized PCKS-Imm

The tissue processing protocol described in Table S 12 resulted in a significant shrinkage of the scaffolds, causing them to lose approximately 70-80% of their original size. This made it challenging to identify the structures after H&E staining. Consequently, an optimized protocol for dehydration and paraffin infiltration was used (Table S 14). It involved utilizing a different tissue processing machine that applies cycles of pressure and vacuum during incubation in the various reagents, which played a crucial role in preventing significant shrinkage.

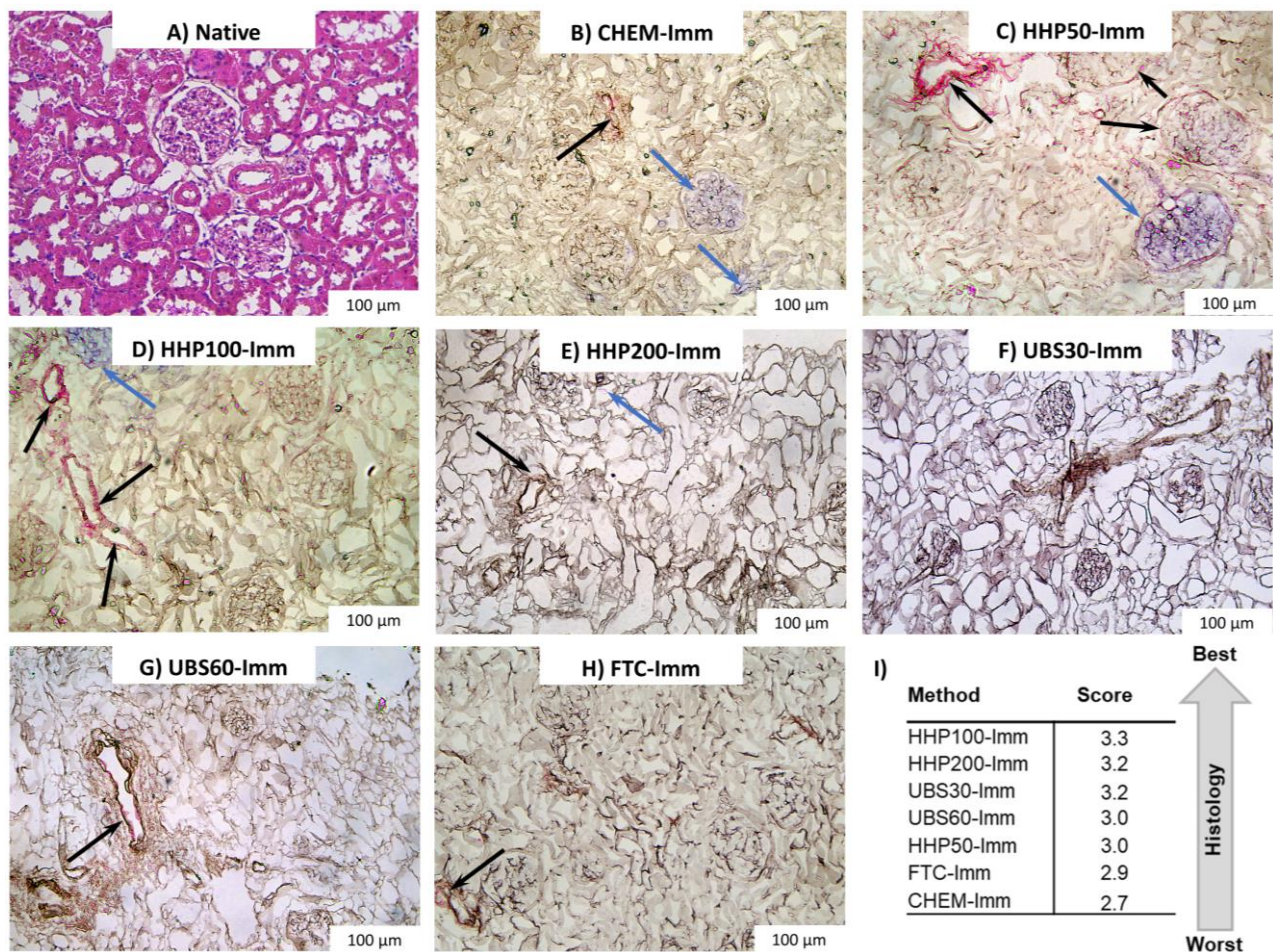


**Figure 11: Histological analysis of H&E stained native and PCKS-Imm.** (A) Native kidney tissue and PCKS-Imm decellularized by (B) CHEM-Imm (C) HHP50-Imm (D) HHP100-Imm (E) HHP200-Imm (F) UBS30-Imm (G) UBS60-Imm and (H) FTC-Imm. Arrows point at remaining nuclear (hematoxylin, blue arrow) and cytoplasmic material (eosin, black arrow). Scale bar: 100 µm. (I) Histology scores. Statistical analysis involved Kruskal Wallis test, followed by Dunn's test for pairwise comparisons against the native kidney. CHEM, HHP50, HHP200 and FTC: n = 5, UBS60: n = 4, HHP100 and UBS30: n = 6

In general, the histological assessment showed gross preservation and no evidence of complete breakdown of structures in PCKS-Imm decellularized by any of the methods tested here (Figure 11). As far as evident by H&E staining, removing cytoplasmic material was harder than removing nuclear material. Moreover, hardly any nuclei were visible in any of the scaffolds except for those treated with HHP, which resulted in incomplete removal of cytoplasmic and nuclear materials (Figure 11C, D, E). This could be an indication that decellularization of PCKS-Imm by immersion is an inhomogeneous process. In contrast, UBS-assisted decellularization demonstrated the lowest levels of remaining cytoplasmic material implying a more homogenous decellularization. The highest histology scores were achieved by HHP100-Imm, HHP200-Imm and UBS30-Imm while FTC-Imm and CHEM-Imm achieved the lowest scores (Figure 11I). The low score of FTC-Imm is attributed to inferior performance in the structural analysis category. On the other hand, CHEM-Imm demonstrated low scores in both categories (general appearance and structures) (Figure S 1A, B).

### **4.4.3 Evaluation of the ultrastructure in decellularized PCKS-Imm**

To assess the effects of the treatments on the ECM ultrastructure, scaffolds from five decellularization protocols were selected for further examination with SEM (Figure 12). The scaffolds were virtually devoid of cells but retained the honeycomb appearance of their underlying basal membranes and accompanying ECM in all protocols. Moreover, inspection at higher magnifications revealed the striated appearance of the basal membranes on the luminal side of the tubules, which is characteristic for intact kidneys (Figure S 11), and showed that it was best preserved in CHEM-Imm scaffolds. On the other hand, while HHP200-Imm and FTC-Imm resulted in partial preservation of the striated appearance of the luminal basal membrane, UBS30-Imm showed remarkably large wrinkle formation, possibly indicating a structural collapse or shrinking of associated ECM components (Figure 12, red arrows). Furthermore, the microstructure of the glomeruli was generally well preserved in CHEM-Imm, FTC-Imm and HHP200-Imm scaffolds. However, UBS30-Imm and UBS60-Imm demonstrated partially damaged and smaller glomeruli, which were even smaller in UBS30-Imm scaffolds (Figure 12, blue arrows).

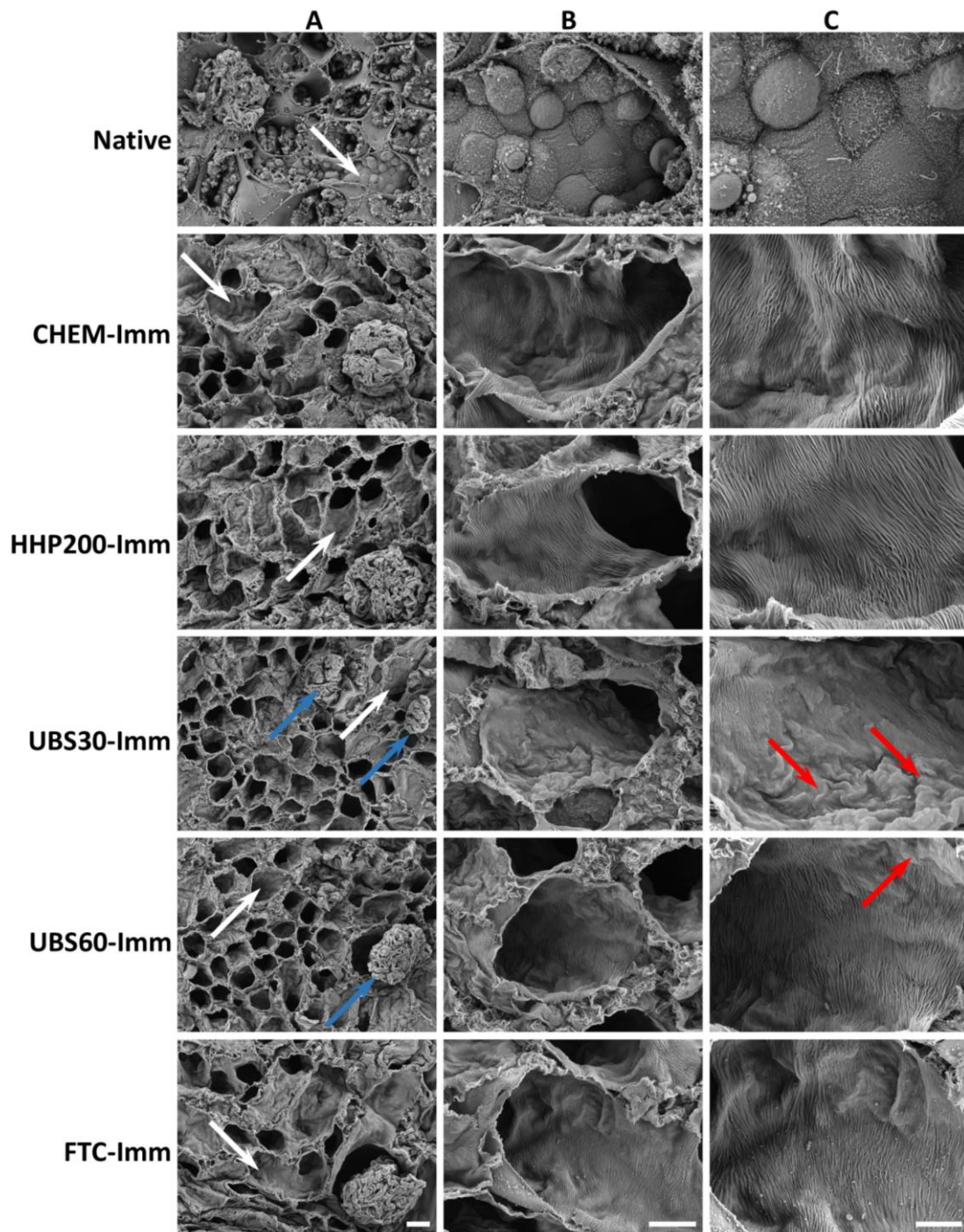



**Figure 12: Scanning electron microscopy of native and PCKs-Imm decellularized by immersion.** Representative images are divided into three columns at different magnifications: (A) 500x, (B) 1000x and (C) 2000x. White arrows represent the magnified areas in columns B and C. Severe wrinkles on the basal membrane in the luminal side of the tubules as shown in UBS30-Imm and less severely in UBS60-Imm (C, red arrows) with glomeruli (blue arrows) also partially damaged in both conditions. Scale bars: (A) 20  $\mu\text{m}$ , (B) 10  $\mu\text{m}$ , (C) 5  $\mu\text{m}$ , n = 1

#### 4.4.4 Immersion decellularization score

The scoring system enabled the combination of quantitative assays data (composition score) with subjective microscopy data (histology score) into a decellularization score. The highest scores were achieved by UBS30-Imm and FTC-Imm, both at approximately 3.1 (Figure 13). While no statistically significant differences were found among the different methods, HHP50-Imm and HHP100-Imm achieved the lowest scores of 2.9 and 2.7 respectively.

Method	Score
FTC-Imm	3.1
UBS30-Imm	3.1
UBS60-Imm	3.0
HHP200-Imm	2.9
HHP100-Imm	2.9
HHP50-Imm	2.9
CHEM-Imm	2.7



**Figure 13: Immersion decellularization score** combining composition and histology scores facilitated comparison of immersion decellularization methods

### 4.5 Perfusion decellularization

Building on the findings from PCKS-Imm decellularization by immersion and the results of the scoring system, the research extends to the perfusion decellularization of whole rat kidneys. The goal of the study was to evaluate how the physical pretreatments (FTC-Prf or HHP200-Prf) affected the success of the perfusion decellularization using CHEM-Prf and determine whether they could improve the overall effectivity of the protocol.

Animal and kidney preparation included intravenous heparinization via the tail. This step was crucial to enhance blood coagulation, preventing blockage of blood vessels with coagulated blood, and ensuring the success of the perfusion decellularization.

#### 4.5.1 Quantification of DNA, GAG and collagen

Amounts of DNA, collagen, and GAGs were quantified to assess the maintenance of key ECM components after perfusion decellularization of whole kidneys. Interestingly, the results were generally consistent with the immersion approach. FTC-Prf achieved the highest reduction, followed by CHEM-Prf (Figure 14A). However, the magnitude of DNA reduction in the perfusion approach was much

## 4 Results

less than the immersion approach. For instance, CHEM-Prf, HHP200-Prf, and FTC-Prf achieved only 53%, 39%, and 82% reduction, respectively, while the same methods in the immersion approach achieved 88%, 90%, and 96% reduction, respectively.

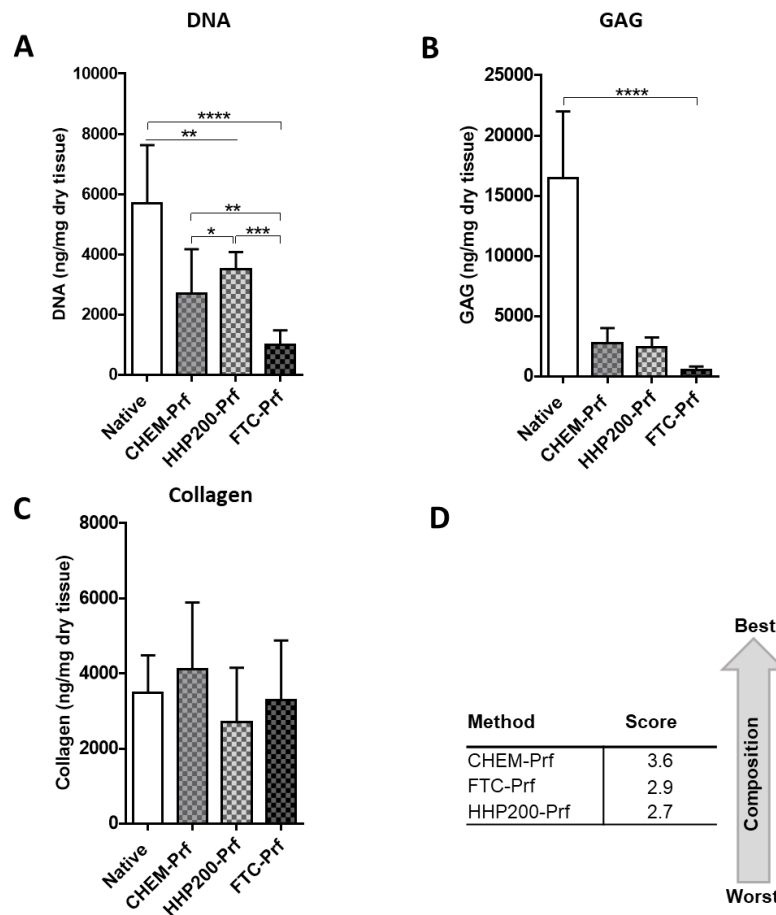


**Figure 14: Characterization of native and decellularized whole rat kidneys for removal of DNA and retention of GAG and collagen.** (A) DNA quantification (B) GAG quantification (C) Collagen content (D) Composition scores. Data were analyzed with Mann-Whitney U test and values are expressed as mean  $\pm$  SD ( $n \geq 6$ ). Significant differences are indicated by (\* $p \leq 0.05$ ), (\*\* $p \leq 0.01$ ), (\*\* $p \leq 0.001$ ) and (\*\*\*\* $p \leq 0.0001$ )

In terms of GAGs, all decellularization methods led to a statistically significant decrease compared to the native kidney, with FTC-Prf resulting in the lowest retention of GAGs (3%) (Figure 14B). However, it is worth noting that FTC-Prf showed less consistent results than its counterpart in the immersion approach, which exhibited a 26% retention in GAGs (Figure 10B). While FTC-Imm had the highest reduction of DNA and maintained GAGs at a similar level to CHEM-Imm, FTC-Prf reduced

GAGs to a much lower level than CHEM-Prf. Thus, it can be concluded that the perfusion approach is more aggressive in terms of GAGs removal.

Moreover, it was found that the use of HHP-Prf resulted in the least effective removal of DNA confirming that HHP treatment prior to CHEM-Prf hinders DNA removal as observed in the immersion approach (Figure 10A). Surprisingly, however, GAGs were removed by HHP200-Prf to a similar extent as CHEM-Prf, suggesting that HHP200-Prf is the least effective method in terms of DNA removal and retention of GAGs (Figure 14A, B). Moreover, decellularized kidneys treated with HHP200-Prf showed lower levels of collagen content compared to native kidneys. On the other hand, collagen content in FTC-Prf scaffolds was almost fully preserved. However, CHEM-Prf scaffolds showed a slight increase in collagen content (Figure 14C).

The results indicate that FTC-Prf is the most effective approach for removing DNA. However, this method led to a significant decrease in GAGs content, even with lower concentrations of SDC and SDS compared to the immersion approach. These findings suggest that further optimization is necessary for the perfusion decellularization of whole kidneys to better retain ECM contents. Therefore, based on the aforementioned results, while CHEM-Prf achieved the highest score in the composition category, HHP200-Prf attained the lowest score (Figure 14D).

### 4.5.2 Perfusate analysis

Although quantification of ECM components (collagen, GAGs) and DNA removal is a widely used endpoint analysis, it involves destructive techniques that prevent using the scaffold for further recellularization experiments. Therefore, in order to obtain more accurate information about the progression of the decellularization process in a non-destructive manner, perfusate samples were collected and analyzed for the presence of proteins, DNA, collagen and GAGs.

To prevent any damage to the vascular network and avoid pressure buildup caused by sudden lysis, the kidneys were first perfused with 0.0025% Trypsin at a flow rate of 0.5 ml/min, allowing for the removal of cellular debris resulting from HHP or FTC treatment. Only after this step was completed, the flow rate was increased to 1 ml/min. Interestingly, the actual perfused volume for all methods was found to be higher than the volume originally set by the pump (theoretical volume). To illustrate, when using a flow rate of 1 ml/min, more than 60 ml of perfusate were circulated within an hour. Additionally, the actual perfused volume varied among methods and individual steps, despite using the same flow rate (Figure 15A).

## 4 Results

This is likely due to pressure changes during decellularization caused by the trafficking of lysed cells in the vasculature. Notably, CHEM-Prf exhibited the highest actual perfused volume (118%) (Figure 15A), suggesting encountering less resistance in the vasculature. Conversely, HHP200-Prf and FTC-Prf showed a lower actual perfused volume than CHEM-Prf (108%).

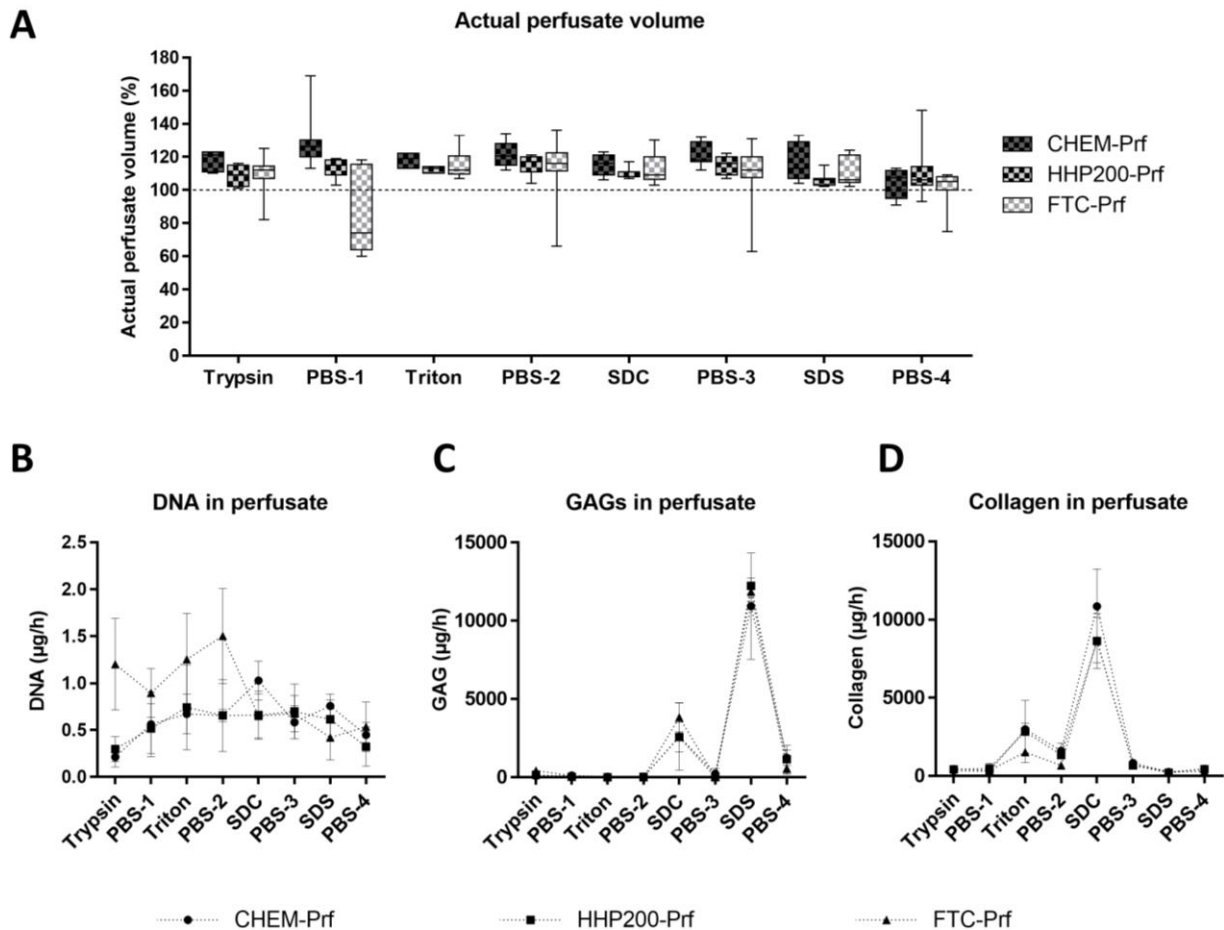


**Figure 15: Evaluation of perfusate samples obtained during the decellularization process.** (A) Actual perfused volume with an orientation line at 100% (theoretical volume). (B) DNA quantification (C) GAG quantification (D) Collagen quantification. Data for the actual perfusate volume are represented as a box and whisker plot, with the line in the middle indicating the median and whiskers from min to max ( $n \geq 7$ ). DNA, GAGs, and collagen data are expressed as mean  $\pm$  SD (actual perfusate volume: CHEM and HHP:  $n = 7$ , FTC:  $n = 9$ ) (DNA, GAG and collagen:  $n = 4$ )

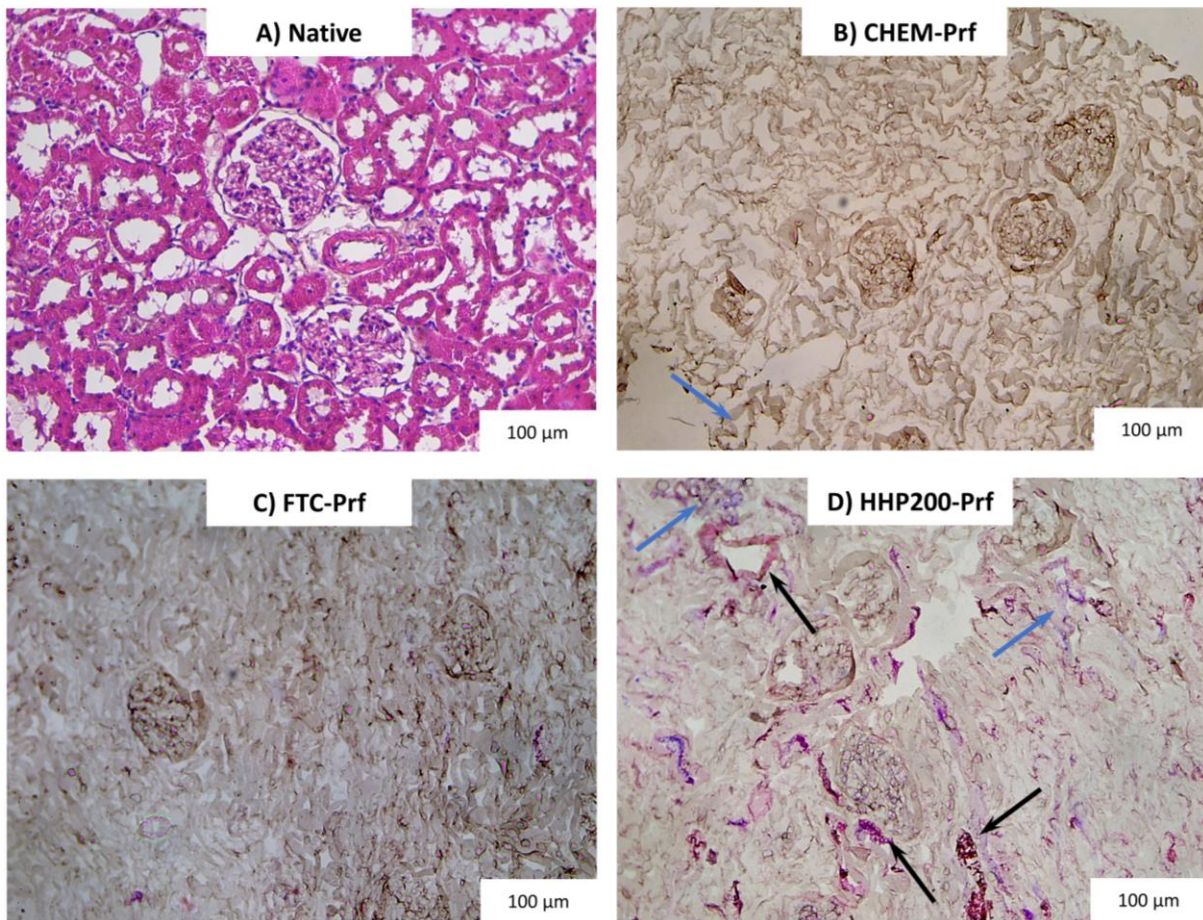
The perfusates from FTC-Prf had the highest levels of DNA, which corresponded with the scaffold analysis. Interestingly, the steps that resulted in the most DNA release differed between the three methods. While CHEM-Prf and HHP200-Prf showed similar levels of DNA release in the early perfusion steps, CHEM-Prf exhibited the highest DNA release during SDC and SDS perfusion. In

contrast, FTC-Prf had the highest amount of DNA release in the initial steps (Trypsin - PBS-2) suggesting a higher level of cell lysis caused by FTC, which dropped considerably during SDC and SDS perfusion (Figure 15B). Thus, possibly indicating that the scaffold has lost the highest amounts of DNA. This was not observed in HHP200-Prf samples possibly due to the HHP-induced compression of the tissues, confirming that FTC is a more effective decellularization method for the tissues analyzed here.

The decellularization process often leads to the loss of important ECM components. In all methods tested, SDS resulted in the highest release of GAGs (70%), followed by SDC (20%) (Figure 15C). On the other hand, SDC caused the highest loss of collagen (60%), followed by Triton X-100 (16%) (Figure 15D). This indicates that different chemicals affect the ECM components differently and these effects were not significantly altered by the employed physical treatments. Although FTC-Prf was the most effective method in terms of DNA removal, it led to a significant decrease in GAGs. Additionally, mostly all PBS washing steps resulted in the release of DNA and ECM components highlighting the importance of washing during decellularization. Therefore, perfusate analysis can be utilized to optimize the decellularization process and reduce residual DNA while better preserving the ECM components.

### **4.5.3 Histological evaluation of decellularized PCKS-Prf**

Histological assessment showed that perfusion decellularization methods preserved the gross structure of the kidneys without evidence of complete breakdown (Figure 16). Similar to the immersion approach, all samples showed no remaining cell nuclei. However, clearing cytoplasmic material proved to be more challenging and received lower scores than removing residual nuclear material (Figure S 16A-E). Moreover, HHP200-Prf resulted in incomplete removal of both cytoplasmic and nuclear materials, earning lower scores in the general appearance category (2.5) compared to its immersion counterpart (3.4) (Figure S 1, Figure S 2). In contrast, FTC-Prf demonstrated the lowest levels of remaining cytoplasmic material and achieved the same score of 3.3 in the general appearance category as the immersion approach. Consequently, FTC-Prf and CHEM-Prf achieved the highest histology scores (3.2), surpassing the immersion approach, which achieved 2.9 and 2.7 respectively. Furthermore, HHP200-Prf achieved a score of 2.8, which is much lower than its immersion counterpart (3.2).



E)

Method	Score
FTC-Prf	3.2
CHEM-Prf	3.2
HHP200-Prf	2.8

Best  
 ↑  
 Histology  
 ↓  
 Worst

**Figure 16: Histological analysis with H&E for whole kidneys decellularized by perfusion.** (A) Native kidney and kidneys decellularized by (B) CHEM-Prf (C) FTC-Prf and (D) HHP200-Prf (E) Histology scores. Arrows point at remaining nuclear (hematoxylin, blue arrow) and cytoplasmic material (eosin, black arrow). CHEM: n = 7, HHP200 and FTC: n = 6

#### 4.5.4 Evaluation of the ultrastructure of PCKS-Prf

The ECM ultrastructure of CHEM-Prf and FTC-Prf scaffolds was examined with SEM (Figure 17). The scaffolds were virtually devoid of cells and the honeycomb appearance of their underlying basal membranes was retained, similar to the immersion approach. Upon inspection at higher magnifications, the striated appearance of the basal membranes on the luminal side of the tubules was best

preserved in CHEM-Prf and partially preserved in FTC-Prf scaffolds. Additionally, the microstructure of the glomeruli was generally well-preserved in both methods.

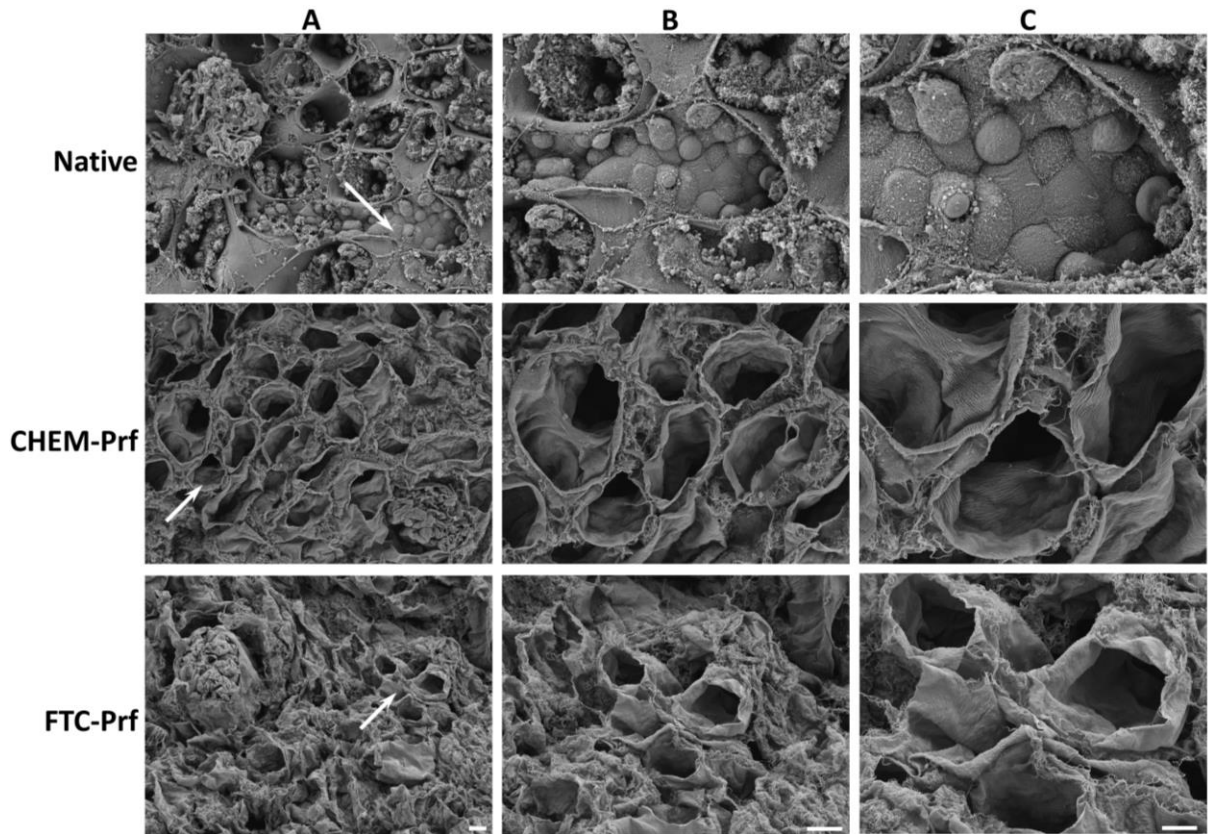


**Figure 17: Scanning electron microscopy of whole kidneys decellularized by perfusion.** Images are divided into three columns. Magnifications: (A) 500x, (B) 1000x and (C) 2000x. White arrows represent the magnified areas shown in columns B and C. Scale bars: (A) 20  $\mu\text{m}$ , (B) 10  $\mu\text{m}$ , (C) 5  $\mu\text{m}$ ,  $n = 2$

#### 4.5.5 Perfusion decellularization score

The decellularization score includes the composition and histology scores. As shown in Figure 18, the highest score was achieved by CHEM-Prf (3.4) followed by FTC-Prf (3.0).

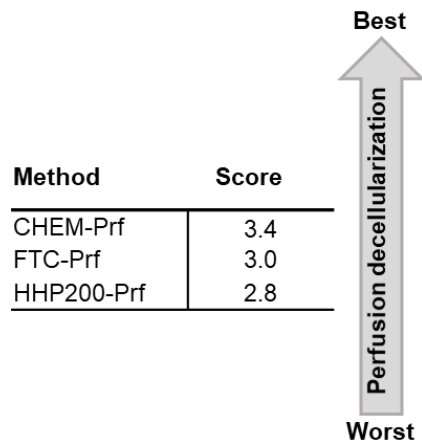


**Figure 18: Perfusion decellularization score** combining composition and histology scores facilitated comparison of perfusion decellularization methods

### 4.6 Characterization of recellularized PCKS-Imm

To determine if there were variations in the ability of decellularized PCKS-Imm to support recellularization, RPTEC/TERT1 cells were seeded onto CHEM-Imm, HHP200-Imm, UBS60-Imm, and FTC-Imm scaffolds, as well as SYNTH scaffolds as described in section 3.6.2.

#### 4.6.1 Macroscopic assessment of recellularized PCKS-Imm

To macroscopically evaluate the scaffolds, photographs were taken before cell seeding and at the end of the recellularization process. Notably, a visible reduction in size and shrinkage of the scaffolds was observed during the incubation period (Figure 19C, D), which could be attributed to the interaction of cells with the scaffold.

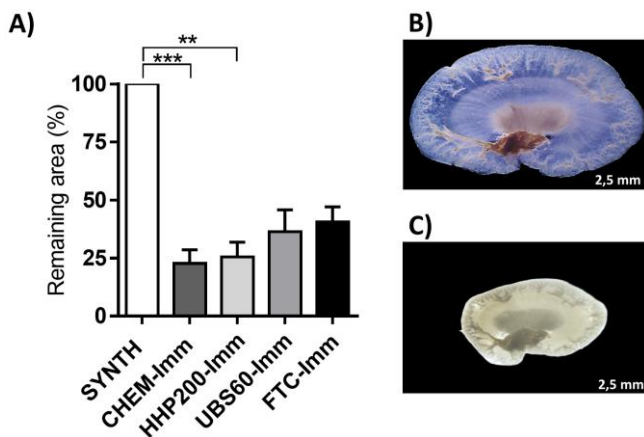


**Figure 19: Macroscopic assessment of scaffold appearance after recellularization.** (A) Quantitative analysis of remaining scaffold area (B) Representative image of a CHEM-Imm scaffold prior to recellularization. (C) Image of the same scaffold after 7 days of recellularization. Scale bar: 2.5 mm

As depicted in Figure 19A, all recellularized scaffolds demonstrated a substantial decrease in size, with FTC-Imm scaffolds exhibiting the largest remaining area at only 40%. Both CHEM-Imm and HHP200-Imm scaffolds showed a statistically significant reduction in size, while UBS60-Imm and FTC-Imm scaffolds exhibited lesser shrinkage. As anticipated, SYNTH scaffolds composed of glass microfibers did not shrink, highlighting the influence of their material properties.

### 4.6.2 Analysis of the cell culture medium

To evaluate cell viability, the reduction of resazurin was utilized, while LDH leakage was employed to assess cell death (Figure 20A, B). A resazurin standard curve was generated (section 3.7.1.1) to establish a correlation between the fluorescence resulting from the reduction of resazurin into resorufin and the corresponding cell numbers responsible for this reduction. A logarithmic regression line was used to calculate the number of cells for the fluorescence values determined from the recellularized scaffolds (Figure S 12).

All of the recellularized scaffolds demonstrated the potential to support human cell adhesion and proliferation over time, regardless of the decellularization method used. It is worth noting that the highest resazurin signal, which indicates persistent cell viability and proliferation within the scaffolds, was consistently observed on the 7th day of incubation (Figure 20A). Although CHEM-Imm appeared to result in the highest cell viability (1.5 times higher on day 7) and growth over time, all physically treated PCKS-Imm that underwent further decellularization with CHEM-Imm exhibited similar viability but lower than those treated with CHEM-Imm alone. Specifically, CHEM-Imm scaffolds showed the highest cell viability, despite having the highest residual DNA compared to all other scaffolds. In contrast, recellularized FTC-Imm scaffolds displayed a lower cell viability than CHEM-Imm, in spite of the lowest residual DNA content and retaining a comparable level of GAG content as CHEM-Imm. Thus, suggesting that CHEM-Imm scaffolds provide a more favorable environment for cell proliferation. Additionally, cell viability in recellularized UBS60-Imm scaffolds was less consistent over time, with viability on day 5 slightly less than that on day 3. It is interesting to note that SYNTH scaffolds exhibited consistent cell growth over time and the highest cell viability among all tested scaffolds, approximately two times higher than CHEM-Imm (Figure 20A).

Nevertheless, it is important to note that the highest resazurin fluorescence value achieved by CHEM-Imm on day 7 corresponded to only 3.5% of the total cells, which were seeded in both cell

## 4 Results

seeding steps ( $1.0 \times 10^6$  cells), as derived by the resazurin standard curve. This comparison indicates that the majority of the cells used in the cell seeding process did not survive.

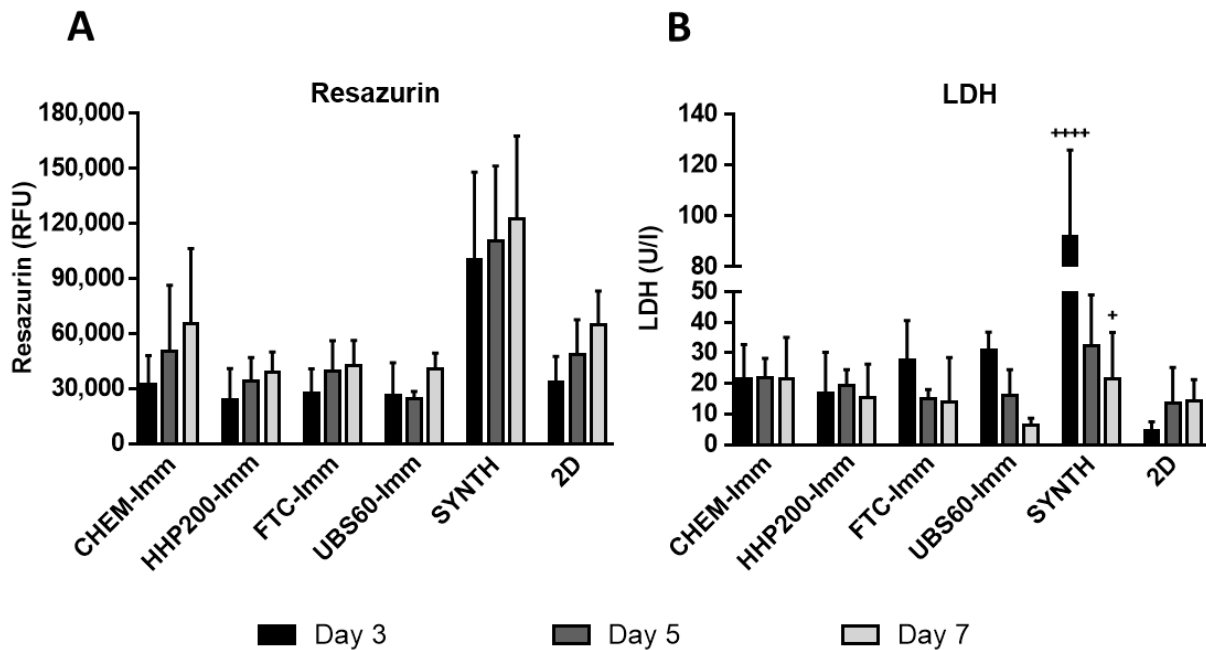


**Figure 20: Analysis of the cell culture medium of recellularized PCKS-Imm.** (A) Resazurin assay (B) LDH concentration. Assays were conducted on days 3, 5, and 7 of the incubation period. Groups were compared using the Kruskal-Wallis test, followed by a pairwise analysis with Dunn's test. Values are expressed as mean  $\pm$ SD ( $n= 2 - 11$ ). Significance levels are denoted by: (\* $p \leq 0.05$ ), and (\*\*\*\* $p \leq 0.0001$ ) represented by symbols as follows: +: SYNTH vs. 2D, \*: FTC vs. SYNTH

Moreover, LDH release was used to monitor cell death (Figure 20B). According to the cell seeding protocol (section 3.6.2), the scaffolds were moved to a new well plate after the second cell seeding step. Therefore, LDH measurements represent only cells that were attached to the scaffolds. Overall, there was a decrease in cell death over time, suggesting that the attached cells were adapting to the scaffolds. This correlated with the increase in resazurin reduction, except for CHEM-Imm, which showed consistent LDH concentration over time. For instance, LDH concentrations in FTC-Imm, UBS60-Imm and SYNTH scaffolds decreased 48%, 80% and 77% respectively, between day 3 and day 7 (Figure 20B). However, HHP-Imm scaffolds exhibited a slightly higher LDH release on day 5 compared to day 3, indicating less adaption of the cells to the scaffold. Additionally, while FTC-Imm and UBS-Imm and SYNTH scaffolds had the highest LDH levels on day 3, they had a lower or similar LDH values than CHEM-Imm on day 7 (Figure 20B). However, the higher LDH in SYNTH scaffolds

## 4 Results

---

can be attributed to the fact that more cells are experiencing cell death, given that more cells were attached to SYNTH scaffolds, as indicated by the resazurin assay.

The metabolic activity of seeded RPTEC/TERT1 cells was analyzed by measuring their glucose consumption and lactate production (Figure 21A, B). Overall, there was an increase in glucose consumption on day 5, followed by a decrease on day 7 (Figure 21B). While CHEM-Imm and HHP200-Imm exhibited a 50% increase in glucose consumption on day 5, both UBS60-Imm and SYNTH scaffolds showed only a 30% increase. Conversely, the highest decrease on day 7 of about 57% was observed in HHP200-Imm scaffolds. However, only FTC-Imm showed a deviation from this trend by exhibiting a 26% higher glucose consumption on day 7 compared to day 5 (Figure 21B). Furthermore, SYNTH scaffolds revealed the lowest glucose consumption. On the other hand, lactate release in CHEM-Imm, HHP-Imm and UBS-Imm followed almost the opposite trend of glucose consumption exhibiting a reduction on day 5 followed by an increase on day 7. The highest increase in lactate release, about 36%, was observed in CHEM-Imm on day 7 (Figure 21A).

The observed increase in lactate production suggests that the cells may be experiencing stress and switching their metabolic pathways towards glycolysis, resulting in the production of lactate as a byproduct. As the highest level of lactate release occurred on day 3, it can be inferred that cells experience a greater initial stress before adapting to the scaffold, which is consistent with the highest LDH levels observed on the same day (Figure 20B). Moreover, seeded SYNTH scaffolds and cells in 2D showed higher lactate levels on day 5 than day 3 indicating a more persistent cell stress when compared to recellularized PCKS-Imm (Figure 21A).

It is noteworthy that cells in 2D displayed equivalent resazurin levels and a similar growth pattern to cells in CHEM-Imm scaffolds, despite only 60,000 cells being seeded in the well plate compared to  $1 \times 10^6$  cells on the scaffolds (Figure 20A). Interestingly, they also showed lower LDH levels compared to CHEM-Imm scaffolds, indicating lower cell death (Figure 20B). Moreover, RPTEC/TERT1 cells in 2D demonstrated the highest levels of lactate on all days, despite their proliferation rate being similar to that of cells in CHEM-Imm scaffolds (Figure 21A). However, cells in 2D exhibited a partially constant and lower glucose consumption compared to all PCKS-Imm (Figure 21B).

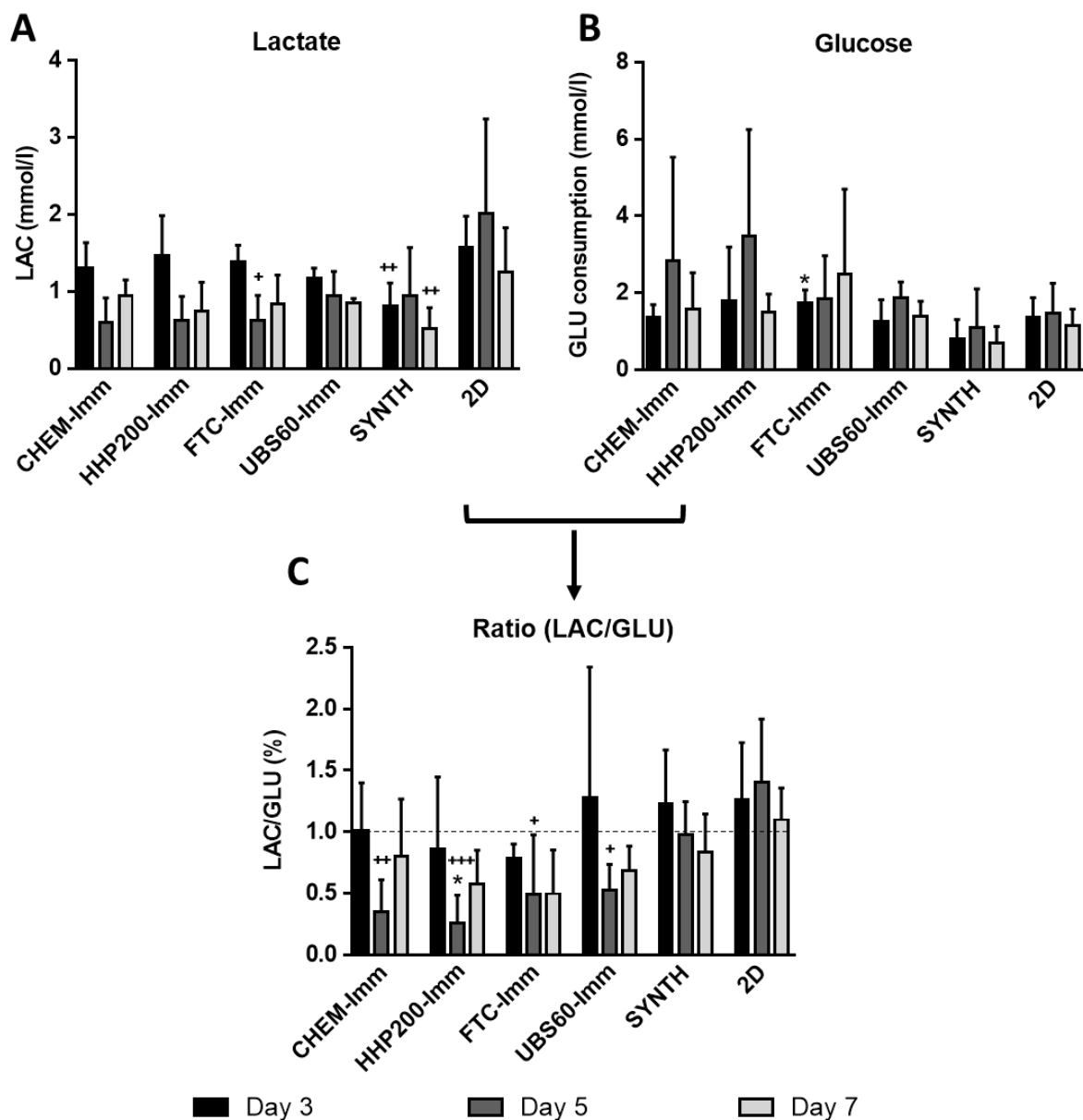


**Figure 21: Analysis of the cell culture medium of recellularized PCKS-Imm.** (A) Lactate concentration (B) Glucose concentration (C) Ratio of lactate to glucose (LAC/GLU) with an orientation line at 1.0. Assays were conducted on days 3, 5, and 7 of the incubation period. Groups were compared using the Kruskal-Wallis test, followed by a pairwise analysis with Dunn's test. Values are expressed as mean  $\pm$ SD (n = 2 - 11). Significance levels are denoted by: (\* $p \leq 0.05$ ), (\*\* $p \leq 0.01$ ) and (\*\*\*) $p \leq 0.001$ ) represented by symbols as follows: +: SYNTH vs. 2D, \*: FTC vs. SYNTH

This suggests that cells in PCKS, even at equivalent resazurin levels compared to 2D, require higher energy to maintain their metabolic activity. Taken together, a ratio of lactate to glucose of less than 1 suggests a primarily oxidative glucose metabolism. SYNTH scaffolds displayed the highest ratio among all PCKS-Imm scaffolds, while FTC-Imm demonstrated the lowest ratio on day 7.

## 4 Results

Thus, supporting the notion that PCKS-Imm scaffolds allowed for sufficient oxygen diffusion. Interestingly, cells in 2D exhibited the highest ratio, indicating a higher dependence on glycolysis.

Combining the outcomes of cell culture medium analysis into a score, as described in Table S 15, aids in identifying the most effective method within this category. Since measurements on day 7 reflect the status at recellularization completion, only these were used to calculate the scores. Figure 22 illustrates that FTC-Imm attained the highest score in this category (3.0), followed by HHP200-Imm (2.7). Conversely, CHEM-Imm achieved the lowest score among all methods of 2.5, despite exhibiting the highest cell viability. This could be attributed to higher LDH concentrations and elevated LAC/GLU ratio values relative to the other methods.

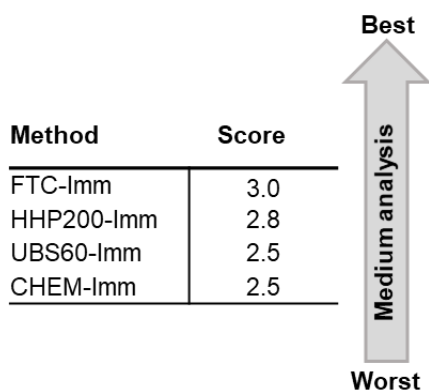


**Figure 22: Medium analysis score for PCKS-Imm scaffolds.** Integration of cell culture medium analysis data from day 7 of the incubation period into scores

### 4.6.3 Analysis of the scaffolds

#### 4.6.3.1 Investigation of migration depth of seeded cells within PCKS-Imm

The extent of migration depth of seeded cells within recellularized PCKS-Imm was investigated. Paraffin sections were obtained from three layers designated as first, second, and third with a uniform spacing of 150  $\mu\text{m}$ , covering up to 300  $\mu\text{m}$  of the scaffold's thickness. DAPI staining was used to visualize cell nuclei, which were counted using QuPath. While all scaffolds facilitated cell migration, the cell migration behavior in FTC-Imm scaffolds was similar to that in CHEM-Imm, with fewer cells observed in the third layer. Conversely, HHP200-Imm and UBS60-Imm showed a different migration pattern, with the highest number of seeded cells found in the second layer and the lowest number in the first layer (Figure 23). Interestingly, HHP200-Imm showed more seeded cells in the second and third layers among all the scaffolds. However, since CHEM-Imm showed the highest levels of resazurin, it is likely that a large proportion of the seeded cells in HHP200-Imm scaffolds represent already dead cells.

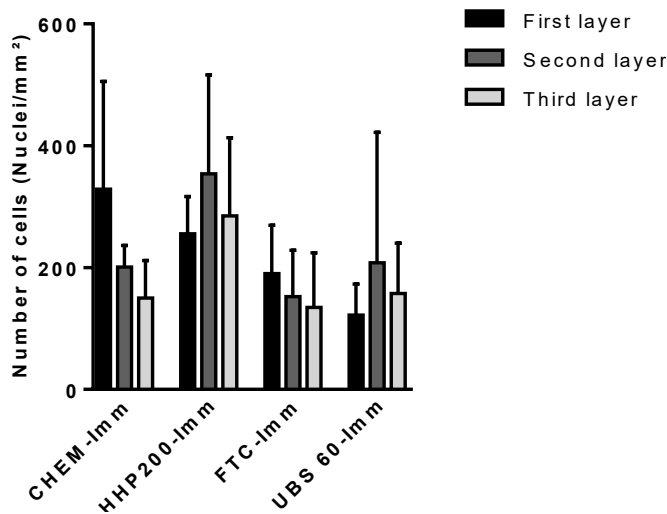


**Figure 23: Investigation of the migration depth of seeded cells within recellularized PCKS-Imm scaffolds.** Values are expressed as mean  $\pm$ SD (n = 4). Nuclei were stained with DAPI

#### 4.6.3.2 Assessment of tight junction formation in recellularized PCKS-Imm

Due to the critical role of tissue organization and cell polarization in kidney function and regeneration, the tight junction protein ZO-1 was investigated in recellularized PCKS-Imm. It was revealed that ZO-1 was produced by seeded cells in all recellularized scaffolds regardless of the employed decellularization method. As depicted in Figure 24A-D, ZO-1 was localized around the cell nucleus, without forming clear connections with neighboring cells. This may be attributed to the short incubation period of 7 days, suggesting that a longer incubation period might promote stronger cell-cell connections. However, the fluorescence intensity of ZO-1 was found to vary among the different scaffolds used in this study, with the highest intensity observed in FTC-Imm scaffolds, which was 2.5 times higher than that in CHEM-Imm (Figure 24E). This observation suggests that the cells had better interaction with FTC-Imm scaffolds, possibly due to its lowest residual DNA content.

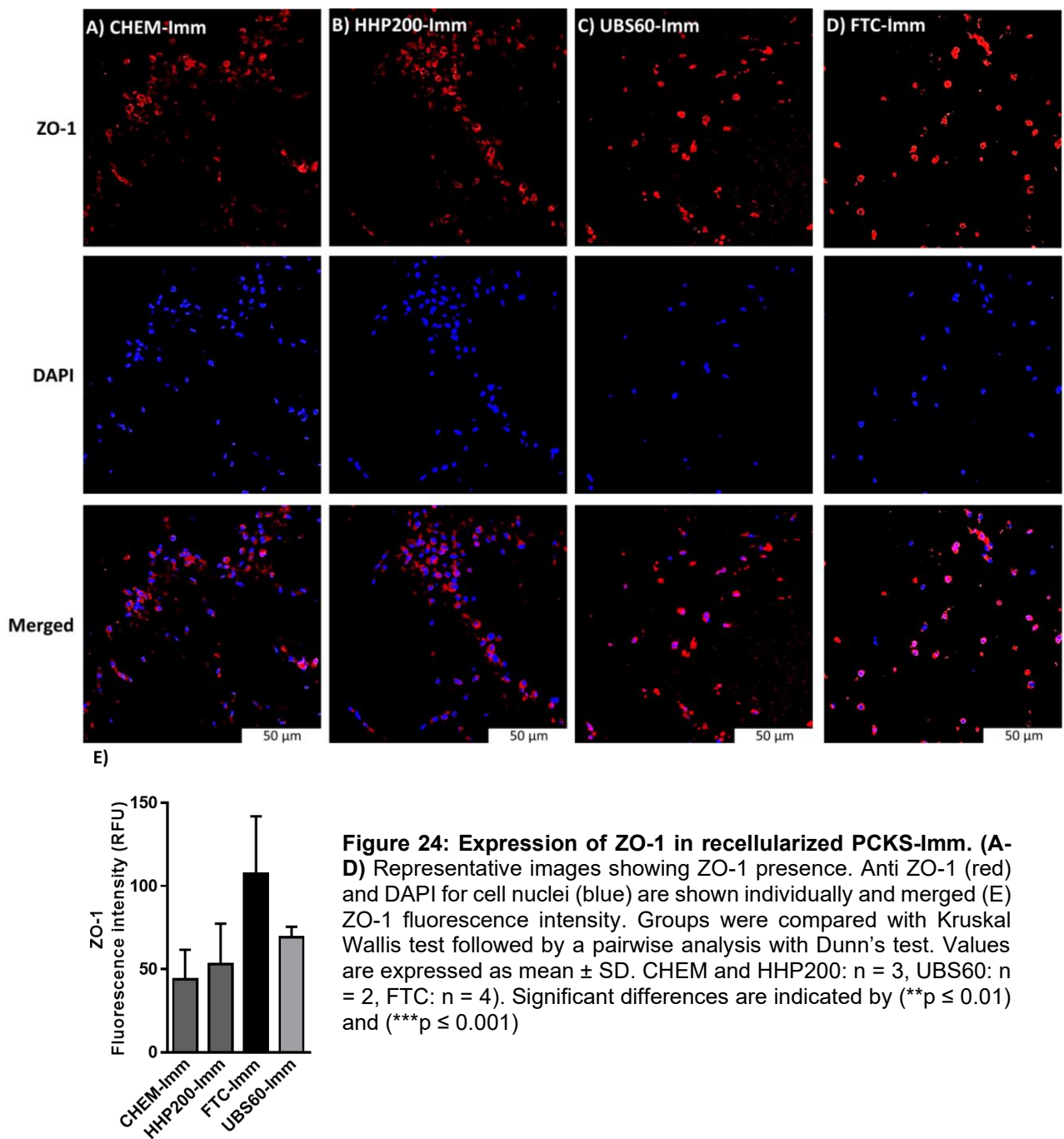


**Figure 24: Expression of ZO-1 in recellularized PCKS-Imm. (A-D)** Representative images showing ZO-1 presence. Anti ZO-1 (red) and DAPI for cell nuclei (blue) are shown individually and merged (E) ZO-1 fluorescence intensity. Groups were compared with Kruskal Wallis test followed by a pairwise analysis with Dunn's test. Values are expressed as mean  $\pm$  SD. CHEM and HHP200: n = 3, UBS60: n = 2, FTC: n = 4. Significant differences are indicated by (\*\*p  $\leq$  0.01) and (\*\*\*) p  $\leq$  0.001)

#### 4.6.3.3 Investigation of cell seeding specificity

To investigate the attachment specificity of seeded cells in decellularized PCKS-Imm, staining with Col-IV was performed to visualize different functional units. Using a neural network algorithm, the BCs were automatically identified. Cells attached inside the BCs were considered to represent non-specific recellularization.

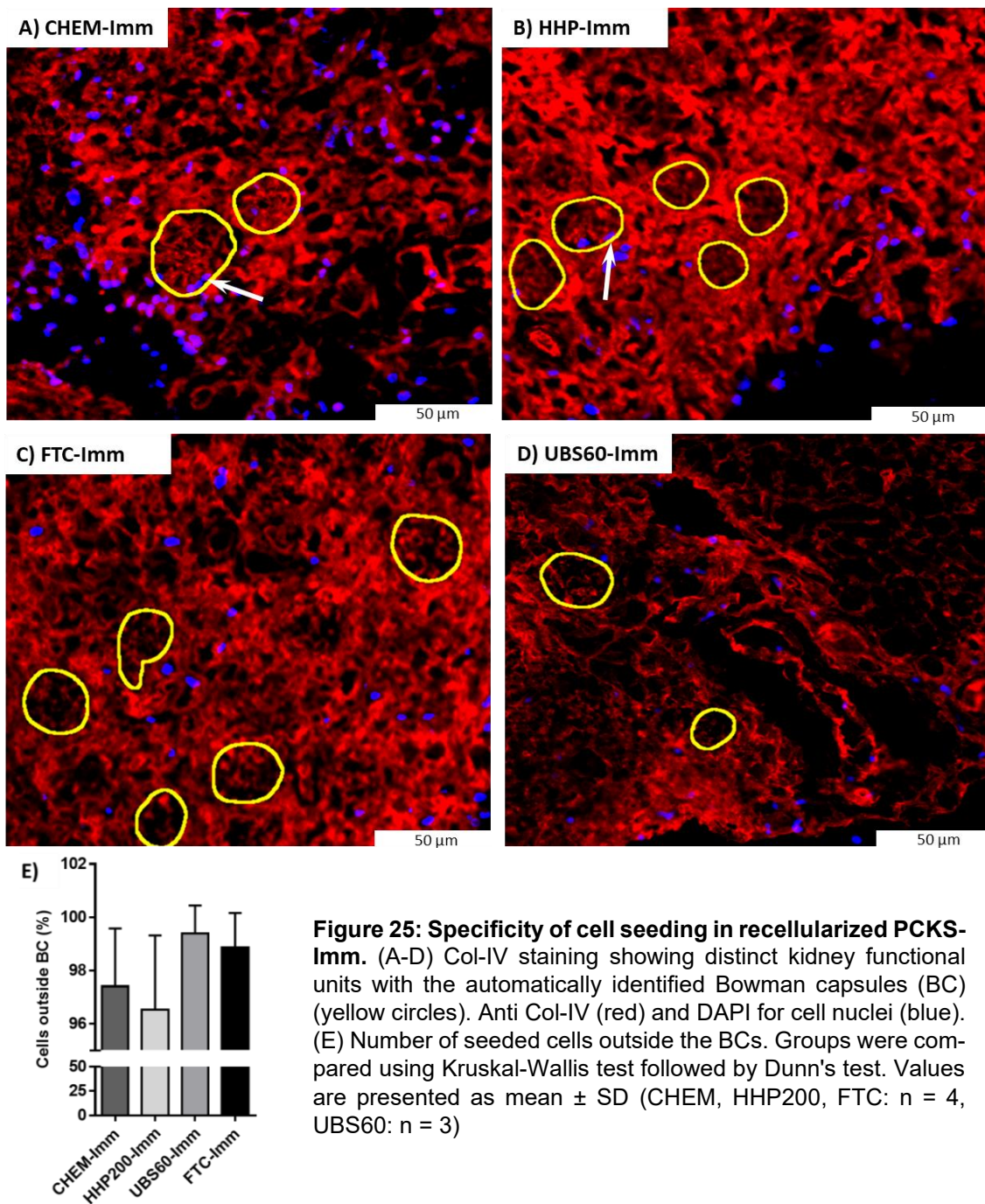


**Figure 25: Specificity of cell seeding in recellularized PCKS-Imm.** (A-D) Col-IV staining showing distinct kidney functional units with the automatically identified Bowman capsules (BC) (yellow circles). Anti Col-IV (red) and DAPI for cell nuclei (blue). (E) Number of seeded cells outside the BCs. Groups were compared using Kruskal-Wallis test followed by Dunn's test. Values are presented as mean  $\pm$  SD (CHEM, HHP200, FTC: n = 4, UBS60: n = 3)


Both UBS60-Imm and FTC-Imm exhibited a higher percentage of attached cells outside the BCs, accounting for 99.4% and 99%, respectively (Figure 25C, D). In contrast, CHEM-Imm and HHP200-Imm had a somewhat lower percentage of attached cells outside the BCs, approximately 97.4% and 96.5%, respectively (Figure 25A, B). Nevertheless, since all methods achieved relatively similar

## 4 Results

---

percentages with no statistical significance, this indicates that all decellularization methods partially preserved the ECM.

The results of scaffold analysis, including ZO-1 assessment and the evaluation of cell seeding specificity, were combined into the scoring system. As shown in Figure 26, FTC-Imm achieved the highest score (3.6) in this category, followed by UBS60-Imm (3.0). In contrast, similar to the medium analysis category, CHEM-Imm obtained the lowest score (2.7).



Method	Score
FTC-Imm	3.6
UBS60-Imm	3.0
HHP200-Imm	2.9
CHEM-Imm	2.7

**Figure 26: Scaffold analysis score for PCKS-Imm scaffolds.** Integration of scaffold analysis data including ZO-1 assessment and cell seeding specificity into scores for overall category evaluation

### 4.6.4 Morphological evaluation of the seeded cells with SEM

The morphology of seeded RPTEC/TERT1 cells on PCKS-Imm scaffolds was investigated with SEM (Figure 27). The tubules displayed reduced diameters (Figure 27, blue arrows) and lost their characteristic honeycomb structure. Consequently, the TBM and interstitial spaces between the tubules appeared thicker in comparison to the scaffolds that had not undergone recellularization, (Figure 12). This finding further reinforces the observed macroscopic shrinking phenomenon (section 4.6.1). Notably, variations in cell density were observed across different locations on the scaffolds. Particularly, UBS60-Imm demonstrated lower cell occupancy compared to other methods. Moreover, unlike RPTEC cells of the native kidney, which are prominently found within the tubules, seeded RPTEC/TERT1 cells seemed to be primarily situated on the scaffold's surface which coincided with the presence of the thicker TBM and interstitium.

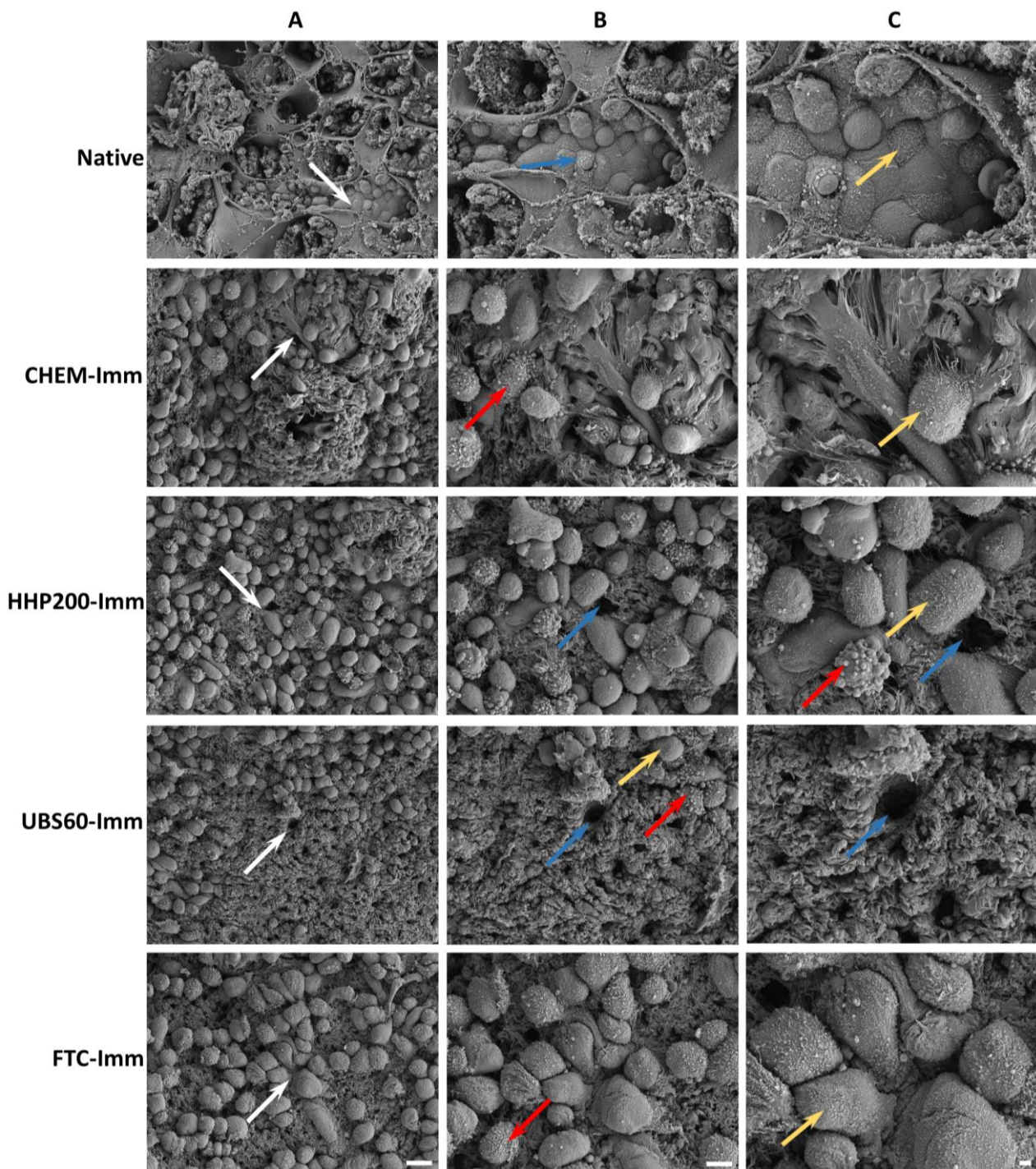


**Figure 27: Scanning electron microscopy of native and recellularized PCKS-Imm.** Representative images are divided into three columns. Magnifications: (A) 500x, (B) 1000x and (C) 2000x. White arrows represent the magnified areas shown in columns B and C. Formation of microvilli can be seen on both native and seeded cells (yellow arrows) while certain seeded cells reveal bubble-like structures on their surfaces (red arrows). Shrinking of the scaffolds is indicated by the smaller diameter of the tubules compared to the native kidney (blue arrows). Scale bars: (A) 20  $\mu\text{m}$ , (B) 10  $\mu\text{m}$ , (C) 5  $\mu\text{m}$ ,  $n = 2$

The native RPTEC cells exhibit a distinct cuboidal shape, characterized by their close intercellular packing. This is in contrast with the round to oval shape of the RPTEC/TERT1 cells on the recellularized PCKS-Imm. However, cells seeded on SYNTH glass scaffolds and on the cover glass in a 2D environment showed significant differences. Specifically, cells on SYNTH scaffolds displayed a more flattened shape compared to those on the PCKS-Imm scaffolds, likely due to the higher stiffness of SYNTH scaffolds (Figure S 10). Meanwhile, cells seeded in a 2D environment on cover glass demonstrated a fully extended and flattened body structure (Figure S 9), even more so than the cells on the SYNTH scaffolds. Furthermore, microvilli were found on the surfaces of RPTEC cells in the native kidney, which were also observed on all recellularized PCKS-Imm and SYNTH scaffolds (Figure 27, yellow arrows). However, it is notable that some seeded cells on all PCKS-Imm scaffolds exhibited bubble-like structures on their surfaces (Figure 27, red arrows), which appeared larger on CHEM-Imm and HHP-Imm scaffolds. In contrast, cells in the 2D environment did not exhibit a clear formation of microvilli. The structures indicated by the yellow arrows in Figure S 9 could potentially be microvilli, but they appear somewhat atypical since microvilli are thinner and more thread-like.

## 4.7 Characterization of recellularized PCKS-Prf

### 4.7.1 Analysis of the cell culture medium

The same methods were employed to assess the cell culture medium of recellularized PCKS-Prf as used for the immersion approach. The findings revealed that recellularized CHEM-Prf and FTC-Prf scaffolds supported human cell proliferation over time as demonstrated by the resazurin assay. However, their viability on day 7 was 46% and 38% lower, respectively, compared to their immersion counterparts (Figure 28A). Notably, CHEM-Prf exhibited the highest viability among the other perfusion methods, being 1.3 times higher on day 7 than FTC-Prf, demonstrating gradual cell growth over time, similar to the immersion approach. However, there were differences observed between the perfusion and immersion approaches. Notably, the viability of cells in recellularized FTC-Prf scaffolds did not show a gradual growth. It decreased on day 5 and increased again on day 7. Moreover, HHP200-Prf displayed the lowest cell viability in the perfusion approach and even 95% lower than its immersion (Figure 28A).

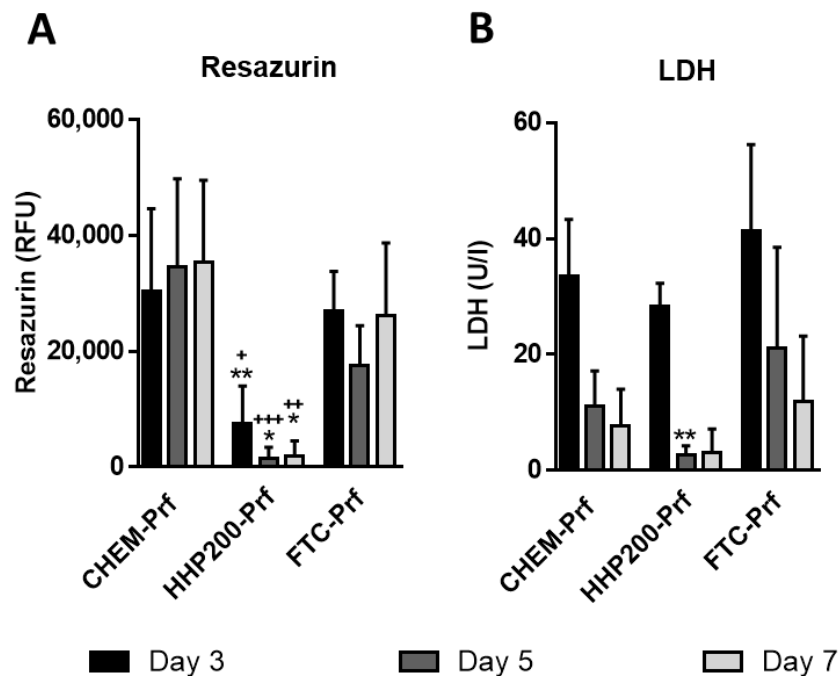


**Figure 28: Analysis of the cell culture medium of recellularized PCKS-Prf.** Assays were conducted on days 3, 5, and 7 of the incubation period. (A) Resazurin assay (B) LDH concentration. Groups were compared using the Kruskal-Wallis test, followed by a pairwise analysis with Dunn's test. Values are expressed as mean  $\pm$ SD ( $n = 6 - 10$ ). Significance levels are denoted by: (\* $p \leq 0.05$ ), (\*\* $p \leq 0.01$ ) and (\*\*\*) $p \leq 0.001$ ), represented by symbols as follows: +: CHEM vs. HHP200, \*: FTC vs. HHP200

Despite observing a decreasing trend of LDH concentration over time, FTC-Prf exhibited 1.5 times higher LDH concentration on day 3 compared to FTC-Imm, which later on day 7 decreased to be almost at the same level as FTC-imm (Figure 10B). This suggests that seeded cells in FTC-Prf may have encountered difficulties in adapting to the scaffold environment by the time of cell seeding. Furthermore, on days 5 and 7, FTC-Prf displayed higher cell death compared to CHEM-Prf, which corresponds to the results of the resazurin assay. Interestingly, HHP200-Prf scaffolds showed the lowest cell viability and consequently the lowest LDH concentration on both day 5 and day 7 among all methods, highlighting its unsuitability for facilitating a favorable environment for cell attachment and proliferation (Figure 10B).

Furthermore, on day 3, HHP200-Prf displayed the highest lactate concentrations, which were 2 times higher than CHEM-Prf and 1.5 times higher than FTC-Prf, indicating elevated stress levels. However, these levels decreased by the end of the incubation period, aligning with the findings of the resazurin and LDH assays.

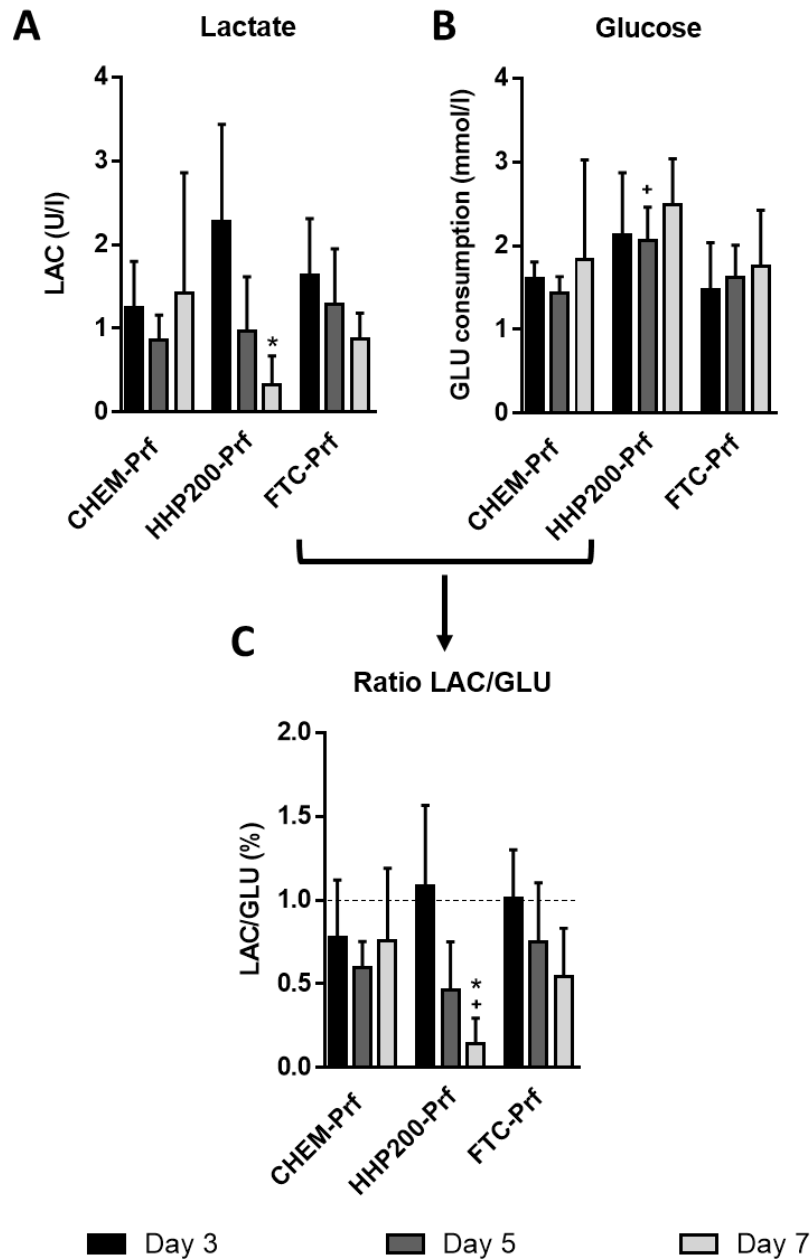


**Figure 29: Analysis of the cell culture medium of recellularized PCKS-Prf.** Assays were conducted on days 3, 5, and 7 of the incubation period. (A) Lactate concentration (B) Glucose consumption (C) Ratio of lactate to glucose (LAC/GLU) with an orientation line at 1.0. Groups were compared using the Kruskal-Wallis test, followed by a pairwise analysis with Dunn's test. Significance levels are denoted by: (\* $p \leq 0.05$ ), represented by symbols as follows: +: CHEM vs. HHP200, \*: FTC vs. HHP200


## 4 Results

---

Moreover, while lactate concentration in recellularized CHEM-Prf scaffolds showed a similar trend to its immersion counterpart, both FTC-Prf and HHP200-Prf exhibited a deviation from this trend, as their lactate concentrations decreased on days 5 and further decreased on day 7 (Figure 29C). Unexpectedly, HHP200-Prf scaffolds showed the highest glucose consumption (Figure 29C). This phenomenon could be linked to the limited number of viable cells, which, as response for high stress and in their struggle for survival, consumed more glucose. Considering the overall results, the lactate to glucose ratio remained below 1 for CHEM-Prf. In contrast, for FTC-Prf, the ratio was initially 1 on day 3, but decreased and remained below 1. Interestingly, the ratios for CHEM-Prf and FTC-Prf on day 7 were similar to their immersion counterparts (Figure 10E).

The results of the cell culture medium analysis were converted into scores. As shown in Figure 30, both HHP200-Prf and CHEM-Prf received similar scores (2.9), placing them at the top of this category, while FTC-Prf received the lowest score (2.7). Although HHP200-Prf received apparently the highest score, it was however excluded from further scaffold assessment.

Method	Score
HHP200-Prf	3.0
CHEM-Prf	2.8
FTC-Prf	2.5



**Figure 30: Medium analysis score for PCK-Prf scaffolds.** Integration of cell culture medium analysis data from day 7 of the incubation period into scores

### 4.7.2 Analysis of the scaffolds

#### 4.7.2.1 Investigation of migration depth of seeded cells within PCKS-Prf scaffolds

The migration depth of the seeded cells in PCKS-Prf scaffolds was investigated in the same manner as in the immersion approach. As seen in Figure 31, the total number of attached cells in all layers for seeded PCKS-Prf scaffolds is generally higher than their immersion counterparts but exhibited a different distribution pattern. While the number of cells remained largely similar in all layers in CHEM-Prf, it increased considerably in the second layer and dropped again in the third layer for FTC-Prf.

## 4 Results

This differs from the immersion approach, in which the number of cells decreased with each layer for both CHEM-Imm and FTC-Imm. This could be due to the lower thickness of PCKS-Prf (500  $\mu\text{m}$ ) scaffolds compared to PCKS-Imm (1000  $\mu\text{m}$ ) scaffolds, which possibly resulted in better diffusion conditions, thus allowing for better cell proliferation and migration.

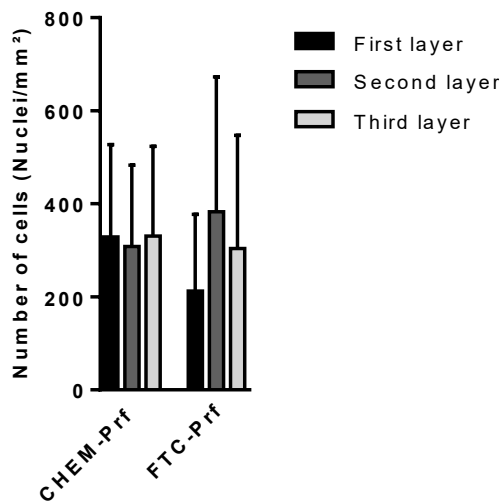


**Figure 31: Investigation of the migration depth of seeded cells within recellularized PCKS-Prf scaffolds** obtained from kidneys decellularized by perfusion. Values are expressed as mean  $\pm$ SD ( $n = 4$ ). Nuclei were stained with DAPI

### 4.7.2.2 Assessment of tight junction formation in recellularized PCKS-Prf

The investigation of ZO-1 production in recellularized PCKS-Prf was conducted in the same manner and parallel to PCKS-Imm. Similar to the immersion approach, ZO-1 localized around the cell nucleus, without forming distinct connections with neighboring cells (Figure 32A, B). Interestingly, CHEM-Prf showed approximately twice the levels of ZO-1 compared to CHEM-Imm, while FTC-Prf exhibited similar levels of ZO-1 as in FTC-Imm (Figure 32C). Specifically, recellularized FTC-Prf scaffolds displayed a 20% higher ZO-1 than CHEM-Prf and exhibited the highest production of ZO-1 in both decellularization approaches. This underscores FTC as the most effective physical treatment method within this study for creating a favorable environment for the cells. Despite containing a higher amount of residual DNA compared to their immersion counterparts, both CHEM-Prf and FTC-Prf scaffolds demonstrated equivalent or higher levels of ZO-1 expression. This could be due to the thinner structure of PCKS-Prf (500  $\mu\text{m}$ ), which may have provided better diffusion conditions for cell proliferation and migration.

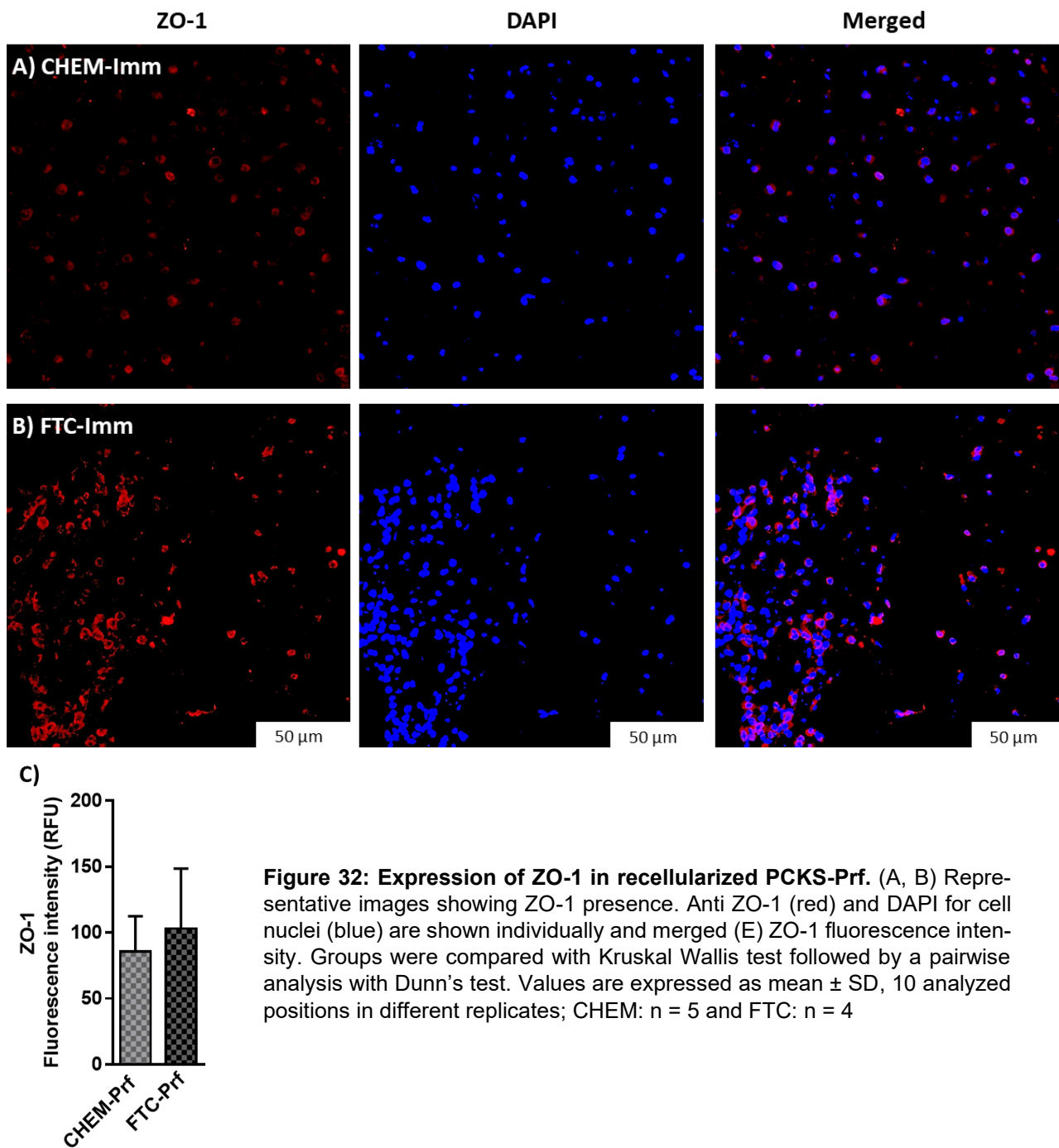


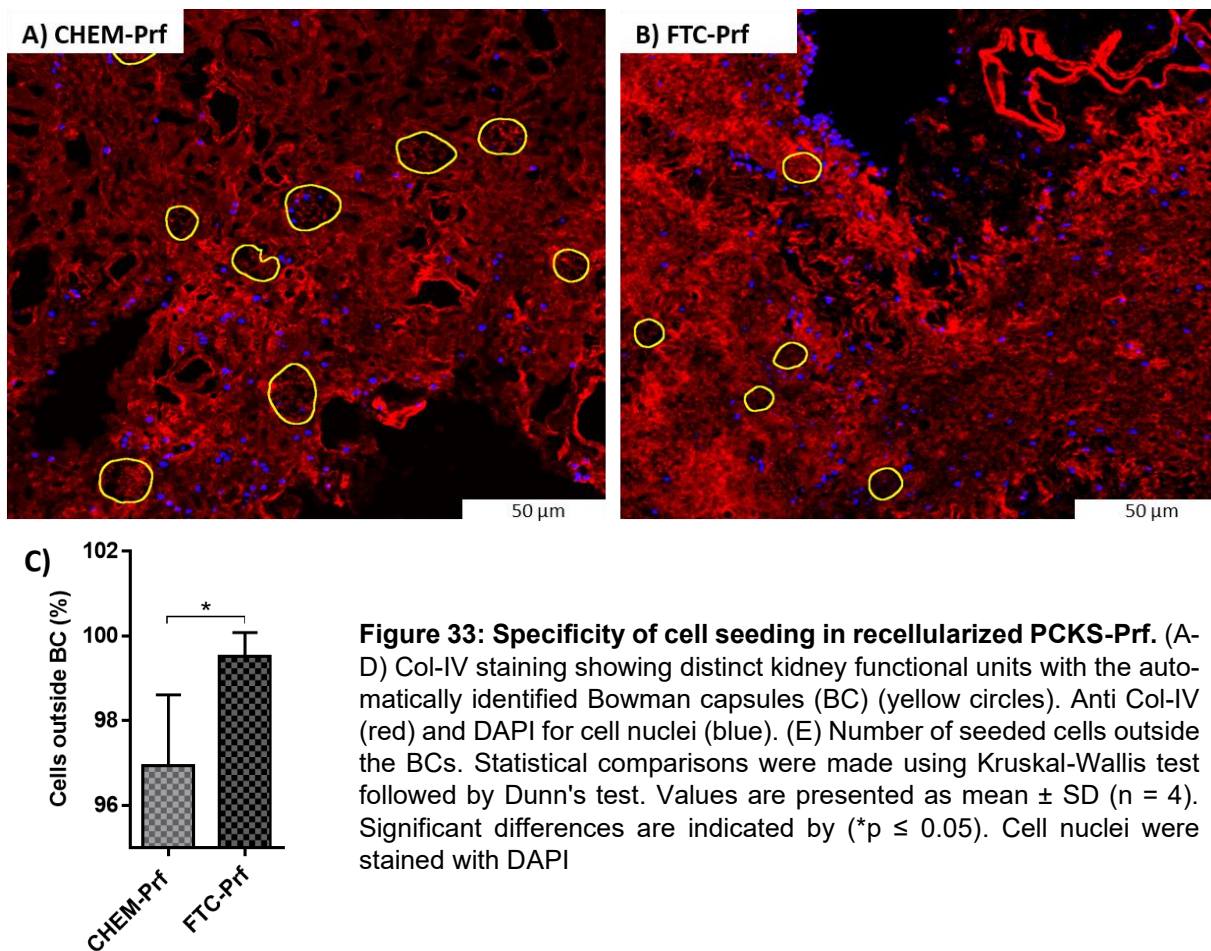
**Figure 32: Expression of ZO-1 in recellularized PCKS-Prf.** (A, B) Representative images showing ZO-1 presence. Anti ZO-1 (red) and DAPI for cell nuclei (blue) are shown individually and merged (E) ZO-1 fluorescence intensity. Groups were compared with Kruskal Wallis test followed by a pairwise analysis with Dunn's test. Values are expressed as mean  $\pm$  SD, 10 analyzed positions in different replicates; CHEM: n = 5 and FTC: n = 4

#### 4.7.2.3 Investigation of cell seeding specificity

The results revealed that FTC-Prf scaffolds demonstrated a statistically significant higher percentage (99.5%) of attached cells outside the BCs compared to CHEM-Prf (97%) (Figure 33). Furthermore, perfusion methods showed a slightly higher percentage of cells outside the BCs compared to the

## 4 Results

immersion method, but these differences are not statistically significant.



The findings from scaffold analysis, including ZO-1 assessment and the evaluation of cell seeding specificity in PCKS-Prf, were combined into the scoring system. FTC-Prf achieved the highest score (3.8). In contrast, CHEM-Prf obtained the lowest score (3.2) (Figure 34).

Method	Score
FTC-Prf	3.8
CHEM-Prf	3.2

Best  
 ↑ Scaffold analysis  
 Worst

**Figure 34: Scaffold analysis score for PCKS-Prf scaffolds.** Integration of scaffold analysis data including ZO-1 assessment and cell seeding specificity into scores for overall category evaluation.

### 4.7.3 Morphological evaluation of the seeded cells with SEM

The morphology of seeded RPTEC/TERT1 cells on PCKS-Prf scaffolds was investigated with the SEM (Figure 35).

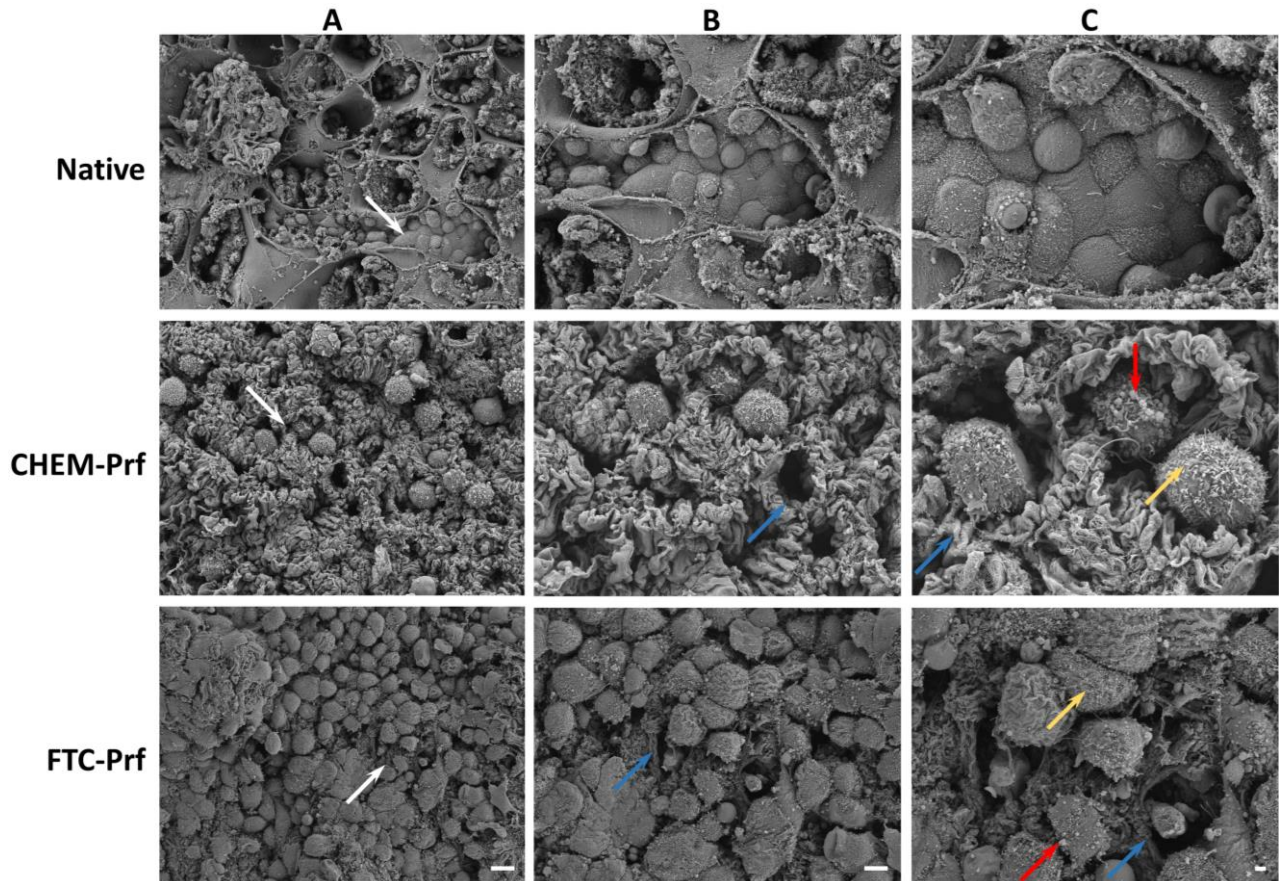


**Figure 35: Scanning electron microscopy of recellularized PCKS-Prf.** Representative images are divided into three columns at different magnifications: (A) 500x, (B) 1000x and (C) 2000x. White arrows represent the magnified areas shown in columns B and C. Seeded cells displayed the formation of microvilli (yellow arrows), and some of these cells exhibited bubble-like structures on their surfaces (red arrows). Noticeable reduction in scaffold size is apparent, as evidenced by the smaller diameter of the tubules compared to the native kidney (blue arrows). Scale bars: (A) 20  $\mu\text{m}$ , (B) 10  $\mu\text{m}$ , (C) 5  $\mu\text{m}$ ,  $n = 2$


Interestingly, similar findings to those of PCKS-Imm were observed in the perfusion approach. Notable variations in cell density were evident across different regions of the recellularized scaffolds. Moreover, seeded RPTEC/TERT1 cells appeared located on the scaffold's surface. However, in the case of CHEM-Prf, unlike its counterpart in the immersion approach, some seeded cells were observed within the tubules (Figure 35, red and yellow arrows). Additionally, a reduction in tubule diameters was also observed (Figure 35, blue arrows) when compared to non-recellularized scaffolds.

Moreover, seeded cells displayed a rounded to oval morphology on the recellularized scaffolds, similar to the immersion approach. Furthermore, while microvilli were also observed on the surfaces of seeded cells, bubble-like structures were evident on the surfaces of certain seeded cells across all scaffolds (Figure 35, red and yellow arrows).

#### 4.8 Recellularization score

Decellularization scores for immersion and perfusion approaches were separately presented, as they represent two different decellularization methodologies. However, recellularization scores were presented together (Figure 36), as PCKS-Imm and PCKS-Prf underwent the same recellularization protocol. As shown in Figure 36, FTC-Prf received the highest recellularization score (3.4) followed by FTC-Imm (3.2), emerging as top-performing methods in both approaches. It is important to note that HHP200-Prf recellularization scores represent only medium analysis findings, as scaffold analysis was not conducted for these scaffolds. Conversely, despite CHEM-Prf exhibiting higher residual DNA in decellularized scaffolds, its recellularization score exceeded that of CHEM-Imm, which registered the lowest score among all methods.

Method	Score
FTC-Prf	3.4
FTC-Imm	3.2
CHEM-Prf	3.0
HHP200-Prf	2.9
HHP200-Imm	2.8
UBS60-Imm	2.7
CHEM-Imm	2.6



**Figure 36: Recellularization score** combining the findings from medium and scaffold analysis

#### 4.9 Total score performance

The scoring system described in Table S 12 was employed for the generation of a total score for an overall ranking of all methods applied within this project. Notably, FTC-Prf and CHEM-Prf share the highest total score of 3.2. Despite their equal total scores, it is crucial to highlight that FTC-Prf scaffolds, with only 1000 ng DNA/mg tissue, outperform CHEM-Prf scaffolds, which contain 2700 ng DNA/mg, making FTC-Prf a more preferred option.

## 4 Results

The third-highest total score of 3.1 was attained by FTC-Imm (Figure 37). Interestingly, both FTC-Imm and FTC-Prf achieved the highest total scores within their respective approaches, underscoring the effectiveness of FTC as a physical treatment method followed by chemical decellularization. Noteworthy, UBS60-Imm and HHP200-Imm share an identical total score of 2.9, while HHP200-Prf follows with a total score of 2.8. On the other hand, CHEM-Imm received the lowest total score (2.7) in both approaches. Notably, the statistical analysis of the scores in all categories did not reveal any significant differences among the compared methods.

Method	Total score
FTC-Prf	3.2
CHEM-Prf	3.2
FTC-Imm	3.1
UBS60-Imm	2.9
HHP200-Imm	2.9
HHP200-Prf	2.8
CHEM-Imm	2.7

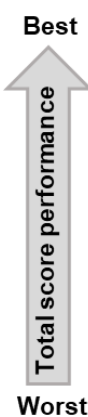


**Figure 37: Total score performance for all methods** determined by averaging the de- and recellularization scores

### 4.10 Optimization of perfusion decellularization after HHP treatment

As described earlier, HHP200-Prf achieved the second lowest total score. This outcome is discussed in detail in section 5.3.1, where it is suggested that HHP-induced tissue compression may have led to vascular network constrictions, hindering chemicals perfusion. Therefore, it was attempted to improve perfusion decellularization of HHP treated kidneys using the indirect decellularization approach described in section 3.4.2. The results of the direct decellularization showed that SDS1% led to only a 24% reduction in DNA content (Figure 38). Treatment with HHP100-SDS1% resulted in only a 6% reduction in DNA, indicating a highly ineffective decellularization. On the contrary, FTC-SDS1% achieved the highest DNA reduction (96%).

In the indirect decellularization, an additional step involving PBS perfusion after the physical treatment (HHP or FTC) and prior to perfusion with SDS0.5% was introduced as a preconditioning to encourage vasculature deconstriction. Interestingly, despite using only half the concentration, SDS0.5% achieved a similar reduction in DNA content compared to SDS1%. Interestingly, a significantly higher DNA reduction (64%) was achieved by HHP150-SDS0.5% in the indirect approach

## 4 Results

compared to the direct approach. Thus, highlighting, the success of the indirect decellularization approach in enhancing perfusion decellularization following HHP treatment.

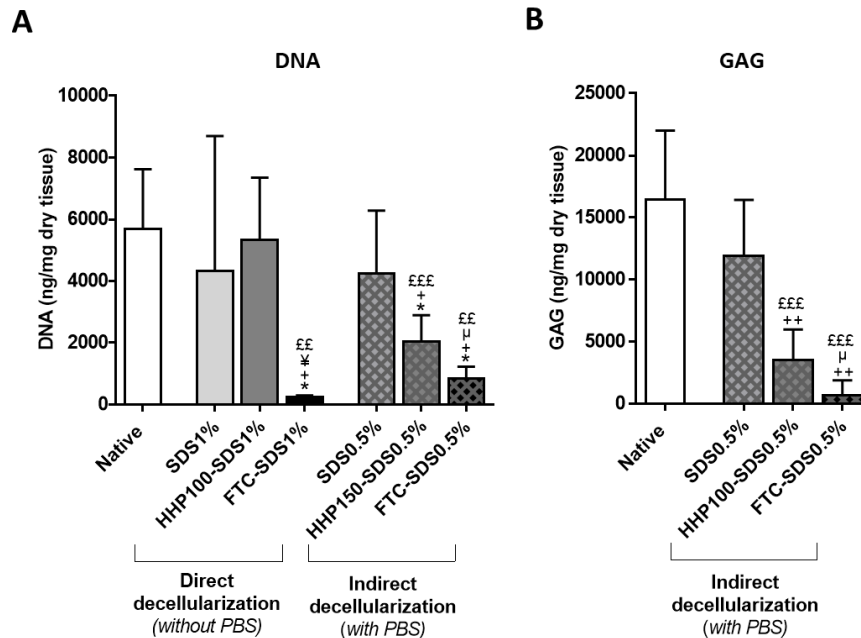


**Figure 38: Characterization of decellularized whole kidneys (direct and indirect approaches).** (A) DNA quantification (B) GAG Quantification. Data were analyzed with Mann-Whitney U test ( $n \geq 4-6$ ). Values are expressed as mean  $\pm$  SD. Significance levels are denoted by: (\* $p \leq 0.05$ ), (\*\* $p \leq 0.01$ ), and (\*\*\*) $p \leq 0.001$ ) represented by symbols as follows: €€ for native, ¥ for SDS1%, \* for HH100-SDS1%, and  $\mu$  for HHP150-SDS0.5%.  $n = 5$

However, when FTC was followed by the same protocol, it resulted in a significant DNA reduction of 85%, which was lower than that in the direct approach. Regarding GAGs, the results of the indirect decellularization approach revealed that both physical treatments, HHP150 and FTC led to a statistically significant reduction of 78% and 95%, respectively.

Histological analysis showed that FTC-SDS1% and FTC-SDS0.5% have the lowest accumulation of nuclear and cytoplasmic materials. In contrast, all other methods showed much higher accumulation of nuclear material (Figure 39), aligning with the results of DNA quantification. Both approaches indicated gross preservation, with no signs of complete breakdown in the ECM structure (Figure 39). However, structural assessment within the scoring system revealed relatively higher damage compared to PCKS-Imm and PCKS-Prf. Specifically, only three out of ten methods (CHEM-Imm and FTC-Imm) received a structure score below 3.0 (Figure S 1 and Figure S 2). In contrast, five out of

## 4 Results

six methods within the direct and indirect decellularization approaches received a structure score below 3.0 (Figure S 6).

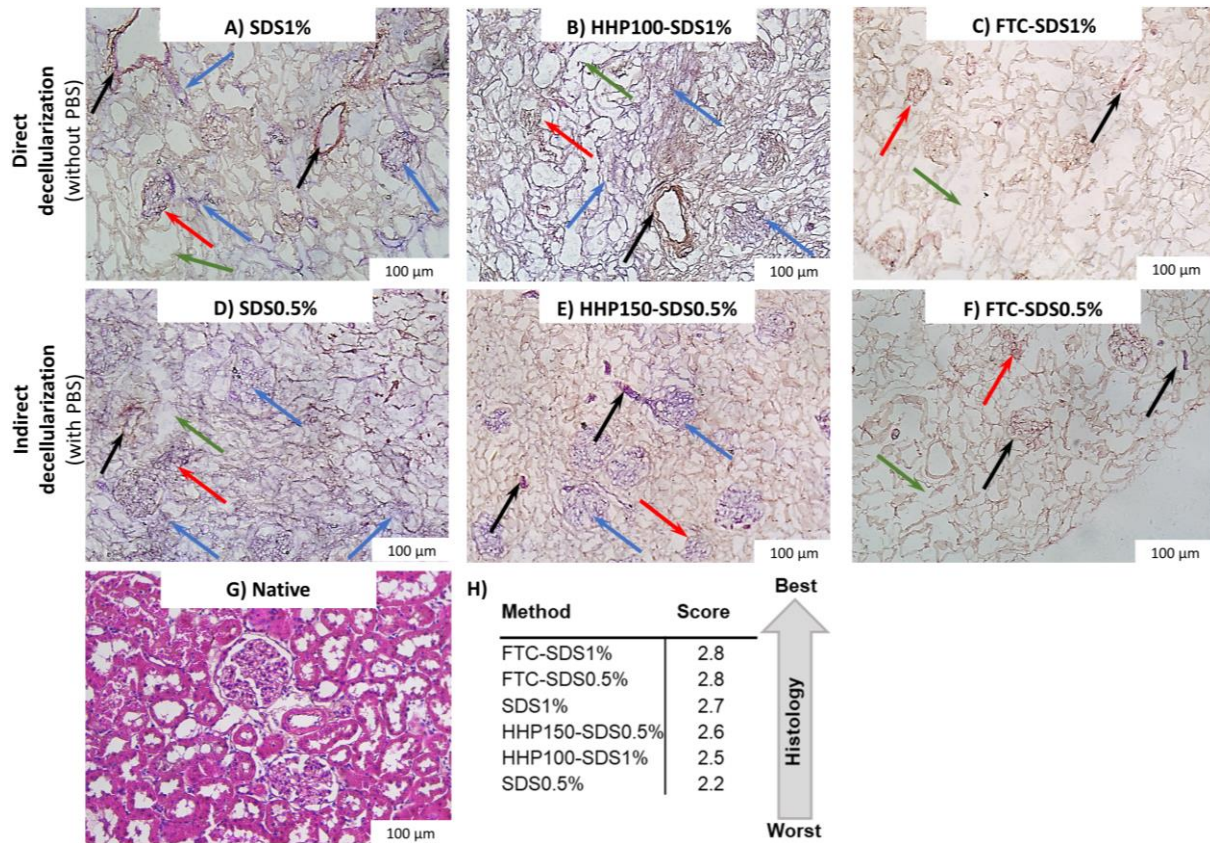


**Figure 39: Analysis of H&E stained decellularized whole kidneys (direct & indirect approaches).** Kidneys decellularized by (A) SDS1% (B) HHP100-SDS1% (C) FTC-SDS1% (D) SDS0.5% (E) HHP150-SDS0.5% (F) FTC-SDS0.5% and (G) Native kidney (H) Histology scores. Arrows point at remaining nuclear (hematoxylin, blue arrow) and cytoplasmic material (eosin, black arrow). Scale bar: 100 μm

For example, the morphology of some glomeruli in all methods appeared relatively contracted and displayed slight alterations (Figure 39, red arrows). Additionally, in certain cases, tubules exhibited signs of structural distortion and fragmentation (Figure 39, green arrows). The highest histology score was achieved by FTC-SDS1% and FTC-SDS0.5% (2.8). However, although HHP150-SDS0.5% achieved a significant reduction of DNA when compared to HHP100-SDS1%, both achieved similar histology scores of 2.6 and 2.5 respectively.

### 4.11 Reactivity of PBMCs to native and decellularized kidneys

A preliminary exploration into the immunogenicity of decellularized kidney scaffolds was conducted. PBMCs were incubated for 48 h with 0.5 mg of both native and decellularized kidney homogenates. Additionally, PBMCs were exposed to IL-2 and 6% ethanol. Incubation of PBMCs with native kidney homogenates led to a 62% increase in resazurin fluorescence compared to untreated PBMCs (Figure 40A). Conversely, incubation with decellularized kidney homogenates resulted in a similar decrease as observed with 6% ethanol, with an approximately 50% reduction in viability. In contrast, incubation with IL-2 caused an 18% increase in resazurin fluorescence. Additionally, incubation of PBMCs with native kidney homogenates, as opposed to decellularized homogenates, triggered higher LDH levels, with a pronounced difference of 69% (Figure 40B). PBMCs incubated with decellularized kidney homogenates exhibited a behavior similar to those exposed to IL-2. Conversely, incubation with native kidney homogenates had a more pronounced cell-damaging effect, resulting in 25% higher LDH levels compared to cultivation with 6% ethanol. Furthermore, decellularized kidney homogenates showed a 40% lower LDH level compared to untreated cells.

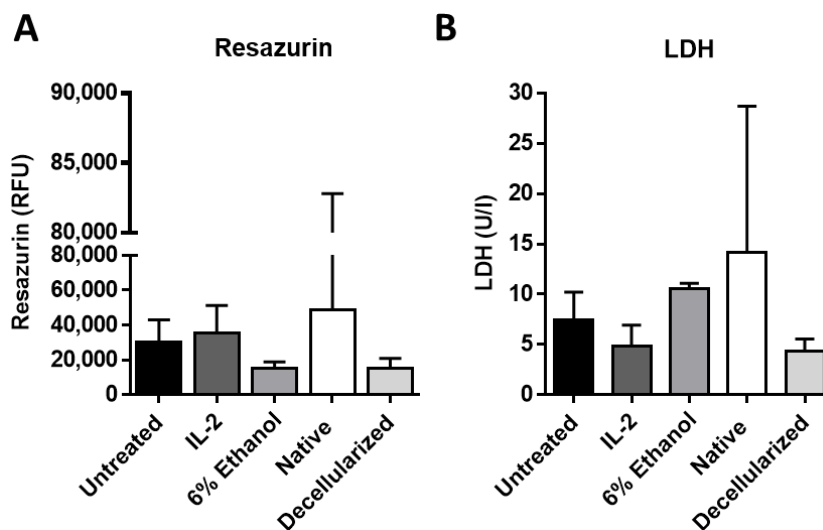


**Figure 40: Incubation of PBMCs with homogenized native and decellularized kidney scaffolds.** (A) Resazurin assay (B) LDH concentration. Values are expressed as mean  $\pm$  SD. Incubation time: 48 h. Untreated ( $n \geq 9$ ), IL-2 ( $n = 4$ ), 6% Ethanol ( $n = 3$ ), native kidney ( $n = 6$ ), decellularized ( $n = 4$ )

## 5 Discussion

### 5.1 Unveiling the effects of HHP and FTC on kidney tissues

Kidney slices subjected to HHP treatment at pressures of 400 and 600 MPa exhibited a noticeable color change, coinciding with a less efficient decellularization process. Similar alterations in color are observed in the food industry when HHP is used for meat decontamination [125]. These color changes following HHP treatment can be attributed to several factors. HHP has the potential to induce modifications in hemoglobin, potentially disrupting their optical properties and causing a shift in color [126,127]. Additionally, the application of pressure may trigger chemical reactions within the tissues, including lipid and protein oxidation, which could further contribute to the observed color alterations [125,126]. Moreover, HHP induces variable changes in protein conformational structures depending on the applied pressure level [125]. Consequently, it can be speculated that such alterations may have played a role in reducing the effectiveness of decellularization.

Given that collagen is the most abundant protein in the ECM, it was imperative to examine how the integrity of collagen was affected by different chemical and physical treatment methods [50]. CHP is a synthetic peptide labeled with fluorescein, which binds to denatured collagen structures. It has a strong propensity for collagen's triple-helix folding and can hybridize with denatured collagen chains, re-forming the triple-helical structure, similar to the binding of a primer to melted DNA strands in PCR [128]. The results of this study revealed that chemical treatments induced more substantial denaturation than that caused by the physical treatments. Specifically, 1% SDS caused extensive denaturation even surpassing that resulting from heating tendons to 60 °C. In a comparable investigation, porcine ligaments were exposed to various chemicals, including 1% SDS and 3% Triton X-100 overnight. Interestingly, SDS induced a six fold greater collagen denaturation compared to Triton X-100, despite Triton's threefold higher concentration [128]. Furthermore, a study involved the decellularization of jellyfish tissues using 1% SDS, 5% Triton X-100, and 5% SDC for five days. While SDS induced an 18-fold higher denaturation than Triton X-100, SDC caused no detectable denaturation [129]. Conversely, in the context of this project, the treatment of kidney tissues with HHP at 600 MPa did not induce any denaturation. This outcome aligns with other studies that have suggested denaturation only occurs at pressures exceeding 1000 MPa while lower pressures result only in structural alterations to the protein [76,130,131], which cannot be measured using CHP. Interestingly, despite exposing kidney tissues to four FTCs, collagen denaturation was minimal.

Moreover, Salti et al. investigated the effect of the intensity of the physical treatment on PCKS histologically right after the treatment and without further decellularization with CHEM-Imm [132]. The analysis showed an HHP-induced compression resulting in a reduction in non-cellular spaces (NCS), which increased with the applied pressure. It can be speculated that HHP-induced compression reduces the diffusion of the chemical reagents into the inner areas of the PCKS during decellularization. However, no correlation was found between the reduction in NCS and DNA content, which decreased with increasing the pressure (Figure 10A). In contrast, FTC treated PCKS achieved the highest reduction in DNA content in spite of the huge reduction in NCS [132].

## 5.2 Immersion decellularization

### 5.2.1 FTC-Imm: optimal DNA reduction and GAGs preservation

All applied methods significantly reduced GAG content, while on the other hand collagen content was largely preserved (Figure 10B, C). The CHEM-Imm protocol led to the most significant reduction in GAG content and received the lowest histology score [132]. Research conducted by other scholars stated that kidney decellularization by SDS (1%), SDC (1%) [91], or trypsin (0.05 %) [109] resulted in a substantial reduction in GAGs, whereas SDC reduced GAG content more significantly than SDS [91]. Therefore, the significant reduction in GAG content in this study can be attributed to the combination of both SDS and SDC in the CHEM-Imm protocol. Moreover, SDS accumulates heavily in the ECM and is difficult to wash out [19,133]. On the other hand, Triton X-100 was reported in several studies to better preserve the components of the ECM [91,93,124,134].

As shown by Salti et al., all HHP protocols within this project achieved the best preservation of GAGs but were the least effective in the reduction of DNA [132]. In previous studies, HHP (1000 MPa) was used for the treatment of porcine corneas and menisci with subsequent washing with DNase. In both cases, DNA was reduced significantly and GAGs were largely preserved [79,81]. Moreover, Sasaki et al. compared the chemical decellularization of corneas with the combined approach of HHP (1000 MPa) and DNase. It was shown that the combined approach resulted in a significant reduction in DNA content and in a better preservation of GAGs when compared to a decellularization by SDS or Triton X-100 alone [79,135]. Knowing that pressure levels up to 200 - 300 MPa usually cause only a reversible protein denaturation [136] could possibly explain the ineffective removal of DNA in HHP-Imm protocols applied within this study. However, treating kidney tissues with pressures up to 980 MPa would probably lead to a much higher compression and concomitant reduction of NCS as

demonstrated in this study at lower pressure levels (Figure 8). Interestingly, Zemmyo et al. suggested combining supercooling and cyclic application of HHP, which was investigated only in collagen gels and suspensions of fibroblasts. The method included supercooling at -4 °C or -8 °C followed by HHP at a maximum of 250 MPa, which was maintained for 2 min and decreased to 100 MPa and then increased again to the same pressure (5 cycles). While the viability of the cultured fibroblasts decreased significantly, the integrity of the collagen gel was preserved. This protocol represents an interesting approach, although it was not yet applied on any types of organs or tissues [137].

On the other hand, GAGs and collagen contents in FTC-Imm scaffolds were similar to CHEM-Imm but with the additional benefit of a substantial reduction in residual DNA content [132]. Repeated FTC contributed to cellular removal through the formation of ice crystals in the cells and the destruction of cell membranes [138]. It can only be speculated that FTC resulted in loosening the cell-cell and cell-matrix contacts causing a more effective removal of DNA. Several groups reported a similar effect in tissues treated with FTC such as kidney, parathyroid capsule, small intestinal submucosa and pericardium [94,139–141]. Poornejad et al. treated porcine kidneys with FTC and decellularized the kidneys by perfusion with a combination of hypertonic and hypotonic solutions as well as SDS (0.5%). It was reported that FTC can damage the cellular material while minimally damaging ECM protein structures [94,95]. In another study, rat kidneys were treated with FTC and perfused with Triton X-100 and SDS. While DNA content was reduced to 40 ng/mg, cytokines and major ECM components were largely preserved [96]. Moreover, Watanabe et al. applied FTC and HHP as physical treatment methods for the decellularization of porcine menisci. It was shown that HHP resulted in a higher reduction in DNA and a lower preservation of the mechanical properties than FTC. However, the results of Watanabe et al. can hardly be compared with the results within this project due to substantial differences in the protocols. While HHP treatment of the menisci was followed with a decellularization with DNase, no such DNase treatment step was done after the FTC treatment of the menisci [81].

UBS methods within this project resulted in a significant reduction in DNA but also caused the highest reduction in GAGs content (Figure 10A, B) [132]. This is in line with the results of a study by Yusof et al. who compared the decellularization of menisci by immersion in chemicals in a sonication bath and reported a significant reduction of GAGs content [142]. Moreover, two separate studies reported the perfusion decellularization of whole porcine kidneys with SDS and evaluated the effect of coupling perfusion decellularization with sonication at different power levels (60 - 250 W). Both studies

demonstrated a significant decrease in perfusion time while causing minimal to moderate disruptions of the ECM microarchitecture [97,143]. This partially contradicts with the SEM results in this project, which showed a marked deterioration of the ultrastructure at 30 and 60 W. This could be attributed to the lower thickness of PCKS-Imm that potentially makes them more vulnerable to sonication-induced mechanical impacts.

### **5.2.2 Insights into DNA reduction and ECM Quality**

Decellularization of PCKS-Imm represents a promising approach, although it will not be used for transplantation experiments. It serves as a model to facilitate the understanding of the aforementioned physical methods and their effects on the ECM. Achieving a maximum DNA content of 50 ng/mg dry ECM is a crucial criterion for assessing decellularization [65]. However, the protocols were not initially optimized towards the lowest achievable DNA concentration. Several parameter variations were initially tested for each of the methods (HHP: 50-200 MPa, UBS: 30 and 60 W, FTC: 1-6 cycles), which permitted a good comparison of the relative impacts on several decellularization factors and not only on the scaffold's DNA content.

The composition and structure of the ECM are often difficult to compare, because they include both quantitative (e.g. GAG, DNA, collagen) and qualitative (histology) data. Therefore, a scoring system was used to include these data in a decellularization score. Although both UBS30-Imm and FTC-Imm achieved the same decellularization score (3.1), SEM analysis indicated a higher degree damage to the ultrastructure in UBS30-Imm scaffolds. Collectively, the results suggest that FTC-Imm is most effective in reducing DNA while best preserving GAG and the ECM structure, implying that it could be suitable as a combination treatment when trying to reduce the duration of incubation in chemical reagents. Therefore, the insights gained from decellularizing PCKS-Imm are invaluable for the application and optimization of perfusion decellularization on whole rat kidneys.

The importance of growth factors (GF) as a characteristic parameter for the preservation of decellularized kidneys is acknowledged. However, the small size of rat kidneys and the low amount of decellularized PCKS-Imm scaffolds does not provide sufficient material for the analysis of GFs using commonly available assay kits. While using 1 mg of dry homogenate was sufficient for each of the other assays (DNA, collagen and GAG), even 5 mg were clearly below the detection limit of the GF assay. Therefore, despite the relevance of this parameter, a quantification of GFs was not feasible in this project. Other research groups reported using different quantities of the dry homogenate for

the GF assay. While a study involving porcine kidneys used 230 mg [91], around a whole or a half rat kidney were used in other studies [96,144].

### **5.3 Perfusion decellularization**

Decellularization through immersion and perfusion represents completely different methodologies. PCKS-Imm served as a model to explore various parameters. Building on the insights obtained from immersion decellularization and the scoring system results, specific methods were chosen for further investigation through perfusion decellularization of whole rat kidneys. Consequently, the outcomes of each decellularization approach are presented independently.

Preparation of PCKS from whole kidneys decellularized by perfusion (PCKS-Prf) was necessary for subsequent recellularization. As cells are removed during whole kidney decellularization, their structure gradually collapses, making them soft, flexible, and unstable. This makes it difficult to cut the kidneys into PCKS using a vibratome. Therefore, a method was developed to stabilize the structure of the decellularized kidneys. Perfusing the kidneys with warm Tissue Tek and then immersing them in ice-cold PBS stabilized the kidneys, turning them into a gel-like structure, enabling to cut 500 µm thick slices using the vibratome.

#### **5.3.1 Comparing HHP-Prf and FTC-Prf**

Although FTC was used as a physical treatment for perfusion decellularization of whole kidneys [94–96], there is currently no evidence in the literature to support the use of HHP for this purpose. As discussed earlier in section 5.2.1, these research groups applied a pressure of 1000 MPa to induce an irreversible protein denaturation in tissue resulting in an effective removal of DNA while preserving the ECM components. However, applying a pressure of 200 MPa (HHP200) to whole kidneys in this study, resulted in the least effective decellularization in the perfusion approach and even less effective than in the immersion approach. This may be due to several factors. The compression of kidney tissues induced by HHP and indicated by the reduction in NCS, likely caused constrictions in the vasculature, impeding the flow of chemicals. Additionally, cells broken up by HHP, combined with subsequent cell lysis by Trypsin, may have led to increasing the pressure in the already constricted vascular network resulting in potential damage to fine blood vessels.

Despite the initial lower flow rate (0.5 ml/min), the higher pressure across the vasculature may have caused a less effective decellularization. On the other hand, while FTC-induced compression caused

a greater reduction in NCS, FTC-Prf was found to be the most effective in terms of DNA removal, indicating that the vascular network was not compromised. Freezing creates ice crystals leading to mechanical damage to the cell membrane, while during thawing, water moves out of the cells through the ruptured membrane, reducing the overall volume of the tissue [138]. In contrast, HHP treatment at pressures up to 200 MPa induces apoptotic cell death, which causes the loss of cell volume or cell shrinkage [76,145]. Therefore, it is suspected that also HHP200-Prf led to water loss and a reduction in total tissue volume. However, despite the less severe effect of HHP-induced compression, as indicated by the lower reduction in NCS, HHP200-Prf resulted in the highest amount of residual DNA. This suggests that tissue compression caused by HHP200-Prf is not the sole factor hindering the decellularization. Although protein denaturation only occurs at pressures of 1000 MPa and above, the use of lower pressures can still induce changes in protein structure, leading to misfolding, aggregation, and the formation of protein gels [76,130,131]. Therefore, it can be speculated that structural changes induced by HHP at 200 MPa in proteins caused them to become more resistant to chemical reagents, resulting in a much lower reduction in DNA content. However, it is important to note that HHP does not damage GAGs [76], which probably explains why HHP200-Prf resulted in a similar amount of GAGs as in CHEM-Prf.

### **5.3.2 FTC-Prf: highest DNA reduction but lowest GAG preservation**

This study found that using FTC-Prf for decellularization resulted in effective DNA removal but also the highest loss of GAGs. Hu et al. applied four cycles of FTC on rat kidneys with subsequent perfusion with Triton X-100 and SDS, which significantly reduced DNA below the threshold of 50 ng/mg while preserving ECM components [96]. Similarly, Poornejad et al. used FTC on porcine kidneys with a combination of hypertonic and hypotonic solutions and SDS, resulting in significant removal of DNA and good retention of ECM components [94].

However, neither study included a control protocol without FTC, making it difficult to determine if the positive outcomes were solely due to FTC. Other research groups utilized FTC as a physical pre-treatment for perfusion decellularization of organs such as the pancreas, heart, lungs, and liver [146–150]. Furthermore, this study revealed that collagen content was generally maintained in FTC-Prf and slightly decreased in HHP200-Prf, while CHEM-Prf exhibited a higher content than the native kidney. However, this finding does not indicate an enrichment of collagen in decellularized CHEM-Prf scaffolds. As collagen is the most abundant component in the ECM [45], it remains largely available after decellularization. As a result, the remaining collagen constitutes a larger proportion of the

total dry weight, while the cellular proteins that are not part of the ECM are removed. Therefore, the amount of collagen tends to increase as a percentage of dry weight after decellularization [151]. Several studies for the decellularization of different organs such as kidney, liver, bladder, pancreas and blood vessels reported the same effect [91,144,151–154].

### **5.3.3 Perfusate analysis: SDS reduced GAGs content significantly**

The evaluation of decellularization is done mainly through destructive endpoint analysis, which render the scaffold unusable for recellularization [155]. Perfusate analysis is a non-destructive approach to monitor perfusion decellularization. It entails assessing the composition of the decellularization reagents circulated through the vascular network. The perfusate is often collected and analyzed by the end of the decellularization using the same biochemical assays as those used for endpoint scaffold analysis [155,156].

As decellularized scaffolds by all perfusion protocols within this project demonstrated a significant reduction in GAGs, it was necessary to determine which chemical reagent contributed to this loss. Based on the results, it is recommended to optimize the FTC-Prf protocol to increase the retention of GAGs, as it demonstrated the highest removal of DNA. Above the critical micelle concentration of 0.2% w/v, SDS forms micelles resulting in a greater damage and higher accumulation in the ECM. Thus, leading to decreased cell survival upon recellularization [89,157,158]. Even though only 0.1% SDS was used in this study, it contributed to the highest loss of GAGs for all perfusion methods. This is consistent with previous studies that have demonstrated that SDS is highly aggressive in terms of GAGs removal [91,159]. Moreover, Bongolan et al. investigated several concentrations of SDS (1%, 0.1%, 0.075%, 0.05%) for the decellularization of human kidney sections. Interestingly, they found that although all concentrations removed similar amounts of DNA, the retention of GAGs increased as the SDS concentration decreased [89].

On the other hand, perfusion with SDC resulted within this project in the removal of the highest amount of collagen. This finding aligns with a study which compared the effects of SDS and SDC on the decellularization of kidney sections and reported the same effect of SDC on collagen as in this study [91]. Consequently, since the contribution of SDS and SDC to DNA removal was smaller than that of other reagents, it is recommended to reduce their concentrations in FTC-Prf protocol. However, this post-process analysis of the perfusate is time-intensive, posing a challenge in customizing decellularization protocols for individual organ characteristics.

To address this issue, Hülsmann et al. monitored rat heart decellularization by measuring the perfusate's rheological properties and found correlations between protein and DNA content as well as perfusate viscosity [160]. In another study the turbidity of the perfusate was quantified, which is directly proportional to the removal of cells and DNA content [161,162]. Alternatively, Raman spectroscopy can be used for perfusate analysis as it can detect multiple biomarkers simultaneously, providing a comprehensive evaluation of the scaffold's quality [163,164].

### 5.3.4 Understanding perfusate volume dynamics

This study found that despite a consistent pump flow rate of 1 ml/min following Trypsin, the actual perfused volume in all methods exceeded the theoretical volume. This can be attributed to the arterial pressure and initial resistance of the vascular network to the perfused chemicals, which are known to be high at the beginning of the decellularization and decrease gradually as cellular content is removed [19]. Therefore, as the pressure decreases during decellularization, a higher volume of chemicals is pumped at the same applied flow rate of 1 ml/min. Nevertheless, applying a constant flow rate may increase the risk of damaging the BM of the vasculature due to persistent mechanical stress [19]. However, HHP-Prf and FTC-Prf showed a lower actual volume of 108% than CHEM-Prf (118%). This could be attributed to flow blockage caused by tissue compression and the high accumulation of damaged cellular material resulting from physical treatment. In a comparable study, Palma et al. measured the change in pressure across the vasculature during lungs decellularization. The protocol started by perfusing PBS followed by SDS and demonstrated a tremendous increase in arterial pressure during SDS perfusion, which decreased over time as cellular content was removed [165].

Previous studies on rat kidney decellularization applied flow rates between 0.4 - 10 ml/min [85,96,124,144,166,167]. However, high flow rates after a physical pretreatment could cause a much greater damage to the vasculature. To enable the vasculature to gradually adapt to changes in vascular resistance, perfusion under a constant physiological pressure is preferred, in which the flow rate is allowed to fluctuate to compensate for pressure changes across the vasculature [19]. This approach helps in accommodating the inherent differences in kidney size and vascular resistance due to different age and weight of the rats as reported by Bell et al. [168]. Girard et al. conducted a study to compare constant flow and constant pressure decellularization of the lungs. The results demonstrated that the constant pressure approach was more effective in removing cellular materials and preserving ECM components. It also resulted in higher cell viability upon recellularization [169].

Several research groups decellularized rat kidneys under constant physiological pressure conditions (100 mm Hg) [94,119,158,170]. However, no studies were found on comparing both approaches for kidney decellularization.

### **5.3.5 Perfusion decellularization: insights into protocol optimization**

Perfusate analysis conducted in this study proved to be effective in identifying areas of optimization. Specifically, it highlights the need to minimize the concentrations or durations of SDC and SDS to improve the process. According to the results obtained in this project and as discussed in section 5.2.1, Triton X-100 is a less aggressive detergent and can therefore be used to further reduce the residual DNA in FTC-Prf scaffolds. However, even though FTC-Imm and FTC-Prf did not reduce DNA content to below 50 ng/mg, they did achieve the highest reduction, which suggests their potential for further optimization. Additionally, a recent study by Yang et al. reported that performing FTC at -20 °C in combination with cryoprotectants before decellularization was better in preserving the ECM [171]. Hence, future studies should consider incorporating cryoprotectants before FTC and performing FTC at -20 °C instead of -80 °C. Moreover, it is advisable to switch to a constant pressure perfusion decellularization, as this can better preserve the ECM. Alternatively, if a constant flow is preferred, lower or graduated flow rates can be used to minimize damage to the native vasculature and ECM [19]. However, it is recommended to monitor the arterial pressure during decellularization, ensuring that it remains below the physiological level of 100 mm Hg.

The preservation of the vascular network is crucial for effective kidney recellularization [68]. To assess the integrity of the vasculature, vascular corrosion casting can be used, where a red or blue polymer is perfused through the artery or vein, enabling the visualization of damage to the vasculature [84,86,124,144]. Other methods include micro-computerized tomography, contrast radiography, X-ray angiography, and fluoroscopic angiography [88,159,172,173].

Moreover, fluorescence microbeads can be perfused into the artery, which are then collected from the vein and ureter. A higher infiltration of beads into the parenchyma suggests damage to the ECM and vascular BMs. Thus enabling a quantitative evaluation of the vasculature [68].

## **5.4 Recellularization of PCKS**

Decellularization must achieve a challenging balance between removing DNA and other cellular components while preserving the ECM structure. Although investigating DNA removal as well as the

composition and structure of the ECM is vital for understanding the decellularization process, these considerations are incomplete without studying its suitability for recellularization. The decellularization score, combined with insights from SEM analysis, guided the selection of the scaffolds for recellularization. Specifically, FTC-Imm, UBS60-Imm, CHEM-Imm scaffolds from the immersion approach, and CHEM-Prf, FTC-Prf, and HHP200-Prf scaffolds from the perfusion approach were chosen for recellularization.

### **5.4.1 Shrinkage of recellularized PCKS**

All scaffolds subjected to the recellularization protocol exhibited a noticeable shrinkage as the first observable phenomenon during the seven incubation days. Once the cells attach to the scaffold, they sense and respond not only to chemical signals but also to physical cues from the environment, such as substrate stiffness, topology, porosity, and elastic behavior [174,175]. As described in section 1.2.2.1, actomyosin generate traction forces, leading to cell migration. Researchers visualized traction forces exerted by different types of migrating cells (e.g. keratinocytes, fibroblasts) plated on a deformable silicone film by observing the resulting visible wrinkles on the film under the cell body [176,177]. Therefore, scaffold's stiffness plays a significant role in deformation, as evidenced by the SYNTH scaffolds, which are made of glass microfibers. However, cells seeded on SYNTH scaffolds exhibited a flatter and more spread-out morphology as confirmed by SEM analysis. In contrast, seeded cells on decellularized PCKS had a more rounded morphology due to their lower stiffness. Several studies investigated the effect of increasing substrate stiffness on cell morphology and reported similar results [178–180].

### 5.4.2 Cell culture medium analysis: metabolic insights

The viability of seeded cells and cell death were assessed using the resazurin and LDH assays respectively. Resazurin has been used widely to evaluate cell proliferation in seeded decellularized scaffolds including lungs, bones, trachea and pancreas, [181–184] as well as in seeded synthetic scaffolds such as polycaprolactone or hydrogel scaffolds [185,186]. Additionally, glucose consumption and lactate release were also quantified.

The findings within this project showed that irrespective of the decellularization method used, the scaffolds offered a favorable environment for cell adhesion and allowed seeded cells to proliferate throughout the seven days incubation period. This was accompanied by a decrease in LDH concentration on day 7 compared to day 3, indicating minimal cell death and that seeded cells were adapting to the scaffold. This also suggests that the washing of the scaffolds with PBS after decellularization was effective in removing toxic chemical reagents. In a comparative study, seeded cells on decellularized porcine kidney slices, exhibited a gradual increase in resazurin fluorescence indicating cell growth over time [109]. Additionally, the resazurin assay was used to assess the viability of cells in whole organs that were de- and recellularized by perfusion. Following perfusion recellularization, arterial perfusion of resazurin was carried out in whole liver and kidney scaffolds demonstrating cell growth over time [187].

Multiple studies have reported an elevation in lactate production in RPTEC/TERT1 cells upon exposure to various compounds. Notably, a decrease in cell viability was always preceded by an increase in lactate production, unless the compound inducing cell stress was removed [106,188–190]. Limonciel et al. demonstrated the applicability of using lactate as a non-invasive and simple marker for detecting cell stress in various cell lines, including RPTEC/TERT1 [106]. In this study, all seeded scaffolds exhibited high lactate production on day 3, indicating initial cell stress during cell attachment. The decline in lactate levels on day 5, coupled with a simultaneous increase in glucose consumption, indicated a likely cellular adaptation to the 3D environment, with cells possibly optimizing their metabolic pathways for improved energy production. As the cells further migrated through the scaffold they may have been stressed by insufficient oxygen and nutrients thus potentially leading to an increased lactate production on day 7. Aoki et al. reported a comparable observation, where they did not measure lactate levels but found that the viability of seeded cells in tracheal scaffolds decreased two days after seeding, followed by a consistent increase after an initial adaptation phase [181]. In a study by Caralt et al., decellularized whole rat kidneys were recellularized with

immortalized human renal cortical tubular epithelial (RCTE) cells. It was shown that resazurin fluorescence increased consistently, similar to the findings of this project. However, in their study lactate concentration increased gradually over the 7-day period without any decrease [191], in contrast to this project where lactate concentration decreased on day 5. However, it is also possible that the slight increase in lactate production on day 7 for recellularized PCKS-Imm within this project was due to the increase in viable cells rather than cell stress.

Cells in 2D showed the highest concentration of lactate and the lowest glucose consumption, despite having a cell viability similar to recellularized CHEM-Imm scaffolds. This suggests that RPTEC/TERT1 cells on a 2D surface may experience unfavorable nutrition conditions and higher levels of stress. Throughout this project, both recellularized PCKS-Imm and SYNTH scaffolds, as well as cells in 2D, were subjected to identical culture conditions. Notably, both were supplied with 1.5 ml of medium, implying an equal distance for oxygen and nutrients diffusion across the medium. However, considering the larger surface area of 3D scaffolds, which is known to facilitate more efficient diffusion [192], it is reasonable to assume that this contributed to enhanced oxygen and nutrients supply within the scaffolds. Furthermore, it is generally understood that cells in 2D cultures have higher oxygen consumption rates [193,194]. This implies that the increased energy consumption in 2D culture might exceed oxygen delivery through diffusion, prompting a transition towards glycolysis and resulting in higher lactate production. Other studies involving different cell types, such as mesenchymal stem cells, B lymphoma cells, and hepatocytes, have reported a similar effect where a higher lactate release was observed in 2D compared to scaffolds [195–197].

Resazurin fluorescence levels were similar between cells in 2D and those on CHEM-Imm scaffolds, corresponding to 35,000 cells on day 7 (calculated by the resazurin standard curve). This comprises 2.5% and 58% of the seeded cells on the scaffolds and the 2D well plate respectively. The surface area of the well plate used for 2D is limited (1.9 cm<sup>2</sup>). Thus, the number of seeded cells (60,000 cells) is possibly high enough to surpass the available surface area. In contrast, PCKS-Imm scaffolds, despite their smaller surface area (1.2 cm<sup>2</sup> ± 0.5 cm<sup>2</sup>) had similar resazurin levels, indicating not only surface colonization but also possibly cell migration into the deeper layers. However, only 2.5% of the initially seeded cells were present in the scaffolds on day 7. Consequently, it can be speculated that extending the incubation period may lead to increased cell presence in the scaffolds.

Glucose consumption and lactate production rates can be used to assess the metabolism in tissue-engineered constructs [191,198]. A lactate-to-glucose ratio of less than 1 suggests aerobic cell metabolism [199–201]. In this study, SYNTH scaffolds had higher lactate-to-glucose ratios compared to PCKS-Imm and PCK-Prf scaffolds.

This may be attributed to the higher cell density in SYNTH scaffolds, which may have led to limited diffusion of oxygen and nutrients into inner the areas of the scaffold, thus leading to higher lactate release through glycolysis [199]. In contrast, 2D cells exhibited the highest lactate-to-glucose ratio, indicating higher reliance on glycolysis [202]. Studies have shown that transitioning from a 2D to a 3D environment can have a significant impact on cell proliferation, differentiation and survival. Thus, leading to improved cell-cell interactions, higher stability, and enhanced functionality [202,203]. Based on the findings of this study, it is speculated that RPTEC/TERT1 cells undergo the glycolysis pathway in 2D due to stress induced by the less physiological environment. In contrast, PCKS-Imm and SYNTH scaffolds provide a more favorable environment that reduces cell stress.

### **5.4.3 Analysis of ZO-1 reveals predominance of FTC scaffolds**

The expression of ZO-1 was assessed to confirm the establishment of tight junctions. The formation of lumens is a crucial characteristic of epithelia within tubular organs such as kidneys and intestines, where they are lined by a monolayer of polarized epithelial cells with distinct apical and basolateral membranes. Establishment of tight junctions is essential for kidney homeostasis and regulation of paracellular permeability, and the expression of ZO-1 is an indication of their formation [204–206]. Remarkably, even though seeded cells in PCKS (PCKS-Imm and PCKS-Prf) were not organized into densely packed tubules, they maintained ZO-1 production with minimal direct cell-to-cell contact. This suggests that the ECM not only provides structural support but also plays a role in preserving cell signaling, thereby contributing to the maintenance of tight junctions [89].

Moreover, FTC-Imm and FTC-Prf scaffolds had the highest amount of ZO-1, suggesting that they provide a more favorable environment for seeded cells to establish tight junctions and promote the production of important proteins. As FTC-Prf, FTC-Imm and UBS60-Imm scaffolds have the lowest residual DNA levels and high ZO-1 expression, it is reasonable to speculate that residual rat DNA could potentially hinder the expression of important proteins by human RPTEC/TERT1 cells. It should be noted that cells in the differentiation process tend to proliferate at a slower rate to focus on acquiring specific functions [207,208].

Immortalized RPTEC/TERT1 cells, while not terminally differentiated, maintain luminal formation ability and several differentiation markers (e.g. tight junction formation, stable transepithelial electrical resistance, and cation transport via OCT/MATE) upon seeding in a 3D environment [200]. Thus, it can be speculated that the higher proliferation rate in CHEM-Imm scaffolds suggests that they offered a less favorable environment for the formation of tight junctions possibly due to their higher DNA content. In their study, Fedecostante et al. recellularized kidney slices with immortalized RPTEC cells and found that both ZO-1 and claudin-2 were expressed more in the recellularized slices than in the 2D model, indicating the formation of tight junctions [85]. However, assessing only tight junctions is insufficient to confirm cell polarization. Therefore, future studies should consider staining the cells against a basolateral-specific protein such as Na<sup>+</sup>/K<sup>+</sup>-adenosine triphosphatase (ATPase) or assessing cilia formation for luminal orientation. Several other studies have shown the importance of these markers to determine the orientation of kidney cells in 3D environments, such as microfluidic devices or Matrigel [31,200,209]. Nonetheless, this study's main objective was to identify the scaffold that offers the best environment for the cells.

### **5.4.4 Factors affecting cell viability in recellularized PCKS-Prf**

It was observed that the viability of seeded cells, as indicated by the resazurin assay, was generally lower in recellularized PCKS-Prf compared to PCKS-Imm. However, both CHEM-Prf and FTC-Prf received higher recellularization scores than PCKS-Imm. This difference is likely due to the higher presence of ZO-1 in recellularized PCKS-Prf scaffolds. As discussed earlier, cells in the process of differentiation tend to proliferate at a slower rate as they focus on acquiring specific functions [207,208]. Therefore, the lower proliferation rate observed in recellularized CHEM-Prf and FTC-Prf scaffolds suggests that they may have provided a more favorable environment for the formation of tight junctions despite both having four times higher residual DNA content than their immersion counterparts. This aligns with the results from the immersion approach, where CHEM-Imm exhibited a higher proliferation rate and lower ZO-1 presence. These notable differences can likely be attributed to the reduced thickness of PCKS-Prf scaffolds (500  $\mu\text{m}$ ) in comparison to PCKS-Imm scaffolds (1000  $\mu\text{m}$ ).

Thick PCKS-Imm (1000  $\mu\text{m}$ ) as well as PCKS-Prf (500  $\mu\text{m}$ ) scaffolds were recellularized under static culture conditions. As mentioned in section 1.3.2, passive diffusion is limited to 100 - 200  $\mu\text{m}$ , resulting in inadequate nutrient and oxygen supply.

Although both PCKS-Imm and PCKS-Prf scaffolds supported cell migration, the reduced numbers of seeded cells in the third layer are likely due to limited mass transfer. Nevertheless, PCKS-Prf scaffolds exhibited a higher number of cells in all investigated layers. Thus, it is reasonable to deduce that the thinner PCKS-Prf scaffolds facilitated improved diffusion, resulting in a higher production of ZO-1.

### **5.4.5 HHP200-Prf scaffolds: residual DNA and seeded cells viability**

Recellularized HHP200-Prf scaffolds displayed the lowest viability compared to all other methods in both approaches. This reduced viability aligns with the 6.5 times higher residual DNA content in HHP200-Prf scaffolds compared to HHP200-Imm scaffolds. As mentioned in section 1.3.1, residual cellular material in the scaffold causes cytocompatibility problems *in vitro*. This observation, in conjunction with the fact that rat PCKS scaffolds were recellularized with human RPTEC/TERT1 cells, suggests the possibility of a DNA-content threshold. Beyond this threshold, higher *in vitro* cytotoxicity may prevail. For instance, HHP200-Prf scaffolds, with 3500 ng/mg tissue DNA, exhibited considerably lower viability compared to FTC-Prf scaffolds, which had 1000 ng/mg tissue DNA. Importantly, DNA serves as an indicator, and its presence does not signify the presence of only DNA [30]. This is evident from the high accumulation of cytoplasmic material in HHP200-Prf scaffolds, as revealed by histological analysis.

Furthermore, while recellularized HHP200-Prf scaffolds displayed notably low cell viability, they achieved the highest score in the medium analysis assessment. However, it is important to clarify that this does not necessarily imply good performance in the respective category. The scoring system considers the lowest achieved LDH concentration as the best performance, corresponding to a score of 4. In this context, it is crucial to recognize that the low LDH concentration observed on day 7 for HHP200-Prf scaffolds is a result of the absence of viable cells and not an indication of favorable cell conditions within the HHP200-Prf scaffolds. This underscores the importance of not interpreting the results of individual medium analysis assays in isolation but rather in conjunction with the findings of all assays. Given that HHP200-Prf recellularized scaffolds exhibited the highest LDH levels on day 3, it further suggests that LDH serves as a valid indicator of elevated cellular stress levels.

### **5.4.6 All recellularized PCKS supported cell migration**

The analysis of recellularized scaffolds necessitates an investigation into seeded cell distribution and migration depth [210,211]. In this study, PCKS-Imm and PCKS-Prf scaffolds revealed the capability of supporting the migration of seeded cells throughout the scaffold. Notably, they reached even the lowest layer examined (third layer) at a depth of 300  $\mu\text{m}$ . This observation aligns with findings from numerous other studies [109,212,213]. For instance, in a study by Tang et al., Chitosan scaffolds (210  $\mu\text{m}$  thick) were seeded with hiPSCs. It was reported that the seeded cells covered the entire depth of the scaffolds. Interestingly, scaffolds preconditioned with cell culture medium (3 days) prior to recellularization exhibited the highest number of cells in the middle of the scaffold indicating that treated scaffolds provided a conducive environment for cell penetration [213]. However, contrary to the findings of Tang et al., while all PCKS-Imm and PCKS-Prf in this project were pre-conditioned with cell culture medium (24 h) before seeding, both CHEM-Imm and FTC-Imm scaffolds demonstrated a gradual decrease in the number of seeded cells per layer.

### **5.4.7 Seeded cells growth: renal vs. intestinal epithelial cells**

In a master thesis conducted within this project [214], CHEM-Imm scaffolds were recellularized with two different cell types: Caco-2 cells (colon carcinoma epithelial cells) and RPTEC/TERT1 cells. The distribution of these cells within the scaffolds exhibited notable differences. While most of the seeded Caco-2 cells remained within a maximum depth of 60  $\mu\text{m}$ , RPTEC/TERT1 cells reached a depth of 220  $\mu\text{m}$ . Furthermore, fluorescence microscopy revealed significant distinctions between the two groups. Scaffolds seeded with RPTEC/TERT1 cells displayed a distinctive cell alignment, forming empty circular structures in the renal cortex, presumably corresponding to Bowman capsules (BC). Additionally, seeded cells exhibited a linear pattern from the cortex into the medulla, resembling the formation of collecting ducts (Figure S 15). In contrast, Caco-2 cells did not exhibit any notable development of cellular alignments along the scaffold structure and appeared to populate almost the entire scaffold surface in a non-specific manner (Figure S 16). This observation raised questions about whether RPTEC/TERT1 cells can indeed adhere specifically to their tubular locations on the scaffold.

### 5.4.8 Artificial intelligence revealed specific recellularization

The kidney is a complex organ consisting of over 30 different cell types [36]. As mentioned previously, cells have the ability to migrate through the ECM by undergoing cytoskeletal rearrangements [58]. Therefore, it became crucial to ascertain whether RPTEC/TERT1 cells were successfully attached to their proximal convoluted tubules (PCT) locations. Hence, it was imperative to develop a method to visualize the location of the seeded cells on the recellularized PCKS (PCKS-Imm and PCKS-Prf). While immunofluorescence could potentially enable this assessment, staining the recellularized scaffold with antibodies against the locations of all cell types is technically extremely demanding due to the multitude of antibodies required. The choice of the Bowman's capsule (BC) for assessment was based on the indication that the presence of seeded cells within it would suggest nonspecific recellularization. Consequently, it was essential to visualize both the PCTs and the BCs in order to count the number of cells attached to each one of them. However, major ECM proteins such as Col-IV and laminin are present in both the BC and tubules, making it difficult to differentiate between these locations once stained with an antibody [48]. Moreover, literature did not provide precise information on proteins specific to only one location requiring the development of an alternative method.

A method was developed involving staining the scaffolds against Col-IV to visualize all functional units. Utilizing artificial neural networks (ANN), the BCs were automatically identified. Cells attached outside the BCs were considered indicative of specific recellularization, although it should be noted that structures other than the PCT are also present outside the BC. The identification of BCs from other structures was possible due to their larger size. However, it was challenging to differentiate between PCTs and DCTs, as they exhibited similar morphological features. Therefore, while this method provided insights into specific recellularization, it did not definitively establish whether cells outside the BCs were attached on scaffold structures originally associated with PCTs.

Interestingly, the analysis of the recellularized PCKS revealed that the majority of seeded cells were located outside the BCs, regardless of the decellularization method used. Even in HHP200-Imm scaffolds, which had the highest percentage of seeded cells inside the BC (3.5%), the majority (more than 96%) of cells were found outside. This indicates that all decellularization methods applied within this project were relatively successful in preserving the ECM. The higher number of cells outside the BCs in recellularized FTC-Imm and UBS60-Imm scaffolds could be attributed to their lower DNA

content compared to CHEM-Imm, CHEM-Prf and HHP200-Imm scaffolds. Moreover, the structural analysis within the scoring system demonstrated that the BCs and the tubules received comparable scores (Figure S 5), suggesting that the preference of RPTEC/TERT1 cells to be positioned outside the BCs in recellularized PCKS is not solely influenced by extensive damage to the BCs. On the other hand, cells seeded on SYNTH scaffolds and stained against Col-IV exhibited a non-uniform distribution of cells without distinct alignments resembling kidney functional units (Figure S 14). Thus, underscoring the importance of using a scaffold that includes embedded functional units such as decellularized PCKS. In conclusion, seeded cells avoided the attachment inside the BC, although it consists of locations for seven different cell types [25]. Thus highlighting the ability of RPTEC/TERT1 cells for directed cell migration, which is commonly observed in vivo [215].

### **5.4.9 Seeded cells exhibited the ability for directed migration**

The ECM plays a crucial role in providing signals that guide cell attachment, migration, and differentiation [14,15,44]. Therefore, it is possible that the decellularized PCKS (PCKS-Imm and PCKS-Prf) although partially, preserved ECM components, which directed cell migration through haptotaxis. The tubules within the kidney may contain specific proteins or GFs, that create a gradient. Haptotaxis-driven cell migration has been observed in various cell types, including mesenchymal stem cells, T cells, fibroblasts, myoblasts, endothelial cells, Schwann cells, neurons, and cancer cells [216–222]. Weber et. al. demonstrated that dendritic cells exhibit directed migration towards lymph vessels in response to endogenous gradients of the chemokine CCL21 embedded within mouse skin [223]. Additionally, fibroblasts and human mesenchymal stem cells can migrate in vitro on polyacrylamide hydrogels that are coated with gradients of the arginine-glycine-aspartic acid (RGD) motif and collagen [219].

Topotaxis is another mechanism that may have influenced the directed cell migration in recellularized PCKS. The decellularization process partially preserved the microarchitecture of the ECM, as indicated by histological and SEM analysis. As described in section 1.2.2, different regions within the ECM vary in their components and abundance, which exist in different isoforms. For example, there are seven Col-IV and twelve laminin isoforms [224]. These differences can influence the stiffness, elasticity and overall mechanical behavior of tissues. Therefore, it is possible that the differential composition and spatial distribution of ECM components contributed to topotaxis in recellularized PCKS. Topotaxis has been observed in fibroblasts, neurons, mesenchymal stem cells, endothelial, epithelial and melanoma cells [225–230].

A research study utilized engineered surfaces that mimic the fibers of the ECM. When the density of the fibers was changed, fibroblasts and melanoma cells exhibited directional migration along the gradient, and their orientation and shape were affected by the topographical differences [62]. Moreover, it was demonstrated that an anisotropic micro- and nanopattern array, incorporating topographical features such as ridges and varying density, induced migration of fibroblasts along the density variations [231].

### **5.4.10 SEM reveals microvilli in recellularized PCKS**

The recellularized PCKS (PCKS-Imm and PCKS-Prf) were analyzed with SEM. In native kidney tissue, RPTEC cells exhibit a distinct cuboidal shape with a densely packed microvilli brush border [40,41]. This characteristic was also confirmed in SEM images of the native rat kidney in this project. Interestingly, similar microvilli were also observed in the seeded RPTEC/TERT1 cells on PCKS scaffolds, although they appeared more in an oval shape and only partially resembled the shape of native cells. It can be speculated that a longer incubation beyond 7 days may potentially lead them closer to the native cell shape. On the other hand, smaller, less oval, and more rounded seeded cells with protruding structures resembling bubbles were also observed. Tinari et al. reported similar morphological changes indicative of apoptosis including the formation of surface protrusions like blebs and blisters, cell rounding and shrinking, cell retraction, and loss of cell-substrate interaction [232]. However, the results of the resazurin and LDH assays within this study indicated that cell growth was supported by the scaffolds over time. Nevertheless, it is recommended that future studies incorporate apoptosis assays to provide a better understanding of seeded cells viability.

## **5.5 Optimization of perfusion decellularization after HHP treatment**

HHP200-Prf achieved the second lowest total score, reflecting the challenges associated with HHP-induced tissue compression, which might have caused constrictions in the vascular network, thereby hindering perfusion during decellularization. To address this issue, the indirect decellularization approach was used for HHP-treated kidneys. In both direct and indirect decellularization approaches, the use of 1% SDS and 0.5% SDS resulted in only a 24% reduction in DNA content, aligning with the high accumulation of cytoplasmic and nuclear material. This can likely be attributed to the relatively low volume of perfused SDS (144 ml). It is worth noting that the SDS1% protocol used in this study was adopted from Ciampi et al., where DNA results were not reported, but successful recellularization was achieved [122]. A study by He et al. demonstrated that decellularizing rat kidneys with

2400 ml of 1% or 0.5% SDS achieved over 99% reduction in residual DNA content [144]. This highlights the effectiveness of using FTC as a physical pretreatment, as it consistently achieved an 85% or greater reduction in DNA content in both decellularization approaches, despite using only 144 ml SDS. In contrast, HHP100-SDS1% of the direct decellularization approach was found to be entirely ineffective. However, the introduction of a PBS perfusion step in the indirect approach after HHP treatment significantly improved the outcome. HHP150-SDS0.5% achieved a 64% reduction in DNA content.

This result suggests that the HHP-induced vasculature compression may have been at least partially resolved, facilitating the more efficient flow of SDS0.5%. In contrast, while FTC-SDS1% yielded the highest reduction in DNA content, FTC-SDS0.5% of the indirect approach achieved a slightly lower reduction due to the lower SDS concentration. This suggests that PBS perfusion after FTC treatment did not yield additional benefits, further confirming that the vascular network was not constricted. However, it is imperative to assess the vascular integrity post-decellularization in future studies as described earlier.

The significant reduction in DNA in HHP150-SDS0.5% scaffolds of the indirect approach underscores the effectiveness of introducing PBS perfusion after HHP treatment. However, it is advisable to monitor the arterial pressure during decellularization to ascertain whether there is a pressure drop during PBS perfusion after HHP treatment, thereby confirming its role in vascular deconstriction. Moreover, GAGs content was significantly reduced and the ECM structures were more damaged compared to PCKS-Imm and PCKS-Prf. Nevertheless, this simple SDS protocol was used for comparative purposes. It is recommended to introduce a PBS perfusion step after HHP treatment in the CHEM-Prf protocol, which was less aggressive and achieved a comparable DNA reduction.

### **5.6 Reactivity of PBMCs to native and decellularized kidneys**

Transplantation of rat kidneys post-recellularization has the risk of immune rejection. This preliminary study utilized PBMCs to lay the groundwork for in vitro investigations of immunological responses of decellularized kidneys. Thus, reducing the number of rats sacrificed without achieving a meaningful experimental outcome. IL-2 is responsible for promoting the proliferation and differentiation of T-helper cells, B-lymphocytes, and natural killer cells upon binding of an antigen [233]. An increased resazurin fluorescence was observed in PBMCs incubated with IL-2 compared to untreated cells, which was a similar effect as reported in other studies [173,234].

In two independent studies, the reaction of PBMCs to native and decellularized rat liver and kidney scaffolds was investigated, upon incubation for 24 h. In both cases, PBMCs incubated with native organ homogenates exhibited around more than twice the cell viability compared to untreated PBMCs, which aligns with the results in this project. However, incubation of PBMCs with decellularized liver or kidney homogenate showed a similar level of viability compared to untreated PBMCs [173,234]. In contrast to this study, resazurin fluorescence intensity for PBMCs incubated with decellularized homogenates was 50% lower than that of untreated PBMCs. Decellularized kidney homogenates used in this study are from scaffolds decellularized according to the SDS1% protocol, which showed a high accumulation of residual DNA. As described above, high amounts of residual DNA in recellularized HHP200-Prf scaffolds led to significantly lower seeded cell viability. Therefore, it is speculated that incubation of PBMCs with decellularized kidney homogenates resulted in an inhibition of cellular metabolic activity due to the DNA content. Nevertheless, specific immunogenicity assays should be incorporated in future studies to specifically investigate the immune response. For instance, the expression of inducible nitric oxide synthase (iNOS) can be measured [173,234]. In a study by Hussein et. al., decellularized kidneys did not increase the expression of iNOS. However, the native kidney stimulated the expression of iNOS compared to untreated PBMCs [234]. Other assays, such as quantifying cytokines (e.g. IL-17, IL-4, TNF- $\alpha$ , IL-10) with flow cytometry or ELISA, can be employed. [235,236]. Additionally, PBMC migration assays toward the stimulus, (e.g. native or decellularized scaffolds), can provide valuable insights [237]. Moreover, flow cytometry can be used to investigate specific cell membrane markers [236].

## 6 Conclusions and future aspects

In this study, rat PCKS served as a model to investigate decellularization strategies. A comprehensive comparison of various physical treatment methods (HHP, UBS, and FTC), combined with a protocol for PCKS decellularization through immersion in chemicals (CHEM-Imm), was conducted. The findings showed that the most effective method for achieving a balance between a significant reduction in DNA content and the preservation of GAGs as well as ECM structural integrity is the combination of FTC with CHEM-Imm. This work provides, for the first time, a comparison of three physical treatment methods for kidney tissues, establishing an essential foundation for further investigations into the decellularization of whole rat kidneys.

The insights gained from the immersion decellularization of PCKS-Imm were applied to the decellularization of whole kidneys. Score analysis indicated that treating kidney slices or whole kidneys with FTC, followed by immersion and perfusion decellularization, can yield scaffolds that support a favorable cellular environment. Consequently, using PCKS as a model in the immersion approach successfully identified the preferred method, reducing the need for animal sacrifice compared to whole kidney decellularization. In this context, this study, for the first time, provides clues indicating that decellularized ECM provides not only an instructive memory for a location-specific stem cell differentiation but also influences the migration of immortalized RPTEC/TERT1 cells toward their specific locations.

However, it is recommended to avoid static culture of PCKS by using a bioreactor to facilitate mass transport and cell migration. Furthermore, recellularizing PCKS with multiple cell types and incubation for longer periods, can enhance the mimicry of the native kidney's complexity, facilitating better tissue maturation [238–240]. However, seeding PCKS with just one cell type for seven days incubation is primarily for the purpose of comparing decellularization methods. Moreover, it is essential to investigate the functionality of recellularized PCKS, especially concerning tubular reabsorption and secretion (e.g. water reabsorption, Na<sup>+</sup> and glucose uptake) [107,200]. Nevertheless, creating a transplantable kidney requires the de- and recellularization of the whole organ by perfusion. However, when considering recellularization for transplantation, the use of immortalized cell lines (RPTEC/TERT1) must be replaced by stem cells.

There is a pressing need for improved kidney models for drug screening and nephrotoxicity assessments that encompass multiple functional units. Since decellularized PCKS already includes the

respective locations and structures of all functional units of the kidney, it can be recellularized with several cell types such as RPTEC/TERT1 cells, endothelial cells and podocytes. This approach allows the creation of a coculture model comprising two vital functional units: the proximal tubule and glomerulus. This feature positions the PCKS model as more advantageous compared to SYNTH scaffolds, which have randomly organized glass fibers and lack specific structures of the kidney functional units.

In light of these considerations, a single rat kidney can yield twelve PCKS by cutting it into 1000  $\mu\text{m}$  slices for immersion decellularization. This quantity can potentially be optimized to 24 slices by reducing the thickness to 500  $\mu\text{m}$ . With each PCKS approximately measuring 1.2  $\text{cm}^2$ , it can be further subdivided into smaller pieces, resulting in the creation of 100 replicates (4 x 25) from one original slice. Such small sections of the original PCKS may provide sufficiently large pieces for use in drug testing. However, a pertinent question arises regarding sacrificing a rat to create PCKS for drug testing. The genuine advantage of utilizing recellularized PCKS compared to existing 3D models, remains uncertain. Therefore, it is imperative to evaluate the efficacy of recellularized PCKS in drug testing in comparison to available 3D models, including organoids, organ-on-chips, and bio-printed scaffolds.

Further development of the FTC-Prf protocol towards the recellularization of whole rat kidneys with stem cells is a very important aspect in kidney tissue engineering (TE). However, ensuring cell coverage of the whole vascular network and tubular system during recellularization is a primary challenge in kidney TE [9]. Nonetheless, as advancements continue in the differentiation of renal hiPSCs, innovations in TE, and bioreactors design, the prospect of successfully generating entire kidneys for transplantation could become a reality. The findings of this thesis contribute to the research needed towards realizing this goal.

## 7 References

- [1] C. P. Kovesdy, "Epidemiology of chronic kidney disease: an update 2022," *Kidney international supplements*, vol. 12, no. 1, pp. 7–11, 2022.
- [2] "Global, regional, and national burden of chronic kidney disease, 1990-2017: a systematic analysis for the Global Burden of Disease Study 2017," *Lancet (London, England)*, vol. 395, no. 10225, pp. 709–733, 2020.
- [3] K. J. Foreman, N. Marquez, A. Dolgert et al., "Forecasting life expectancy, years of life lost, and all-cause and cause-specific mortality for 250 causes of death: reference and alternative scenarios for 2016-40 for 195 countries and territories," *Lancet (London, England)*, vol. 392, no. 10159, pp. 2052–2090, 2018.
- [4] J. S. Uzarski, Y. Xia, J. C. Belmonte et al., "New strategies in kidney regeneration and tissue engineering," *Current opinion in nephrology and hypertension*, vol. 23, no. 4, 2014.
- [5] N. Montserrat, E. Garreta, and J. C. Izpisua Belmonte, "Regenerative strategies for kidney engineering," *The FEBS journal*, vol. 283, no. 18, pp. 3303–3324, 2016.
- [6] S. Vadakedath and V. Kandi, "Dialysis: A Review of the Mechanisms Underlying Complications in the Management of Chronic Renal Failure," *Cureus*, vol. 9, no. 8, e1603-e1603, 2017.
- [7] S. Yamamoto, J. J. Kazama, T. Wakamatsu et al., "Removal of uremic toxins by renal replacement therapies: a review of current progress and future perspectives," *Renal Replacement Therapy*, vol. 2, no. 1, p. 43, 2016.
- [8] N. Pooornejad, L. B. Schaumann, E. M. Buckmiller et al., "Current Cell-Based Strategies for Whole Kidney Regeneration," *Tissue engineering. Part B, Reviews*, vol. 22, no. 5, pp. 358–370, 2016.
- [9] M. J. de Haan, F. M. Witjas, M. A. Engelse et al., "Have we hit a wall with whole kidney decellularization and recellularization: A review," *Current Opinion in Biomedical Engineering*, vol. 20, p. 100335, 2021.
- [10] C. A. Batchelder, M. L. Martinez, and A. F. Tarantal, "Natural Scaffolds for Renal Differentiation of Human Embryonic Stem Cells for Kidney Tissue Engineering," *PLOS ONE*, vol. 10, no. 12, e0143849-e0143849, 2015.
- [11] German Organ Transplantation Foundation, "Jahresbericht Organspende und Transplantation in Deutschland," 2023, <https://dso.de/organspende/statistiken-berichte/jahresbericht>.

## 7 References

---

- [12] B. Almoguera, A. Shaked, and B. J. Keating, "Transplantation genetics: current status and prospects," *American Journal of Transplantation*, vol. 14, no. 4, pp. 764–778, 2014.
- [13] S. F. Badylak, D. Taylor, and K. Uygun, "Whole-organ tissue engineering: decellularization and recellularization of three-dimensional matrix scaffolds," *Annual review of biomedical engineering*, vol. 13, pp. 27–53, 2011.
- [14] S. Yi, F. Ding, L. Gong et al., "Extracellular Matrix Scaffolds for Tissue Engineering and Regenerative Medicine," *Current stem cell research & therapy*, vol. 12, no. 3, pp. 233–246, 2017.
- [15] M. Fedecostante, O. G. Onciu, K. G. C. Westphal et al., "Towards a bioengineered kidney: recellularization strategies for decellularized native kidney scaffolds," *The International journal of artificial organs*, vol. 40, no. 4, pp. 150–158, 2017.
- [16] C. G. Lebedenko and I. A. Banerjee, "Enhancing Kidney Vasculature in Tissue Engineering—Current Trends and Approaches: A Review," *Biomimetics*, vol. 6, no. 2, 2021.
- [17] R. P. Anand, J. V. Layer, D. Heja et al., "Design and testing of a humanized porcine donor for xenotransplantation," *Nature*, vol. 622, no. 7982, pp. 393–401, 2023.
- [18] M. E. Scarritt, N. C. Pashos, and B. A. Bunnell, "A review of cellularization strategies for tissue engineering of whole organs," *Frontiers in bioengineering and biotechnology*, vol. 3, p. 43, 2015.
- [19] J. P. Guyette, S. E. Gilpin, J. M. Charest et al., "Perfusion decellularization of whole organs," *Nature protocols*, vol. 9, no. 6, pp. 1451–1468, 2014.
- [20] T. C. Fuchs and P. Hewitt, "Biomarkers for drug-induced renal damage and nephrotoxicity—an overview for applied toxicology," *The AAPS journal*, vol. 13, no. 4, pp. 615–631, 2011.
- [21] M. A. Perazella, "Pharmacology behind Common Drug Nephrotoxicities," *Clinical Journal of the American Society of Nephrology*, vol. 13, no. 12, 2018.
- [22] H. Y. Tiong, P. Huang, S. Xiong et al., "Drug-Induced Nephrotoxicity: Clinical Impact and Pre-clinical in Vitro Models," *Molecular Pharmaceutics*, vol. 11, no. 7, pp. 1933–1948, 2014.
- [23] C. A. Naughton, "Drug-induced nephrotoxicity," *American family physician*, vol. 78, no. 6, pp. 743–750, 2008.
- [24] W. S. Redfern, R. A. Bialecki, L. Ewart et al., "Impact and prevalence of safety pharmacology-related toxicities throughout the pharmaceutical life cycle," *Journal of Pharmacological and Toxicological Methods*, vol. 62, 2010.
- [25] M. S. Balzer, T. Rohacs, and K. Susztak, "How Many Cell Types Are in the Kidney and What Do They Do?," *Annual review of physiology*, vol. 84, pp. 507–531, 2022.
- [26] N. Nakhoul and V. Batuman, "Role of Proximal Tubules in the Pathogenesis of Kidney Disease," in *Contributions to Nephrology : Contrib Nephrol*, vol. 169, pp. 37–50, 2011.

## 7 References

---

- [27] K. A. Homan, D. B. Kolesky, M. A. Skylar-Scott et al., “Bioprinting of 3D Convulated Renal Proximal Tubules on Perfusable Chips,” *Scientific Reports*, vol. 6, no. 1, p. 34845, 2016.
- [28] S. M. King, J. W. Higgins, C. R. Nino et al., “3D Proximal Tubule Tissues Recapitulate Key Aspects of Renal Physiology to Enable Nephrotoxicity Testing,” *Frontiers in physiology*, vol. 8, p. 123, 2017.
- [29] D. Kleinknecht, P. Landais, and B. Goldfarb, “Drug-Associated Acute Renal Failure. A Prospective Collaborative Study of 81 Biopsied Patients,” in *Acute Renal Failure: Clinical and Experimental*, A. Amerio, P. Coratelli, V. M. Campese et al., Eds., pp. 125–128, Springer US, Boston, MA, 1987.
- [30] T. M. DesRochers, L. Suter, A. Roth et al., “Bioengineered 3D Human Kidney Tissue, a Platform for the Determination of Nephrotoxicity,” *PLoS one*, vol. 8, no. 3, e59219, 2013.
- [31] E. J. Weber, A. Chapron, B. D. Chapron et al., “Development of a microphysiological model of human kidney proximal tubule function,” *Kidney International*, vol. 90, no. 3, pp. 627–637, 2016.
- [32] A. Hoppensack, C. C. Kazanecki, D. Colter et al., “A human in vitro model that mimics the renal proximal tubule,” *Tissue Engineering Part C: Methods*, vol. 20, no. 7, pp. 599–609, 2014.
- [33] A. Petrosyan, P. Cravedi, V. Villani et al., “A glomerulus-on-a-chip to recapitulate the human glomerular filtration barrier,” *Nature Communications*, vol. 10, no. 1, p. 3656, 2019.
- [34] L. Wang, T. Tao, W. Su et al., “A disease model of diabetic nephropathy in a glomerulus-on-a-chip microdevice,” *Lab on a chip*, vol. 17, no. 10, pp. 1749–1760, 2017.
- [35] N. Gupta, E. Dilmen, and R. Morizane, “3D kidney organoids for bench-to-bedside translation,” *Journal of Molecular Medicine*, vol. 99, no. 4, pp. 477–487, 2021.
- [36] J. P. Zambon, P. Chandra, A. Atala et al., “Chapter 33 - Renal System,” in *Translational Regenerative Medicine*, A. Atala and J. G. Allickson, Eds., pp. 457–468, Academic Press, Boston, 2015.
- [37] Gordon Betts J, Desaix P, Johnson E, *Anatomy & Physiology: The urinary system*, OpenStax, Houston, Texas, USA, 2022.
- [38] M. C. Menon, P. Y. Chuang, C. J. He et al., “The Glomerular Filtration Barrier: Components and Crosstalk,” *International Journal of Nephrology*, vol. 2012, p. 749010, 2012.
- [39] M. A. Breshears and A. W. Confer, “Chapter 11 - The Urinary System1,” in *Pathologic Basis of Veterinary Disease (Sixth Edition)*, J. F. Zachary, Ed., 617-681.e1, Mosby, 2017.
- [40] M. Taub, “Primary kidney cells,” *Methods in molecular biology (Clifton, N.J.)*, vol. 75, pp. 153–161, 1997.

## 7 References

---

- [41] B. A. Molitoris and M. C. Wagner, "Surface membrane polarity of proximal tubular cells: Alterations as a basis for malfunction," *Kidney International*, vol. 49, no. 6, pp. 1592–1597, 1996.
- [42] D. B. Mount, "Thick ascending limb of the loop of Henle," *Clinical Journal of the American Society of Nephrology*, vol. 9, no. 11, pp. 1974–1986, 2014.
- [43] J. A. McCormick and D. H. Ellison, "Distal convoluted tubule," *Comprehensive Physiology*, vol. 5, no. 1, pp. 45–98, 2015.
- [44] C. Frantz, K. M. Stewart, and V. M. Weaver, "The extracellular matrix at a glance," *Journal of Cell Science*, vol. 123, no. 24, pp. 4195–4200, 2010.
- [45] R. Lennon, "Chapter 59 - Extracellular Matrix Biology Applied to the Kidney," in *Kidney Transplantation, Bioengineering and Regeneration*, G. Orlando, G. Remuzzi, and D. F. Williams, Eds., pp. 829–841, Academic Press, 2017.
- [46] D. A. C. Walma and K. M. Yamada, "The extracellular matrix in development," *Development (Cambridge, England)*, vol. 147, no. 10, 2020.
- [47] R. V. Iozzo and M. A. Gubbiotti, "Extracellular matrix: The driving force of mammalian diseases," *Matrix Biology*, 71-72, pp. 1–9, 2018.
- [48] R. D. Bülow and P. Boor, "Extracellular Matrix in Kidney Fibrosis: More Than Just a Scaffold," *The journal of histochemistry and cytochemistry : official journal of the Histochemistry Society*, vol. 67, no. 9, pp. 643–661, 2019.
- [49] A. D. Theocharis, S. S. Skandalis, C. Gialeli et al., "Extracellular matrix structure," *Advanced Drug Delivery Reviews*, vol. 97, pp. 4–27, 2016.
- [50] N. K. Karamanos, A. D. Theocharis, Z. Piperigkou et al., "A guide to the composition and functions of the extracellular matrix," *The FEBS journal*, vol. 288, no. 24, pp. 6850–6912, 2021.
- [51] A. P. Drain and V. M. Weaver, "Chapter 7 - Matrix molecules and their ligands," in *Principles of Tissue Engineering (Fifth Edition)*, R. Lanza, R. Langer, J. P. Vacanti et al., Eds., pp. 119–132, Academic Press, 2020.
- [52] T. Rozario and D. W. DeSimone, "The extracellular matrix in development and morphogenesis: A dynamic view," *Developmental Biology*, vol. 341, no. 1, pp. 126–140, 2010.
- [53] D. F. Boyd and P. G. Thomas, "Towards integrating extracellular matrix and immunological pathways," *Cytokine*, vol. 98, pp. 79–86, 2017.
- [54] F. Genovese, A. A. Manresa, D. J. Leeming et al., "The extracellular matrix in the kidney: a source of novel non-invasive biomarkers of kidney fibrosis?," *Fibrogenesis & Tissue Repair*, vol. 7, no. 1, p. 4, 2014.

## 7 References

---

- [55] V. W. Tang, "Collagen, stiffness, and adhesion: the evolutionary basis of vertebrate mechanobiology," *Molecular biology of the cell*, vol. 31, no. 17, pp. 1823–1834, 2020.
- [56] K. Legerstee and A. B. Houtsmuller, "A Layered View on Focal Adhesions," *Biology*, vol. 10, no. 11, 2021.
- [57] M. Mavrakis and M. A. Juanes, "The compass to follow: Focal adhesion turnover," *Current Opinion in Cell Biology*, vol. 80, p. 102152, 2023.
- [58] X. Trepats, Z. Chen, and K. Jacobson, "Cell migration," *Comprehensive Physiology*, vol. 2, no. 4, pp. 2369–2392, 2012.
- [59] A. J. Boys and R. M. Owens, "Measuring cellular contraction: Current progress and a future in bioelectronics," *APL Materials*, vol. 9, no. 4, p. 40903, 2021.
- [60] S. SenGupta, C. A. Parent, and J. E. Bear, "The principles of directed cell migration," *Nature Reviews Molecular Cell Biology*, vol. 22, no. 8, pp. 529–547, 2021.
- [61] M. M. Thibault, C. D. Hoemann, and M. D. Buschmann, "Fibronectin, Vitronectin, and Collagen I Induce Chemotaxis and Haptotaxis of Human and Rabbit Mesenchymal Stem Cells in a Standardized Transmembrane Assay," *Stem Cells and Development*, vol. 16, no. 3, pp. 489–502, 2007.
- [62] J. Park, D.-H. Kim, and A. Levchenko, "Topotaxis: A New Mechanism of Directed Cell Migration in Topographic ECM Gradients," *Biophysical Journal*, vol. 114, no. 6, pp. 1257–1263, 2018.
- [63] K. N. Murphy and A. J. Brinkworth, "Manipulation of Focal Adhesion Signaling by Pathogenic Microbes," *International journal of molecular sciences*, vol. 22, no. 3, 2021.
- [64] P. K. Chandra, S. Soker, and A. Atala, "Chapter 1 - Tissue engineering: current status and future perspectives," in *Principles of Tissue Engineering (Fifth Edition)*, R. Lanza, R. Langer, J. P. Vacanti et al., Eds., pp. 1–35, Academic Press, 2020.
- [65] P. M. Crapo, T. W. Gilbert, and S. F. Badylak, "An overview of tissue and whole organ decellularization processes," *Biomaterials*, vol. 32, no. 12, pp. 3233–3243, 2011.
- [66] E. Garreta, R. Oria, C. Tarantino et al., "Tissue engineering by decellularization and 3D bioprinting," *Materials Today*, vol. 20, no. 4, pp. 166–178, 2017.
- [67] S. Baiguera, C. Del Gaudio, E. Kuevda et al., "Dynamic decellularization and cross-linking of rat tracheal matrix," *Biomaterials*, vol. 35, no. 24, pp. 6344–6350, 2014.
- [68] H. C. Ott, T. S. Matthiesen, S.-K. Goh et al., "Perfusion-decellularized matrix: using nature's platform to engineer a bioartificial heart," *Nature Medicine*, vol. 14, no. 2, pp. 213–221, 2008.

## 7 References

---

- [69] T. K. Rajab, T. J. O'Malley, and V. Tchantchaleishvili, "Decellularized scaffolds for tissue engineering: Current status and future perspective," *Artificial Organs*, vol. 44, no. 10, pp. 1031–1043, 2020.
- [70] Y. Wang, C. T. Nicolas, H. S. Chen et al., "Recent Advances in Decellularization and Recellularization for Tissue-Engineered Liver Grafts," *Cells Tissues Organs*, vol. 204, 3-4, pp. 125–136, 2017.
- [71] T. J. Keane, I. T. Swinehart, and S. F. Badylak, "Methods of tissue decellularization used for preparation of biologic scaffolds and in vivo relevance," *Methods (San Diego, Calif.)*, vol. 84, pp. 25–34, 2015.
- [72] U. Mendibil, R. Ruiz-Hernandez, S. Retegi-Carrion et al., "Tissue-Specific Decellularization Methods: Rationale and Strategies to Achieve Regenerative Compounds," *International journal of molecular sciences*, vol. 21, no. 15, p. 5447, 2020.
- [73] M. Rabbani, N. Zakian, and N. Alimoradi, "Contribution of Physical Methods in Decellularization of Animal Tissues," *Journal of medical signals and sensors*, vol. 11, no. 1, pp. 1–11, 2021.
- [74] D. Moffat, K. Ye, and S. Jin, "Decellularization for the retention of tissue niches," *Journal of tissue engineering*, vol. 13, 20417314221101151, 2022.
- [75] T. K. Rajab, T. J. O'Malley, and V. Tchantchaleishvili, "Decellularized scaffolds for tissue engineering: Current status and future perspective," *Artificial Organs*, vol. 44, no. 10, pp. 1031–1043, 2020.
- [76] N. Rivalain, J. Roquain, and G. Demazeau, "Development of high hydrostatic pressure in biosciences: Pressure effect on biological structures and potential applications in Biotechnologies," *Biotechnology Advances*, vol. 28, no. 6, pp. 659–672, 2010.
- [77] E. G. Santoso, K. Yoshida, Y. Hirota et al., "Application of detergents or high hydrostatic pressure as decellularization processes in uterine tissues and their subsequent effects on in vivo uterine regeneration in murine models," *PLoS one*, vol. 9, no. 7, e103201, 2014.
- [78] J. Negishi, S. Funamoto, T. Kimura et al., "Porcine radial artery decellularization by high hydrostatic pressure," *Journal of tissue engineering and regenerative medicine*, vol. 9, no. 11, E144–E151, 2015.
- [79] Y. Hashimoto, S. Funamoto, S. Sasaki et al., "Preparation and characterization of decellularized cornea using high-hydrostatic pressurization for corneal tissue engineering," *Biomaterials*, vol. 31, no. 14, pp. 3941–3948, 2010.

## 7 References

---

- [80] Y. Hashimoto, S. Funamoto, T. Kimura et al., “The effect of decellularized bone/bone marrow produced by high-hydrostatic pressurization on the osteogenic differentiation of mesenchymal stem cells,” *Biomaterials*, vol. 32, no. 29, pp. 7060–7067, 2011.
- [81] N. Watanabe, M. Mizuno, J. Matsuda et al., “Comparison of High-Hydrostatic-Pressure Decellularized Versus Freeze-Thawed Porcine Menisci,” *Journal of orthopaedic research : official publication of the Orthopaedic Research Society*, vol. 37, no. 11, pp. 2466–2475, 2019.
- [82] N. Charoensombut, K. Kawabata, J. Kim et al., “Internal radial perfusion bioreactor promotes decellularization and recellularization of rat uterine tissue,” *Journal of Bioscience and Bioengineering*, vol. 133, no. 1, pp. 83–88, 2022.
- [83] M. Lorenz, F. Poosch, M. Meyer et al., *Ultrasonic treatment for decellularisation of cartilage and dura mater*, 2021.
- [84] J. P. Zambon, I. K. Ko, M. Abolbashari et al., “Comparative analysis of two porcine kidney decellularization methods for maintenance of functional vascular architectures,” *Acta Biomaterialia*, vol. 75, pp. 226–234, 2018.
- [85] M. Fedecostante, K. G. C. Westphal, M. F. Buono et al., “Recellularized Native Kidney Scaffolds as a Novel Tool in Nephrotoxicity Screening,” *Drug Metabolism and Disposition*, vol. 46, no. 9, p. 1338, 2018.
- [86] A. Peloso, A. Petrosyan, S. Da Sacco et al., “Renal Extracellular Matrix Scaffolds From Discarded Kidneys Maintain Glomerular Morphometry and Vascular Resilience and Retains Critical Growth Factors,” *Transplantation*, vol. 99, no. 9, pp. 1807–1816, 2015.
- [87] P. Mallis, C. Oikonomidis, Z. Dimou et al., “Optimizing Decellularization Strategies for the Efficient Production of Whole Rat Kidney Scaffolds,” *Tissue engineering and regenerative medicine*, vol. 18, no. 4, pp. 623–640, 2021.
- [88] H. Feng, Y. Xu, S. Luo et al., “Evaluation and preservation of vascular architectures in decellularized whole rat kidneys,” *Cryobiology*, vol. 95, pp. 72–79, 2020.
- [89] T. Bongolan, J. Whiteley, J. Castillo-Prado et al., “Decellularization of porcine kidney with submicellar concentrations of SDS results in the retention of ECM proteins required for the adhesion and maintenance of human adult renal epithelial cells,” *Biomaterials science*, vol. 10, no. 11, pp. 2972–2990, 2022.
- [90] S. Bombelli, C. Meregalli, C. Scalia et al., “Nephrosphere-Derived Cells Are Induced to Multilineage Differentiation when Cultured on Human Decellularized Kidney Scaffolds,” *The American journal of pathology*, vol. 188, no. 1, pp. 184–195, 2018.

## 7 References

---

- [91] I. Fischer, M. Westphal, B. Rossbach et al., “Comparative characterization of decellularized renal scaffolds for tissue engineering,” *Biomedical materials (Bristol, England)*, vol. 12, no. 4, p. 45005, 2017.
- [92] K. H. Nakayama, C. C. I. Lee, C. A. Batchelder et al., “Tissue Specificity of Decellularized Rhesus Monkey Kidney and Lung Scaffolds,” *PLOS ONE*, vol. 8, no. 5, e64134, 2013.
- [93] N. K. Singh, W. Han, S. A. Nam et al., “Three-dimensional cell-printing of advanced renal tubular tissue analogue,” *Biomaterials*, vol. 232, p. 119734, 2020.
- [94] N. Poornejad, N. Momtahan, A. S. M. Salehi et al., “Efficient decellularization of whole porcine kidneys improves reseeded cell behavior,” *Biomedical materials (Bristol, England)*, vol. 11, no. 2, p. 25003, 2016.
- [95] N. Poornejad, T. S. Frost, D. R. Scott et al., “Freezing/Thawing without Cryoprotectant Damages Native but not Decellularized Porcine Renal Tissue,” *Organogenesis*, vol. 11, no. 1, pp. 30–45, 2015.
- [96] D. Hu, D. Zhang, B. Liu et al., “Human ucMSCs seeded in a decellularized kidney scaffold attenuate renal fibrosis by reducing epithelial–mesenchymal transition via the TGF- $\beta$ /Smad signaling pathway,” *Pediatric Research*, vol. 88, no. 2, pp. 192–201, 2020.
- [97] T. M. Manalastas, N. Dugos, G. Ramos et al., “Effect of Decellularization Parameters on the Efficient Production of Kidney Bioscaffolds,” *Applied biochemistry and biotechnology*, vol. 193, no. 5, pp. 1239–1251, 2021.
- [98] S. Say, N. Dugos, S. Roces et al., “Sonication-assisted Perfusion Decellularization of Whole Porcine Kidney,” 2019.
- [99] A. A. Manfredi, A. Capobianco, M. E. Bianchi et al., “Regulation of dendritic- and T-cell fate by injury-associated endogenous signals,” *Critical reviews in immunology*, vol. 29, no. 1, pp. 69–86, 2009.
- [100] S. Nagata, R. Hanayama, and K. Kawane, “Autoimmunity and the clearance of dead cells,” *Cell*, vol. 140, no. 5, pp. 619–630, 2010.
- [101] B. N. Brown, J. E. Valentin, A. M. Stewart-Akers et al., “Macrophage phenotype and remodeling outcomes in response to biologic scaffolds with and without a cellular component,” *Biomaterials*, vol. 30, no. 8, pp. 1482–1491, 2009.
- [102] Q. Zhang, M. Raoof, Y. Chen et al., “Circulating mitochondrial DAMPs cause inflammatory responses to injury,” *Nature*, vol. 464, no. 7285, pp. 104–107, 2010.
- [103] F. K.-M. Chan, K. Moriwaki, and M. J. de Rosa, “Detection of necrosis by release of lactate dehydrogenase activity,” *Methods in molecular biology (Clifton, N.J.)*, vol. 979, pp. 65–70, 2013.

## 7 References

---

- [104] S. M. Smith, M. B. Wunder, D. A. Norris et al., “A Simple Protocol for Using a LDH-Based Cytotoxicity Assay to Assess the Effects of Death and Growth Inhibition at the Same Time,” *PloS one*, vol. 6, no. 11, e26908, 2011.
- [105] D. Lavogina, H. Lust, M.-J. Tahk et al., “Revisiting the Resazurin-Based Sensing of Cellular Viability: Widening the Application Horizon,” *Biosensors*, vol. 12, no. 4, 2022.
- [106] A. Limonciel, L. Aschauer, A. Wilmes et al., “Lactate is an ideal non-invasive marker for evaluating temporal alterations in cell stress and toxicity in repeat dose testing regimes,” *Toxicology in Vitro*, vol. 25, no. 8, pp. 1855–1862, 2011.
- [107] A. Rizki-Safitri, T. Traitteur, and R. Morizane, “Bioengineered Kidney Models: Methods and Functional Assessments,” *Function*, vol. 2, no. 4, zqab026, 2021.
- [108] S. Shahraki, M. Moghaddam Matin, A. Ebrahimzadeh Bideskan et al., “Kidney tissue engineering using a well-preserved acellular rat kidney scaffold and mesenchymal stem cells,” *Veterinary research forum : an international quarterly journal*, vol. 12, no. 3, pp. 339–348, 2021.
- [109] N. Poornejad, L. B. Schaumann, E. M. Buckmiller et al., “The impact of decellularization agents on renal tissue extracellular matrix,” *Journal of biomaterials applications*, vol. 31, no. 4, pp. 521–533, 2016.
- [110] I. Ullah, R. Abu-Dawud, J. F. Busch et al., “VEGF – Supplemented extracellular matrix is sufficient to induce endothelial differentiation of human iPSC,” *Biomaterials*, vol. 216, p. 119283, 2019.
- [111] D. S. Masson-Meyers and L. Tayebi, “Vascularization strategies in tissue engineering approaches for soft tissue repair,” *Journal of tissue engineering and regenerative medicine*, vol. 15, no. 9, pp. 747–762, 2021.
- [112] H. Yu, S. K. Chong, A. M. Hassanbhai et al., “Chapter 11 - Principles of bioreactor design for tissue engineering,” in *Principles of Tissue Engineering (Fifth Edition)*, R. Lanza, R. Langer, J. P. Vacanti et al., Eds., pp. 179–203, Academic Press, 2020.
- [113] D. Lim, E. S. Renteria, D. S. Sime et al., “Bioreactor design and validation for manufacturing strategies in tissue engineering,” *Bio-Design and Manufacturing*, vol. 5, no. 1, pp. 43–63, 2022.
- [114] M. Montorsi, G. G. Genchi, D. de Pasquale et al., “Design, fabrication, and characterization of a multimodal reconfigurable bioreactor for bone tissue engineering,” *Biotechnology and Bioengineering*, vol. 119, no. 7, pp. 1965–1979, 2022.
- [115] A. J. Janvier, E. Canty-Laird, and J. R. Henstock, “A universal multi-platform 3D printed bioreactor chamber for tendon tissue engineering,” *Journal of tissue engineering*, vol. 11, 2041731420942462, 2020.

## 7 References

---

- [116] S. Todros, S. Spadoni, E. Maghin et al., “A Novel Bioreactor for the Mechanical Stimulation of Clinically Relevant Scaffolds for Muscle Tissue Engineering Purposes,” *Processes*, vol. 9, no. 3, 2021.
- [117] G. Putame, S. Gabetti, D. Carbonaro et al., “Compact and tunable stretch bioreactor advancing tissue engineering implementation. Application to engineered cardiac constructs,” *Medical Engineering & Physics*, vol. 84, pp. 1–9, 2020.
- [118] J. H. Kim, A. Atala, and J. J. Yoo, “Chapter 45 - Tissue engineering of the kidney,” in *Principles of Tissue Engineering (Fifth Edition)*, R. Lanza, R. Langer, J. P. Vacanti et al., Eds., pp. 825–843, Academic Press, 2020.
- [119] J. J. Song, J. P. Guyette, S. E. Gilpin et al., “Regeneration and experimental orthotopic transplantation of a bioengineered kidney,” *Nature Medicine*, vol. 19, no. 5, pp. 646–651, 2013.
- [120] S. Sabetkish and A.-M. Kajbafzadeh, “The Renal Extracellular Matrix as a Supportive Scaffold for Kidney Tissue Engineering: Progress and Future Considerations,” in *Decellularization Methods of Tissue and Whole Organ in Tissue Engineering*, A.-M. Kajbafzadeh, Ed., pp. 103–118, Springer International Publishing, Cham, 2021.
- [121] “Adult Tissue Extracellular Matrix Determines Tissue Specification of Human iPSC-Derived Embryonic Stage Mesodermal Precursor Cells,” vol. 7, no. 5.
- [122] O. Ciampi, B. Bonandrini, M. Derosas et al., “Engineering the vasculature of decellularized rat kidney scaffolds using human induced pluripotent stem cell-derived endothelial cells,” *Scientific Reports*, vol. 9, no. 1, p. 8001, 2019.
- [123] M. Lorenz, F. Poosch, M. Meyer et al., “Ultrasonic treatment for decellularisation of cartilage and dura mater,” *euspen’s 21st International Conference & Exhibition, Copenhagen, 2021*.
- [124] M. Caralt, J. S. Uzarski, S. Iacob et al., “Optimization and critical evaluation of decellularization strategies to develop renal extracellular matrix scaffolds as biological templates for organ engineering and transplantation,” *American Journal of Transplantation*, vol. 15, no. 1, pp. 64–75, 2015.
- [125] H. Liu, Y. Xu, S. Zu et al., “Effects of High Hydrostatic Pressure on the Conformational Structure and Gel Properties of Myofibrillar Protein and Meat Quality: A Review,” *Foods*, vol. 10, no. 8, 2021.
- [126] F. A. de Oliveira, O. C. Neto, Santos, Lígia Marcondes Rodrigues dos et al., “Effect of high pressure on fish meat quality – A review,” *Trends in Food Science & Technology*, vol. 66, pp. 1–19, 2017.

## 7 References

---

- [127] R. Ramírez, A. Trejo, J. Delgado-Adámez et al., “Effect of High-Hydrostatic-Pressure Processing and Storage Temperature on Sliced Iberian Dry-Cured Sausage (&ldquo;Salchich&ocute;n&rdquo;) from Pigs Reared in Montanera System,” *Foods*, vol. 11, no. 9, 2022.
- [128] J. Hwang, B. H. San, N. J. Turner et al., “Molecular assessment of collagen denaturation in decellularized tissues using a collagen hybridizing peptide,” *Acta Biomaterialia*, vol. 53, pp. 268–278, 2017.
- [129] J. Zhao, W. Yu, Q. Zhang et al., “Structural and biofunctional evaluation of decellularized jellyfish matrices,” *Journal of Materials Chemistry B*, vol. 11, no. 16, pp. 3740–3751, 2023.
- [130] D. M. Serena, F. Giovanna, and M. Paola, “Rheological Characterization Bovine Serum Albumin Gels Induced by High Hydrostatic Pressure,” *Food and Nutrition Sciences*, Vol.06No.09, p. 10, 2015.
- [131] J. L. Silva, A. C. Oliveira, Vieira, Tuane C. R. G. et al., “High-Pressure Chemical Biology and Biotechnology,” *Chemical Reviews*, vol. 114, no. 14, pp. 7239–7267, 2014.
- [132] H. Salti, L. Kramer, S.-C. Nelz et al., “Decellularization of precision-cut kidney slices-application of physical and chemical methods,” *Biomedical materials (Bristol, England)*, vol. 18, no. 2, 2023.
- [133] A. Gilpin, Y. Yang, and C. Del Gaudio, “Decellularization Strategies for Regenerative Medicine: From Processing Techniques to Applications,” *BioMed Research International*, vol. 2017, p. 9831534, 2017.
- [134] S. Shahraki, A. E. Bideskan, M. Aslzare et al., “Decellularization with triton X-100 provides a suitable model for human kidney bioengineering using human mesenchymal stem cells,” *Life sciences*, vol. 295, p. 120167, 2022.
- [135] S. Sasaki, S. Funamoto, Y. Hashimoto et al., “In vivo evaluation of a novel scaffold for artificial corneas prepared by using ultrahigh hydrostatic pressure to decellularize porcine corneas,” *Molecular vision*, vol. 15, pp. 2022–2028, 2009.
- [136] CheftelJC., “Effects of high hydrostatic pressure on food constituents an overview,” *Balny, C, Et Al (Ed ) Colloque Inserm (Institut National De La Sante Et De La Recherche Medicale)*, Vol, 224 Haute Pression Et Biotechnologie; (Inserm (National Institute Of Health And Medical Research) Colloquium, Vol 224 High Pressure And Biotechnology); First European Seminar on High Pressure And Biotechnology Held Jointly With The Fifth Symposium on High Pressure And Food Scie, Ed, ontrouge, 1992.
- [137] D. Zemmyo, M. Yamamoto, and S. Miyata, “Efficient Decellularization by Application of Moderate High Hydrostatic Pressure with Supercooling Pretreatment,” *Micromachines*, vol. 12, no. 12, 2021.

- [138] E. Vorobiev and N. Lebovka, "Cooling, Freezing, Thawing and Crystallization," in *Processing of Foods and Biomass Feedstocks by Pulsed Electric Energy*, E. Vorobiev and N. Lebovka, Eds., pp. 179–207, Springer International Publishing, Cham, 2020.
- [139] N. İ. Büyük, K. Tüfekçi, A. Cumbul et al., "A novel method for providing scaffold: Decellularization of parathyroid capsule," *Journal of biomaterials applications*, vol. 36, no. 7, pp. 1201–1212, 2021.
- [140] M. Parmaksız, A. E. Elcin, and Y. M. Elcin, "Decellularization of bovine small intestinal submucosa and its use for the healing of a critical-sized full-thickness skin defect, alone and in combination with stem cells, in a small rodent model," *Journal of tissue engineering and regenerative medicine*, vol. 11, no. 6, pp. 1754–1765, 2017.
- [141] N. Li, Y. Li, D. Gong et al., "Efficient decellularization for bovine pericardium with extracellular matrix preservation and good biocompatibility," *Interactive CardioVascular and Thoracic Surgery*, vol. 26, no. 5, pp. 768–776, 2018.
- [142] F. Yusof, M. Sha'ban, and A. Azhim, "Development of decellularized meniscus using closed sonication treatment system: potential scaffolds for orthopedics tissue engineering applications," *International journal of nanomedicine*, vol. 14, pp. 5491–5502, 2019.
- [143] S. Say, N. Dugos, S. Roces et al., "Sonication-assisted Perfusion Decellularization of Whole Porcine Kidney," 2019.
- [144] M. He, A. Callanan, K. Lagaras et al., "Optimization of SDS exposure on preservation of ECM characteristics in whole organ decellularization of rat kidneys," *Journal of biomedical materials research. Part B, Applied biomaterials*, vol. 105, no. 6, pp. 1352–1360, 2017.
- [145] "Ions, the Movement of Water and the Apoptotic Volume Decrease,"
- [146] Q. Wu, J. Bao, Y. Zhou et al., "Optimizing Perfusion-Decellularization Methods of Porcine Livers for Clinical-Scale Whole-Organ Bioengineering," *BioMed Research International*, vol. 2015, p. 785474, 2015.
- [147] J. J. Urbano, R. K. da Palma, F. M. de Lima et al., "Effects of two different decellularization routes on the mechanical properties of decellularized lungs," *PloS one*, vol. 12, no. 6, e0178696, 2017.
- [148] H. Kitahara, H. Yagi, K. Tajima et al., "Heterotopic transplantation of a decellularized and recellularized whole porcine heart," *Interactive CardioVascular and Thoracic Surgery*, vol. 22, no. 5, pp. 571–579, 2016.
- [149] V. K. Kuna, N. Kvarnström, E. Elebring et al., "Isolation and Decellularization of a Whole Porcine Pancreas," *JoVE*, no. 140, e58302, 2018.

## 7 References

---

- [150] G. Mazza, K. Rombouts, A. Rennie Hall et al., “Decellularized human liver as a natural 3D-scaffold for liver bioengineering and transplantation,” *Scientific Reports*, vol. 5, no. 1, p. 13079, 2015.
- [151] C. Quint, Y. Kondo, R. J. Manson et al., “Decellularized tissue-engineered blood vessel as an arterial conduit,” *Proceedings of the National Academy of Sciences of the United States of America*, vol. 108, no. 22, pp. 9214–9219, 2011.
- [152] J. Willemse, M. M. Verstegen, A. Vermeulen et al., “Fast, robust and effective decellularization of whole human livers using mild detergents and pressure controlled perfusion,” *Materials science & engineering. C, Materials for biological applications*, vol. 108, p. 110200, 2020.
- [153] “Utility of Air Bladder-Derived Nanostructured ECM for Tissue Regeneration,”
- [154] R. Tamburrini, D. Chaimov, A. Asthana et al., “Detergent-Free Decellularization of the Human Pancreas for Soluble Extracellular Matrix (ECM) Production,” *JoVE*, no. 163, 2020.
- [155] S. Geerts, S. Ozer, M. Jaramillo et al., “Nondestructive Methods for Monitoring Cell Removal During Rat Liver Decellularization,” *Tissue Engineering Part C: Methods*, vol. 22, no. 7, pp. 671–678, 2016.
- [156] G. I. Barbulescu, F. M. Bojin, V. L. Ordodi et al., “Innovative Biotechnology for Generation of Cardiac Tissue,” *Applied Sciences*, vol. 11, no. 12, 2021.
- [157] B. Hammouda, “Temperature Effect on the Nanostructure of SDS Micelles in Water,” *Journal of research of the National Institute of Standards and Technology*, vol. 118, pp. 151–167, 2013.
- [158] J. Sauter, H. Degenhardt, J. Tuebel et al., “Effect of different decellularization protocols on reendothelialization with human cells for a perfused renal bioscaffold of the rat,” *BMC Biotechnology*, vol. 23, no. 1, p. 8, 2023.
- [159] P. R. Corridon, “In vitro investigation of the impact of pulsatile blood flow on the vascular architecture of decellularized porcine kidneys,” *Scientific Reports*, vol. 11, no. 1, p. 16965, 2021.
- [160] J. Hülsmann, H. Aubin, S. T. Bandesha et al., “Rheology of perfusates and fluid dynamical effects during whole organ decellularization: a perspective to individualize decellularization protocols for single organs,” *Biofabrication*, vol. 7, no. 3, p. 35008, 2015.
- [161] C. Hochman-Mendez, Pereira de Campos, Dilza Balteiro, R. S. Pinto et al., “Tissue-engineered human embryonic stem cell-containing cardiac patches: evaluating recellularization of decellularized matrix,” *Journal of tissue engineering*, vol. 11, 2041731420921482, 2020.
- [162] P.-F. Lee, E. Chau, R. Cabello et al., “Inverted orientation improves decellularization of whole porcine hearts,” *Acta Biomaterialia*, vol. 49, pp. 181–191, 2017.

## 7 References

---

- [163] D. Zuncheddu, E. Della Bella, A. Schwab et al., “Quality control methods in musculoskeletal tissue engineering: from imaging to biosensors,” *Bone Research*, vol. 9, no. 1, p. 46, 2021.
- [164] “Raman Spectroscopy in Skeletal Tissue Disorders and Tissue Engineering: Present and Prospective,” *Tissue Engineering Part B: Reviews*, vol. 28, no. 5, pp. 949–965, 2022.
- [165] R. K. da Palma, N. Campillo, J. J. Uriarte et al., “Pressure- and flow-controlled media perfusion differently modify vascular mechanics in lung decellularization,” *Journal of the mechanical behavior of biomedical materials*, vol. 49, pp. 69–79, 2015.
- [166] A. Remuzzi, M. Figliuzzi, B. Bonandrini et al., “Experimental Evaluation of Kidney Regeneration by Organ Scaffold Recellularization,” *Scientific Reports*, vol. 7, p. 43502, 2017.
- [167] F. Ghorbani, M. Ekhtiari, B. Moeini Chaghervand et al., “Detection of the residual concentration of sodium dodecyl sulfate in the decellularized whole rabbit kidney extracellular matrix,” *Cell and Tissue Banking*, vol. 23, no. 1, pp. 119–128, 2022.
- [168] R. M. Bell, M. M. Mocanu, and D. M. Yellon, “Retrograde heart perfusion: the Langendorff technique of isolated heart perfusion,” *Journal of molecular and cellular cardiology*, vol. 50, no. 6, pp. 940–950, 2011.
- [169] E. D. Girard, T. J. Jensen, S. D. Vadasz et al., “Automated procedure for biomimetic de-cellularized lung scaffold supporting alveolar epithelial transdifferentiation,” *Biomaterials*, vol. 34, no. 38, pp. 10043–10055, 2013.
- [170] D. G. Leuning, F. M. Witjas, M. Maanaoui et al., “Vascular bioengineering of scaffolds derived from human discarded transplant kidneys using human pluripotent stem cell–derived endothelium,” *American Journal of Transplantation*, vol. 19, no. 5, pp. 1328–1343, 2019.
- [171] J. Yang, Y. Xu, S. Luo et al., “Effect of cryoprotectants on rat kidney decellularization by freeze-thaw process,” *Cryobiology*, vol. 105, pp. 71–82, 2022.
- [172] B. Bonandrini, M. Figliuzzi, E. Papadimou et al., “Recellularization of well-preserved acellular kidney scaffold using embryonic stem cells,” *Tissue engineering. Part A*, vol. 20, 9-10, pp. 1486–1498, 2014.
- [173] K. H. Hussein, T. Saleh, E. Ahmed et al., “Biocompatibility and hemocompatibility of efficiently decellularized whole porcine kidney for tissue engineering,” *Journal of biomedical materials research. Part A*, vol. 106, no. 7, pp. 2034–2047, 2018.
- [174] D. Li and Y. Wang, “Chapter 14 - Mechanobiology, tissue development, and tissue engineering,” in *Principles of Tissue Engineering (Fifth Edition)*, R. Lanza, R. Langer, J. P. Vacanti et al., Eds., pp. 237–256, Academic Press, 2020.

## 7 References

---

- [175] C. de Pascalis and S. Etienne-Manneville, "Single and collective cell migration: the mechanics of adhesions," *Molecular biology of the cell*, vol. 28, no. 14, pp. 1833–1846, 2017.
- [176] S. S. Lou, A. S. Kennard, E. F. Koslover et al., "Elastic wrinkling of keratocyte lamellipodia driven by myosin-induced contractile stress," *Biophysical Journal*, vol. 120, no. 9, pp. 1578–1591, 2021.
- [177] S. Fujiwara, S. Deguchi, and T. M. Magin, "Disease-associated keratin mutations reduce traction forces and compromise adhesion and collective migration," *Journal of Cell Science*, vol. 133, no. 14, jcs243956, 2020.
- [178] J. Dou, S. Mao, H. Li et al., "Combination Stiffness Gradient with Chemical Stimulation Directs Glioma Cell Migration on a Microfluidic Chip," *Analytical Chemistry*, vol. 92, no. 1, pp. 892–898, 2020.
- [179] S. R. Caliri and J. A. Burdick, "A practical guide to hydrogels for cell culture," *Nature Methods*, vol. 13, no. 5, pp. 405–414, 2016.
- [180] T. Yeung, P. C. Georges, L. A. Flanagan et al., "Effects of substrate stiffness on cell morphology, cytoskeletal structure, and adhesion," *Cell Motility*, vol. 60, no. 1, pp. 24–34, 2005.
- [181] F. G. Aoki, R. Varma, A. E. Marin-Araujo et al., "De-epithelialization of porcine tracheal allografts as an approach for tracheal tissue engineering," *Scientific Reports*, vol. 9, no. 1, p. 12034, 2019.
- [182] F. Sensi, E. D'angelo, A. Biccari et al., "Establishment of a human 3D pancreatic adenocarcinoma model based on a patient-derived extracellular matrix scaffold," *Translational Research*, vol. 253, pp. 57–67, 2023.
- [183] B. Young, L.-A. M. Antczak, K. Shankar et al., "A Two-Step Bioreactor for Lung Recellularization," *bioRxiv*, 2020.
- [184] M. Parmaksiz, Ö. Lalegül-Ülker, M. T. Vurat et al., "Magneto-sensitive decellularized bone matrix with or without low frequency-pulsed electromagnetic field exposure for the healing of a critical-size bone defect," *Materials science & engineering. C, Materials for biological applications*, vol. 124, p. 112065, 2021.
- [185] W. Wang, G. Caetano, W. S. Ambler et al., "Enhancing the Hydrophilicity and Cell Attachment of 3D Printed PCL/Graphene Scaffolds for Bone Tissue Engineering," *Materials*, vol. 9, no. 12, 2016.
- [186] H. T. Beaman and M. B. Monroe, "Highly porous gas-blown hydrogels for direct cell encapsulation with high cell viability," *Tissue engineering. Part A*, 2023.

## 7 References

---

- [187] J. S. Uzarski, B. M. Bijonowski, B. Wang et al., “Dual-Purpose Bioreactors to Monitor Noninvasive Physical and Biochemical Markers of Kidney and Liver Scaffold Recellularization,” *Tissue Engineering Part C: Methods*, vol. 21, no. 10, pp. 1032–1043, 2015.
- [188] A. Limonciel, A. Wilmes, L. Aschauer et al., “Oxidative stress induced by potassium bromate exposure results in altered tight junction protein expression in renal proximal tubule cells,” *Archives of Toxicology*, vol. 86, no. 11, pp. 1741–1751, 2012.
- [189] C. Tebby, W. Gao, J. Delp et al., “A quantitative AOP of mitochondrial toxicity based on data from three cell lines,” *Toxicology in Vitro*, vol. 81, p. 105345, 2022.
- [190] L. Aschauer, A. Limonciel, A. Wilmes et al., “Application of RPTEC/TERT1 cells for investigation of repeat dose nephrotoxicity: A transcriptomic study,” *Toxicology in Vitro*, vol. 30, 1, Part A, pp. 106–116, 2015.
- [191] M. Caralt, J. S. Uzarski, S. Iacob et al., “Optimization and Critical Evaluation of Decellularization Strategies to Develop Renal Extracellular Matrix Scaffolds as Biological Templates for Organ Engineering and Transplantation,” *American Journal of Transplantation*, vol. 15, no. 1, pp. 64–75, 2015.
- [192] D.-J. Yoo, “Advanced porous scaffold design using multi-void triply periodic minimal surface models with high surface area to volume ratios,” *International Journal of Precision Engineering and Manufacturing*, vol. 15, no. 8, pp. 1657–1666, 2014.
- [193] C. Magliaro, G. Mattei, F. Iacoangeli et al., “Oxygen Consumption Characteristics in 3D Constructs Depend on Cell Density,” *Frontiers in bioengineering and biotechnology*, vol. 7, p. 251, 2019.
- [194] I. Streeter and U. Cheema, “Oxygen consumption rate of cells in 3D culture: the use of experiment and simulation to measure kinetic parameters and optimise culture conditions,” *The Analyst*, vol. 136, no. 19, pp. 4013–4019, 2011.
- [195] P. Rybkowska, K. Radoszkiewicz, M. Kawalec et al., “The Metabolic Changes between Monolayer (2D) and Three-Dimensional (3D) Culture Conditions in Human Mesenchymal Stem/Stromal Cells Derived from Adipose Tissue,” *Cells*, vol. 12, no. 1, 2023.
- [196] R. Bhatt, D. Ravi, A. M. Evens et al., “Scaffold-mediated switching of lymphoma metabolism in culture,” *Cancer & Metabolism*, vol. 10, no. 1, p. 15, 2022.
- [197] K. Linke, J. Schanz, J. Hansmann et al., “Engineered Liver-Like Tissue on a Capillarized Matrix for Applied Research,” *Tissue Engineering*, vol. 13, no. 11, pp. 2699–2707, 2007.

## 7 References

---

- [198] X. Ren, L. F. Tapias, B. J. Jank et al., “Ex vivo non-invasive assessment of cell viability and proliferation in bio-engineered whole organ constructs,” *Biomaterials*, vol. 52, pp. 103–112, 2015.
- [199] M. Radisic, J. Malda, E. Epping et al., “Oxygen gradients correlate with cell density and cell viability in engineered cardiac tissue,” *Biotechnology and Bioengineering*, vol. 93, no. 2, pp. 332–343, 2006.
- [200] P. F. Secker, L. Luks, N. Schlichenmaier et al., “RPTEC/TERT1 cells form highly differentiated tubules when cultured in a 3D matrix,” *ALTEX - Alternatives to animal experimentation*, vol. 35, no. 2, pp. 223–234, 2018.
- [201] Y. H. Shen, M. S. Shoichet, and M. Radisic, “Vascular endothelial growth factor immobilized in collagen scaffold promotes penetration and proliferation of endothelial cells,” *Acta Biomaterialia*, vol. 4, no. 3, pp. 477–489, 2008.
- [202] C. Jensen and Y. Teng, “Is It Time to Start Transitioning From 2D to 3D Cell Culture?,” *Frontiers in molecular biosciences*, vol. 7, p. 33, 2020.
- [203] K. Duval, H. Grover, L.-H. Han et al., “Modeling Physiological Events in 2D vs. 3D Cell Culture,” *Physiology (Bethesda, Md.)*, vol. 32, no. 4, pp. 266–277, 2017.
- [204] M. A. Odenwald, W. Choi, A. Buckley et al., “ZO-1 interactions with F-actin and occludin direct epithelial polarization and single lumen specification in 3D culture,” *Journal of Cell Science*, vol. 130, no. 1, pp. 243–259, 2017.
- [205] A. Kirk, S. Campbell, P. Bass et al., “Differential expression of claudin tight junction proteins in the human cortical nephron,” *Nephrology, dialysis, transplantation : official publication of the European Dialysis and Transplant Association - European Renal Association*, vol. 25, no. 7, pp. 2107–2119, 2010.
- [206] W.-T. Kuo, M. A. Odenwald, J. R. Turner et al., “Tight junction proteins occludin and ZO-1 as regulators of epithelial proliferation and survival,” *Annals of the New York Academy of Sciences*, vol. 1514, no. 1, pp. 21–33, 2022.
- [207] Cooper GM, *The Cell: A Molecular Approach: Cell Proliferation in Development and Differentiation*, Sinauer Associates, Sunderland (MA), 2000.
- [208] S. Ruijtenberg and S. van den Heuvel, “Coordinating cell proliferation and differentiation: Antagonism between cell cycle regulators and cell type-specific gene expression,” *Cell Cycle*, vol. 15, no. 2, pp. 196–212, 2016.

## 7 References

---

- [209] E. J. Ross, E. R. Gordon, H. Sothers et al., “Three dimensional modeling of biologically relevant fluid shear stress in human renal tubule cells mimics in vivo transcriptional profiles,” *Scientific Reports*, vol. 11, no. 1, p. 14053, 2021.
- [210] A. L. Olivares and D. Lacroix, “Simulation of Cell Seeding Within a Three-Dimensional Porous Scaffold: A Fluid-Particle Analysis,” *Tissue Engineering Part C: Methods*, vol. 18, no. 8, pp. 624–631, 2012.
- [211] Z. Liu, M. Tamaddon, Y. Gu et al., “Cell Seeding Process Experiment and Simulation on Three-Dimensional Polyhedron and Cross-Link Design Scaffolds,” *Frontiers in bioengineering and biotechnology*, vol. 8, p. 104, 2020.
- [212] S. Ni, J. Chang, and L. Chou, “A novel bioactive porous CaSiO<sub>3</sub> scaffold for bone tissue engineering,” *Journal of biomedical materials research. Part A*, 76A, no. 1, pp. 196–205, 2006.
- [213] Y. Tang, Y. Zhou, G. Lin et al., “Enhanced Cell Penetration and Pluripotency Maintenance of hiPSCs in 3D Natural Chitosan Scaffolds,” *Macromolecular Bioscience*, vol. 23, no. 6, p. 2200460, 2023.
- [214] S.-C. Nelz, *Development of Recellularization Methods for Rat Kidney Scaffolds*, Rostock University Medical Center, 2021.
- [215] A. Shellard and R. Mayor, “All Roads Lead to Directional Cell Migration,” *Trends in Cell Biology*, vol. 30, no. 11, pp. 852–868, 2020.
- [216] M. J. Oudin, M. A. Miller, J. A. Z. Klazen et al., “MenalNV mediates synergistic cross-talk between signaling pathways driving chemotaxis and haptotaxis,” *Molecular biology of the cell*, vol. 27, no. 20, pp. 3085–3094, 2016.
- [217] Z. Roveimiab, F. Lin, and J. E. Anderson, “Traction and attraction: haptotaxis substrates collagen and fibronectin interact with chemotaxis by HGF to regulate myoblast migration in a microfluidic device,” *American journal of physiology. Cell physiology*, vol. 319, no. 1, C75-C92, 2020.
- [218] X. Luo, V. Seveau de Noray, L. Aoun et al., “Lymphocytes perform reverse adhesive haptotaxis mediated by LFA-1 integrins,” *Journal of Cell Science*, vol. 133, no. 16, 2020.
- [219] J. H. Wen, O. Choi, H. Taylor-Weiner et al., “Haptotaxis is Cell Type Specific and Limited by Substrate Adhesiveness,” *Cellular and Molecular Bioengineering*, vol. 8, no. 4, pp. 530–542, 2015.
- [220] C. M. Motta, K. J. Endres, C. Wesdemiotis et al., “Enhancing Schwann cell migration using concentration gradients of laminin-derived peptides,” *Biomaterials*, vol. 218, p. 119335, 2019.
- [221] “Neuro-taxis: Neuronal movement in gradients of chemical and physical environments,” vol. 80, 9-10.

- [222] “Selective Adhesion and Directional Migration of Endothelial Cells Guided by Cys-Ala-Gly Peptide Density Gradient on Antifouling Polymer Brushes,” vol. 19, no. 11.
- [223] M. Weber, R. Hauschild, J. Schwarz et al., “Interstitial dendritic cell guidance by haptotactic chemokine gradients,” *Science (New York, N.Y.)*, vol. 339, no. 6117, pp. 328–332, 2013.
- [224] R. Kalluri, “Basement membranes: structure, assembly and role in tumour angiogenesis,” *Nature Reviews Cancer*, vol. 3, no. 6, pp. 422–433, 2003.
- [225] S. Krishnamoorthy, Z. Zhang, and C. Xu, “Guided cell migration on a graded micropillar substrate,” *Bio-Design and Manufacturing*, vol. 3, no. 1, pp. 60–70, 2020.
- [226] J. Park, D.-H. Kim, H.-N. Kim et al., “Directed migration of cancer cells guided by the graded texture of the underlying matrix,” *Nature Materials*, vol. 15, no. 7, pp. 792–801, 2016.
- [227] J. C. Mateus, C. D. F. Lopes, M. Cerquido et al., “Improved in vitro electrophysiology using 3D-structured microelectrode arrays with a micro-mushrooms islets architecture capable of promoting topotaxis,” *Journal of neural engineering*, vol. 16, no. 3, p. 36012, 2019.
- [228] C. Leclech, D. Gonzalez-Rodriguez, A. Villedieu et al., “Topography-induced large-scale anti-parallel collective migration in vascular endothelium,” *Nature Communications*, vol. 13, no. 1, p. 2797, 2022.
- [229] “Biomimetic Multiscale Hierarchical Topography Enhances Osteogenic Differentiation of Human Mesenchymal Stem Cells,” vol. 7, no. 14.
- [230] C. Fedele, E. Mäntylä, B. Belardi et al., “Azobenzene-based sinusoidal surface topography drives focal adhesion confinement and guides collective migration of epithelial cells,” *Scientific Reports*, vol. 10, no. 1, p. 15329, 2020.
- [231] D.-H. Kim, K. Han, K. Gupta et al., “Mechanosensitivity of fibroblast cell shape and movement to anisotropic substratum topography gradients,” *Biomaterials*, vol. 30, no. 29, pp. 5433–5444, 2009.
- [232] A. Tinari, A. M. Giammarioli, V. Manganelli et al., “Chapter One Analyzing Morphological and Ultrastructural Features in Cell Death,” in *Methods in Enzymology : Programmed Cell Death, General Principles for Studying Cell Death, Part A*, vol. 442, pp. 1–26, Academic Press, 2008.
- [233] S. H. Ross and D. A. Cantrell, “Signaling and Function of Interleukin-2 in T Lymphocytes,” *Annual review of immunology*, vol. 36, pp. 411–433, 2018.
- [234] K. H. Hussein, K. M. Park, H. M. Kim et al., “Construction of a biocompatible decellularized porcine hepatic lobe for liver bioengineering,” *The International journal of artificial organs*, vol. 38, no. 2, pp. 96–104, 2015.

## 7 References

---

- [235] N. Alvarez-Rueda, C. Rouges, A. Touahri et al., “In vitro immune responses of human PBMCs against *Candida albicans* reveals fungal and leucocyte phenotypes associated with fungal persistence,” *Scientific Reports*, vol. 10, no. 1, p. 6211, 2020.
- [236] J. G. Melgaço, T. Azamor, A. M. V. Silva et al., “Two-Step In Vitro Model to Evaluate the Cellular Immune Response to SARS-CoV-2,” *Cells*, vol. 10, no. 9, 2021.
- [237] N. Kränkel, K. Kuschnerus, P. Madeddu et al., “A novel flow cytometry-based assay to study leukocyte–endothelial cell interactions in vitro,” *Cytometry Part A*, 79A, no. 4, pp. 256–262, 2011.
- [238] F. Piossek, S. Beneke, N. Schlichenmaier et al., “Physiological oxygen and co-culture with human fibroblasts facilitate in vivo-like properties in human renal proximal tubular epithelial cells,” *Chemico-Biological Interactions*, vol. 361, p. 109959, 2022.
- [239] M. Choi, Y.-B. Yang, S. Park et al., “Effect of Co-culture of mesenchymal stem cell and glomerulus endothelial cell to promote endothelialization under optimized perfusion flow rate in whole renal ECM scaffold,” *Materials today. Bio*, vol. 17, p. 100464, 2022.
- [240] T. Zhang, D. Lih, R. J. Nagao et al., “Open microfluidic coculture reveals paracrine signaling from human kidney epithelial cells promotes kidney specificity of endothelial cells,” *American journal of physiology. Renal physiology*, vol. 319, no. 1, F41-F51, 2020.

## 8 List of abbreviations

2D	Two dimensional
3D	Three dimensional
AKI	Acute kidney injury
ANN	Artificial neural networks
BC	Bowman Capsule
BM	Basement membrane
BSA	Bovine serum albumin
CKD	Chronic kidney disease
Col-IV	Collagen type IV
ECM	Extracellular matrix
EDTA	Ethylenediaminetetraacetic acid
ESC	Embryonic stem cells
ESRD	End-stage renal disease
FAC	Focal adhesion complex
F-CHP	fluorescently-labeled collagen hybridizing peptide
FTC	Freezing–thawing–cycles
GAG	Glycosaminoglycans
GBD	Global Burden of Disease
GBM	Glomerular basement membrane
GF	Growth factors
H&E	Hematoxylin and eosin
HHP	High hydrostatic pressure
IM	Interstitial matrix
iPSC	Induced pluripotent stem cells
IST	Insulin, transferrin, selenium
LDH	Lactate dehydrogenase
MSC	Mesenchymal stem cells
NCS	Non-cellular spaces
NGS	Normal goat serum
PBS	Phosphate-buffered saline
PBST	PBS-Tween
PCKS	Precision-cut kidney slices
PCT	Proximal convoluted tubule
PG	Proteoglycans
Prf	Perfusion
RPTEC/TERT1	Renal proximal tubular epithelial cells
RT	Room temperature
SDC	Sodium deoxycholate

---

SDS	Sodium dodecyl sulfate
SEM	Scanning electron microscopy
TBM	Tubular basement membrane
TE	Tissue engineering
UBS	Ultrasonic bath system
ZO-1	Zonula occludens-1

## 9 List of figures

Figure 1: Human kidney is divided into two main regions .....	4
Figure 2: Representation of the glomerular and tubular ECM components .....	5
Figure 3: Illustration of a focal adhesion complex in a cell .....	7
Figure 4: Schematic representation of the decellularization protocols .....	16
Figure 5: Schematic overview of the recellularization protocol for PCKS-Imm and PCKS-Prf .....	21
Figure 6: Schematic representation of the serial paraffin sections.....	24
Figure 7: Optical characteristics of PCKS following HHP treatment .....	28
Figure 8: Evaluation of NCS in H&E stained PCKS after HHP and FTC .....	30
Figure 9: Effect of physical methods and chemical reagents on collagen denaturation .....	31
Figure 10: Characterization of decellularized PCKS-Imm .....	33
Figure 11: Histological analysis of H&E stained native and PCKS-Imm .....	34
Figure 12: Scanning electron microscopy of native and PCKS-Imm decellularized by immersion.....	36
Figure 13: Immersion decellularization score .....	37
Figure 14: Characterization of native and decellularized whole rat kidneys .....	38
Figure 15: Evaluation of perfusate samples obtained during the decellularization process .....	40
Figure 16: Histological analysis with H&E for whole kidneys decellularized by perfusion .....	42
Figure 17: Scanning electron microscopy of whole kidneys decellularized by perfusion.....	43
Figure 18: Perfusion decellularization score.....	44
Figure 19: Macroscopic assessment of scaffold appearance after recellularization .....	44
Figure 20: Analysis of the cell culture medium of recellularized PCKS-Imm .....	46
Figure 21: Analysis of the cell culture medium of recellularized PCKS-Imm .....	48
Figure 22: Medium analysis score for PCKS-Imm scaffolds .....	49
Figure 23: Investigation of the migration depth of seeded cells within recellularized PCKS-Imm .....	50
Figure 24: Expression of ZO-1 in recellularized PCKS-Imm .....	51
Figure 25: Specificity of cell seeding in recellularized PCKS-Imm .....	52
Figure 26: Scaffold analysis score for PCKS-Imm scaffolds .....	53
Figure 27: Scanning electron microscopy of native and recellularized PCKS-Imm .....	54
Figure 28: Analysis of the cell culture medium of recellularized PCKS-Prf.....	56
Figure 29: Analysis of the cell culture medium of recellularized PCKS-Prf.....	57
Figure 30: Medium analysis score for PCK-Prf scaffolds .....	58
Figure 31: Investigation of the migration depth of seeded cells within recellularized PCKS-Prf.....	59
Figure 32: Expression of ZO-1 in recellularized PCKS-Prf.....	60
Figure 33: Specificity of cell seeding in recellularized PCKS-Prf .....	61
Figure 34: Scaffold analysis score for PCKS-Prf scaffolds .....	61
Figure 35: Scanning electron microscopy of recellularized PCKS-Prf .....	62
Figure 36: Recellularization score .....	63
Figure 37: Total score performance for all methods.....	64
Figure 38: Characterization of decellularized whole kidneys (direct and indirect approaches). .....	65

Figure 39: Analysis of H&E stained decellularized whole kidneys (direct & indirect approaches).....	66
Figure 40: Incubation of PBMCs with homogenized native and decellularized kidney scaffolds .....	67

## 10 List of supplementary figures

Figure S 1: Evaluation of histological categories of the scoring system for PCKS-Imm scaffolds.....	122
Figure S 2: Evaluation of histological categories of the scoring system for PCKS-Prf scaffolds .....	122
Figure S 3: Histological categories of the scoring system (direct and indirect approaches) .....	123
Figure S 4: Structure scores (histology category) of the scoring system for PCKS-Imm scaffolds .....	123
Figure S 5: Structure scores (histology category) of the scoring system for PCKS-Prf scaffolds .....	123
Figure S 6: Rat kidney harvest and preparation .....	124
Figure S 7: Illustration of the perfusion decellularization bioreactor setup .....	125
Figure S 8: Representative images of a whole rat kidney decellularized .....	126
Figure S 9: SEM of RPTEC/TERT1 cells in 2D (cover glass in 24 well plate) .....	126
Figure S 10: SEM of synthetic scaffolds (SYNTH) .....	127
Figure S 11: SEM of the ultrastructure of the luminal basal membrane .....	127
Figure S 12: Resazurin standard curve .....	128
Figure S 13: Representative images of ZO-1 staining on seeded SYNTH scaffolds .....	128
Figure S 14: Representative images of Col-IV staining on seeded SYNTH scaffolds. ....	129
Figure S 15: RPTEC/TERT1 cells in PCKS-Imm showing distinctive circular cell alignment .....	129
Figure S 16: Caco-2 (intestinal epithelial cells) in PCKS-Imm did not exhibit cellular alignments .....	130

## 11 List of supplementary tables

Table S 1: Materials for histology .....	114
Table S 2: Materials for animal preparation and kidney harvest .....	114
Table S 3: Materials for decellularization.....	115
Table S 4: Materials for the assessment of decellularization effectivity .....	115
Table S 5: Materials for recellularization .....	116
Table S 6: Materials for the assessment of recellularization .....	117
Table S 7: General instruments .....	117
Table S 8: Softwares .....	118
Table S 9: Number of replicates for applied assays in the immersion approach .....	118
Table S 10: Number of replicates for applied assays in the perfusion approach .....	118
Table S 11: Number of replicates in the direct and indirect decellularization approaches.....	119
Table S 12: Dehydration and tissue processing protocol.....	119
Table S 13: H&E staining protocol of paraffin sections .....	119
Table S 14: Dehydration and tissue processing protocol for decellularized kidneys .....	120
Table S 15: Categories of the scoring system and their respective parameters .....	121

## 12 Appendix

### 12.1 Materials

**Table S 1: Materials for histology**

<b>Name</b>	<b>Supplier</b>
<i>Chemicals</i>	
Formaldehyde methanol-free (30%)	Carl Roth, Germany
Ethanol	Carl Roth, Germany
Xylene (Isomers) > 98%, pure, for histology	Carl Roth, Germany
Mayer's Hemalum Solution	Carl Roth, Germany
Eosin 0.2% alcoholic	Merck, Germany
DePeX (Mounting medium)	Serva, Germany
Histoplast (Paraffin)	Epredia, Germany
<i>Instruments / consumables</i>	
Tissue processor, STP 120-2	Epredia, Germany
Tissue processor, ASP 3005 (for decellularized samples)	Leica, Germany
Embedding workstation, Histostar	Thermo Scientific, Germany
Microtome, MICROM 340 E	Thermo Scientific, Germany
Light microscope, DM IL LED	Leica Microsystems, Germany
Tissue cassettes	Thermo Scientific, Germany
HistoBond® microscope slides	Marienfeld, Germany

**Table S 2: Materials for animal preparation and kidney harvest**

<b>Name</b>	<b>Supplier</b>
<i>Rats</i>	
Sprague Dawley	Charles River, Germany
<i>Surgery</i>	
Isofluran CP 1 ml/ml	CP Pharma, Germany
Heparin-Natrium-5000	Ratiopharm, Germany
Cannulas, Vasofix® Safety, G 24	B. Braun SE, Germany
Phosphate buffered saline (10x)	Alfa Aesar, Germany
<i>Instruments</i>	
Anesthetic machine, Sulla 808	Dräger, Germany

Stereomicroscope, LEICA M651	Leica, Germany
Vibrating microtome (Vibratome, VT1200 S)	Leica, Germany
Ismatec ISM831C (2 channels pump)	Cole Parmer, Germany

**Table S 3: Materials for decellularization**

<b>Name</b>	<b>Supplier</b>
<i>Chemicals / buffers</i>	
Trypsin-EDTA, 0.05% (v/v) in DPBS	Carl Roth, Germany
Triton X-100	Capricorn, Germany
Sodium dodecyl sulfate (SDS)	Carl Roth, Germany
Deoxycholic acid sodium salt (SDC)	Carl Roth, Germany
Phosphate buffered saline (10x)	Alfa Aesar, Germany
<i>Instruments</i>	
Cold isotactic pressurization machine (HHP chamber)	Dustec Hochdrucktechnik, Germany
Sonication Bath	UCE Ultrasonic, Germany
Ismatec™ Reglo ICC (4 channels pump)	Cole-Parmer, Germany
Pump tube, Tygon® LMT-55, 2.54mm	VWR, Germany
Homogenizer, Precellys evolution	Bertin technologies, France
<i>Perfusion bioreactor</i>	
DURAN® baffled wide mouth bottle GLS 80	VWR, Germany
DURAN® replacement screw cap for GLS 80 stirred reactor	VWR, Germany
Laboratory screw joint GL 14, 4.0 mm	VWR, Germany
Screw cap, GL 14, red	VWR, Germany
Insert for screw cap GL 14 und GL 18	VWR, Germany
Screw cap with opening, GL14 und GL 18	VWR, Germany
Pump tube, Tygon® LMT-55, 2.54mm	VWR, Germany

**Table S 4: Materials for the assessment of decellularization effectivity**

<b>Name</b>	<b>Supplier</b>
<i>Kits</i>	
DNeasy Blood and Tissue Kit	Qiagen, Germany
Blyscan sulfated Glycosaminoglycan (GAG) Assay kit	Biocolor, Germany
Sircol Soluble Collagen Assay kit	Biocolor, Germany
<i>Chemicals</i>	
Papain from papaya latex (for GAG extraction)	Sigma-Aldrich, Germany

## 12 Appendix

Pepsin from porcine gastric mucosa (for collagen extraction)	Sigma-Aldrich, Germany
Acetic Acid (for pepsin solution)	VWR, Germany
Collagen Hybridizing Peptide, 5-FAM Conjugate (F-CHP)	3Helix, USA

### *Chemicals for papain solution (as in GAG assay kit manual)*

di-Sodium hydrogen phosphate	Carl Roth, Germany
Sodium dihydrogen phosphate monohydrate	Carl Roth, Germany
Sodium acetate	Carl Roth, Germany
Ethylenediaminetetraacetic acid (EDTA), di sodium salt	Carl Roth, Germany
Cysteine HCl	Carl Roth, Germany

### *Instruments*

NanoDrop Lite Spectrophotometer	Thermo Scientific, Germany
Microplate reader, Anthos 2010	Biochrom Ltd, UK
Nikon Eclipse Ti-E microscope	Nikon GmbH, Germany
Field emission scanning electron microscope, FE-SEM, MERLIN® VP Compact	Carl Zeiss, Germany

**Table S 5: Materials for recellularization**

<b>Name</b>	<b>Supplier</b>
<i>Cell line</i>	
immortalized human renal proximal tubular epithelial cells (RPTEC/TERT1)	ATCC, USA
<i>RPTEC/TERT1 cell culture medium</i>	
DMEM/F12 (1:1), w/o: L-Glutamine, w: 1.2 g/L NaHCO <sub>3</sub>	PAN Biotech, Germany
GlutaMax (100X)	Gibco, Germany
Fetal Bovine Serum	Capricorn, Germany
Epidermal growth factor	Sigma-Aldrich, Germany
Hydrocortisone	Sigma-Aldrich, Germany
Insulin-Transferrin-Selenium (100X)	Gibco, Germany
Penicillin/Streptomycin	Capricorn, Germany
<i>Synthetic scaffolds (SYNTH)</i>	
SeedEZ™ scaffold	Lena Biosciences, USA
<i>Chemicals / buffers / consumables</i>	
Trypsin-EDTA (0.05 % in DPBS)	Capricorn, Germany
Agarose Standard, Rotigarose	Carl Roth, Germany
Trypan blue solution (0.4%)	Thermo Scientific, Germany

## 12 Appendix

Dulbecco's PBS (1X)	Capricorn, Germany
Hemocytometer, C-Chip Hemocytometer	Nano EnTek, South Korea
<i>Instruments</i>	
CO <sub>2</sub> Incubator, BBD 6220	Thermo Scientific, Germany
Laminar flow hood, HeraSafe	Thermo Scientific, Germany

**Table S 6: Materials for the assessment of recellularization**

Name	Supplier
<i>Cell culture medium analysis (Assay kits)</i>	
Resazurin-sodium salt	Thermo Scientific, Germany
Lactae dehydrogenase kit LDH, IFCC	Labor + Technik Lehmann, Germany
Lactate kit, LOX-PAP	Labor + Technik Lehmann, Germany
Glucose kit, GOD-PAP	Labor + Technik Lehmann, Germany
<i>Scaffold analysis (antibodies and chemicals)</i>	
Rabbit anti-Collagen IV antibody (ab6586)	Abcam, Germany
Mouse anti ZO-1 monoclonal antibody (ZO1-1A12)	Thermo Scientific, Germany
Goat anti-Mouse secondary antibody, Alexa Fluor™ 647	Thermo Scientific, Germany
Goat anti-Rabbit secondary antibody, Alexa Fluor™ 647	Thermo Scientific, Germany
Normal Goat Serum (ab7481)	Abcam, Germany
Bovine serum albumin (BSA)	Carl Roth, Germany
Fluoromount-G™, with DAPI	Thermo Scientific, Germany
Tween 20	Carl Roth, Germany
<i>Instruments</i>	
Confocal microscope, Zeiss ELYRA PS. 1 LSM 780	Carl Zeiss, Germany
CLARIOstar plate reader	BMG LABTECH, Germany

**Table S 7: General instruments**

Name	Supplier
<i>General instruments</i>	
Centrifuge, Heraceus Megafuge 16R	Thermo Scientific, Germany
Thermomixer compact	Eppendorf, Germany
Stereomicroscope, Leica S9D	Leica, Germany

**Table S 8: Softwares**

Name	Developer
<i>Software</i>	
Image J, version 1.53J	National Institute of Health, USA
QuPath open source software for digital pathology image analysis, version 0.2.3	Centre for Cancer Research & Cell Biology, Queen's University Belfast, UK
Cellpose: generalist algorithm for cellular segmentation	HHMI, Ashburn, VA, USA
GraphPad Prism, version 6	GraphPad Software Inc., California, USA

## 12.2 Number of replicates

**Table S 9: Number of replicates for applied assays in the immersion approach**

Method	Resazurin			Lactate			Glucose			LDH					
	DNA	GAG	Collagen	D1	D2	D3	D1	D2	D3	D1	D2	D3	D1	D2	D3
Native	12	6	8	x	x	x	x	x	x	x	x	x	x	x	x
CHEM-Imm	4	4	5	4	5	5	5	5	5	5	5	5	4	4	4
HHP50-Imm	5	4	4	x	x	x	x	x	x	x	x	x	x	x	x
HHP100-Imm	4	4	3	x	x	x	x	x	x	x	x	x	x	x	x
HHP200-Imm	3	3	3	5	6	6	6	6	6	6	6	6	4	4	4
UBS30-Imm	3	3	3	x	x	x	x	x	x	x	x	x	x	x	x
UBS60-Imm	3	3	3	6	6	6	6	6	4	6	6	4	4	4	2
FTC-Imm	4	4	4	5	6	6	6	6	6	6	6	4	6	6	6
SYNTH	x	x	x	8	8	8	8	8	8	8	8	8	8	8	8
2D	x	x	x	12	12	12	11	11	11	11	11	11	11	11	11

**Table S 10: Number of replicates for applied assays in the perfusion approach. D1, D2 and D3 correspond to the incubation days at which the assays were performed**

Method	Resazurin			Lactate			Glucose			LDH					
	DNA	GAG	Collagen	D1	D2	D3	D1	D2	D3	D1	D2	D3	D1	D2	D3
Native	12	8	8	x	x	x	x	x	x	x	x	x	x	x	x
CHEM-Prf	7	7	7	6	5	5	6	5	5	6	5	5	6	5	5
HHP200-Prf	7	7	6	6	6	6	6	6	6	6	6	6	6	6	6
FTC-Prf	9	8	10	10	10	10	10	10	10	10	10	10	10	10	10

**Table S 11: Number of replicates in the direct and indirect decellularization approaches**

Method	DNA	GAG
Native	12	x
SDS1%	5	x
HHP100-SDS1%	5	x
FTC-SDS1%	4	4
SDS0.5%	5	5
HHP150-SDS0.5%	6	6
FTC-SDS0.5%	4	6

### 12.3 Histology protocols

**Table S 12: Dehydration and tissue processing protocol**

Step	Reagent	Duration (h)	Step	Reagent	Duration (h)
1	Ethanol 50%	2	6	Ethanol 100%	1
2	Ethanol 70%	2	7	Xylene	2
3	Ethanol 80%	1	8	Xylene	2
4	Ethanol 96%	1	9	Paraffin	2
5	Ethanol 100%	1	10	Paraffin	2

**Table S 13: H&E staining protocol of paraffin sections**

	Step	Reagent	Duration	Step	Reagent	Duration
deparaffinization	1	Xylene	5 min	8	Eosin 0.2% alcoholic	5 min
	2	Xylene	5 min	9	Washing: tap water	1 min
	3	Ethanol 96%	1 min	10	Ethanol 70%	5 s
	4	Ethanol 96%	1 min	11	Ethanol 96%	5 s
	5	Ethanol 70%	1 min	12	Ethanol 96%	5 s
	6	Mayers Hematoxylin	10 min	13	Xylene	5 s
	7	Washing: tap water	3 min	14	Xylene	5 s

**Table S 14: Dehydration and tissue processing protocol for decellularized kidneys**

Step	Reagent	Duration	Step	Reagent	Duration
1	Ethanol 70%	1 h	7	Ethanol 100%	1 h
2	Ethanol 70%	1 h	8	Isopropanol	1 h
3	Ethanol 80%	1 h	9	Xylene	1 h
4	Ethanol 96%	1 h	10	Xylene	1 h
5	Ethanol 96%	1 h	11	Paraffin	10 min
6	Ethanol 100%	1 h	12	Paraffin	10 min

## 12.4 Scoring system: calculation of the translated scores

Translated scores are calculated by multiplying the average maximal amount obtained from a respective assay with specific factors. Example: the average maximum amount of GAG obtained for the decellularization of PCKS-Imm is 1150 ng/mg dry tissue. A Score of 4 (which is the best attainable) is therefore given for a GAG content  $\geq 1150$  ng/mg. Lower scores were given to scaffolds with lower GAG contents. For the scores 1, 2 and 3, the maximum amount is multiplied with 0.6, 0.8 and 0.9, respectively. The scores for DNA content, however, were calculated by treating the DNA content oppositely (i.e. score of 4 for the lowest DNA content and lower scores for higher content). The same scoring system was applied for PCKS-Prf. However, whole decellularized kidneys obtained for the optimization of perfusion decellularization of HHP-treated kidneys (direct and indirect decellularization approached; section 3.4) were only subjected to histology scoring, excluding scaffolds shrinking measurement. No composition score was calculated for these scaffolds.

It should be emphasized that the immersion and perfusion methods were intentionally kept separate, with each decellularization approach being normalized against its own values. The PCKS model serves primarily as a testing and optimization platform for decellularization methods. In the context of transplantation, a whole kidney would be decellularized by perfusion, which is a fundamentally different process with distinct parameters.

**Table S 15: Categories of the scoring system and their respective parameters for the examination of de- and recellularized PCKS.** Scores were assigned from 1 to 4 signifying the best to worst achieved result. The max value refers to the highest achieved result for quantitative assays

Scores: 1-4, highest score = best result Score of 5 is assigned for the native kidney #: immersion values *: perfusion values				1	2	3	4	Max value #: immersion *: perfusion	
Total score	Decellularization score	Histology	General appearance	Remaining cytoplasmic material	cytoplasm minimally reduced (close to intact)	cytoplasm moderately reduced (no clear boundaries)	cytoplasm substantially removed, only fragments remaining	no cytoplasm remaining	
				Absence of nuclear structures	minimal loss of nuclei (close to intact)	moderate loss of nuclei, high amount of released DNA	substantial loss of nuclei, DNA detectable	no nuclei, no DNA detectable	
				Shrinking (remaining area) (quantified by ImageJ)	≤ 20%# / 18%*	≤ 41%# / 30%*	≤ 58%# / 38%*	65%# / 42%*	65%# / 42%*
		Structures	Glomeruli, tubules and vessels	complete disruption and breakdown of tissue (no outlines visible)	marked disruption of architecture (visible outlines)	moderate disruption of architecture (visible outlines)	minimal disruption, architecture close to intact		
	DNA and ECM Composition (ng/mg)	DNA content	≥ 1214# / 3497*	≥ 1093# / 3147*	≥ 765# / 2158*	≥ 382# / 1511*	1214# / 3497*		
		GAG content	≤ 3177# / 1035*	≤ 5296# / 1725*	≤ 6620# / 2156*	≤ 7355# / 2396*	7355# / 2396*		
		Collagen content	≤ 1660# / 1778*	≤ 2767# / 2964*	≤ 3458# / 3705*	≤ 3842# / 4116*	3842# / 4116*		
	Recellularization score	Medium analysis	Resazurin (RFU)	≤ 28,187# / 15,259*	≤ 46,978# / 25,431*	≤ 58,722# / 31,789*	≤ 65,247# / 35,321*	65,247# / 35,321*	
			LDH (U/l)	≥ 22# / 12*	≥ 19# / 11*	≥ 16# / 9*	≥ 9# / 5*	22# / 12*	
			Ratio (LAC/GLU)	≥ 0.83# / 0.75*	≥ 0.75# / 0.68*	≥ 0.60# / 0.54*	≥ 0.36# / 0.33*	0.83# / 0.75*	
		Scaffold analysis	ZO-1 intensity (RFU)	≤ 46# / 55*	≤ 77# / 92*	≤ 97# / 115*	≤ 107# / 128*	107# / 128*	
			Seeding specificity (%)	≤ 43# / 42*	≤ 72# / 70*	≤ 89# / 87*	≤ 99# / 97*	99# / 97*	

## 12.5 Scoring system: subcategories results

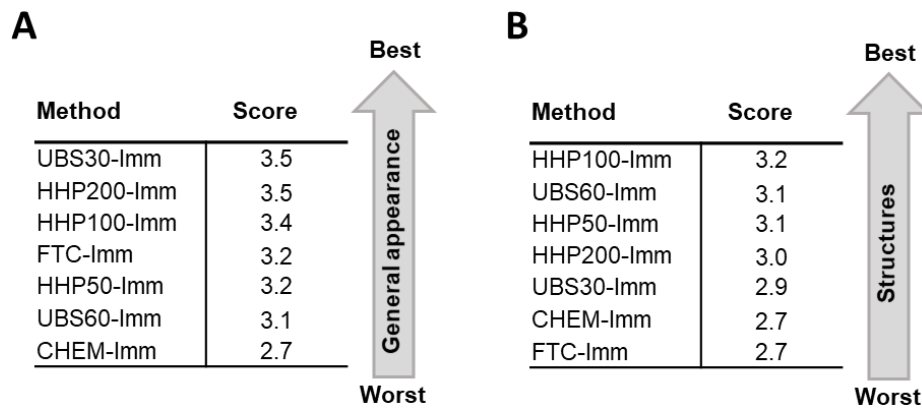


**Figure S 1: Evaluation of histological categories of the scoring system for PCKS-Imm scaffolds.** (A) general appearance category and (B) structures category following decellularization of PCKS-Imm by immersion

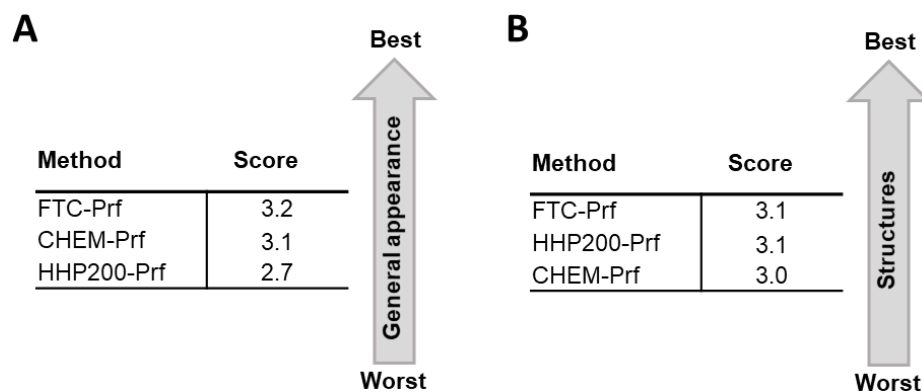


**Figure S 2: Evaluation of histological categories of the scoring system for PCKS-Prf scaffolds.** (A) general appearance category and (B) structures category following perfusion decellularization of whole kidneys

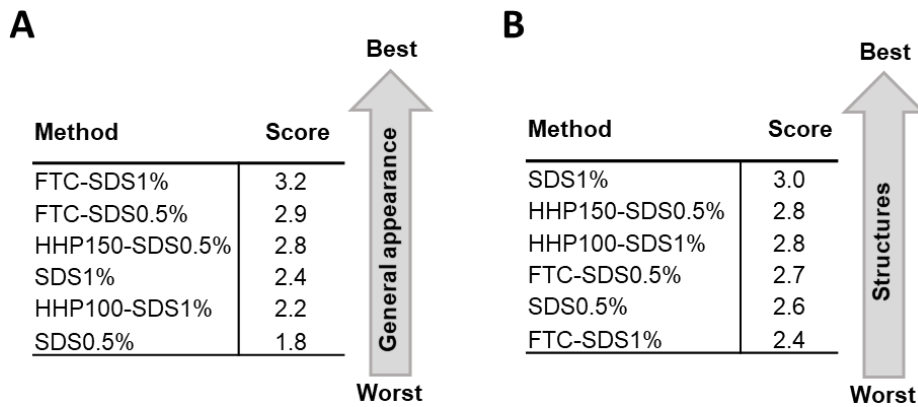


**Figure S 3: Histological categories of the scoring system (direct and indirect approaches).** (A) general appearance category and (B) structures category following perfusion decellularization of whole rat kidneys using the direct and indirect decellularization approaches

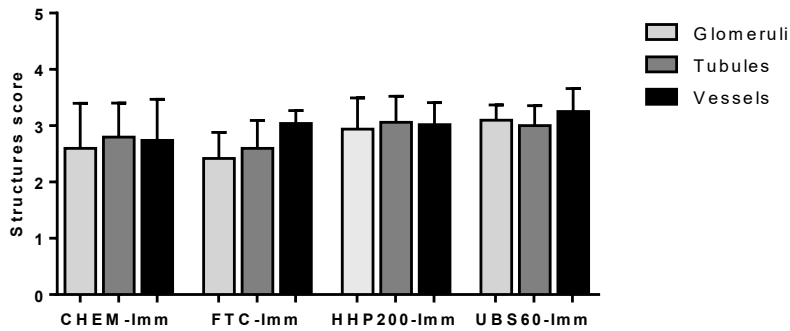


**Figure S 4: Structure scores (histology category) of the scoring system for PCKS-Imm scaffolds** chosen for recellularization. Scores are provided as mean ± SD (n = 4 - 5)

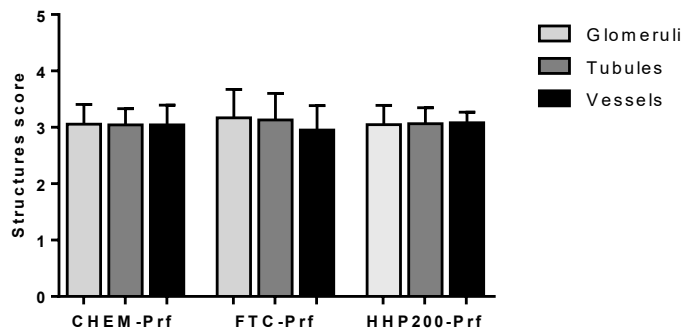


**Figure S 5: Structure scores (histology category) of the scoring system for PCKS-Prf scaffolds** chosen for recellularization. Scores are provided as mean ± SD (n= 6 - 7)

## 12.6 Kidney harvest and perfusion reactor: representative images

### 12.6.1 Kidney harvest

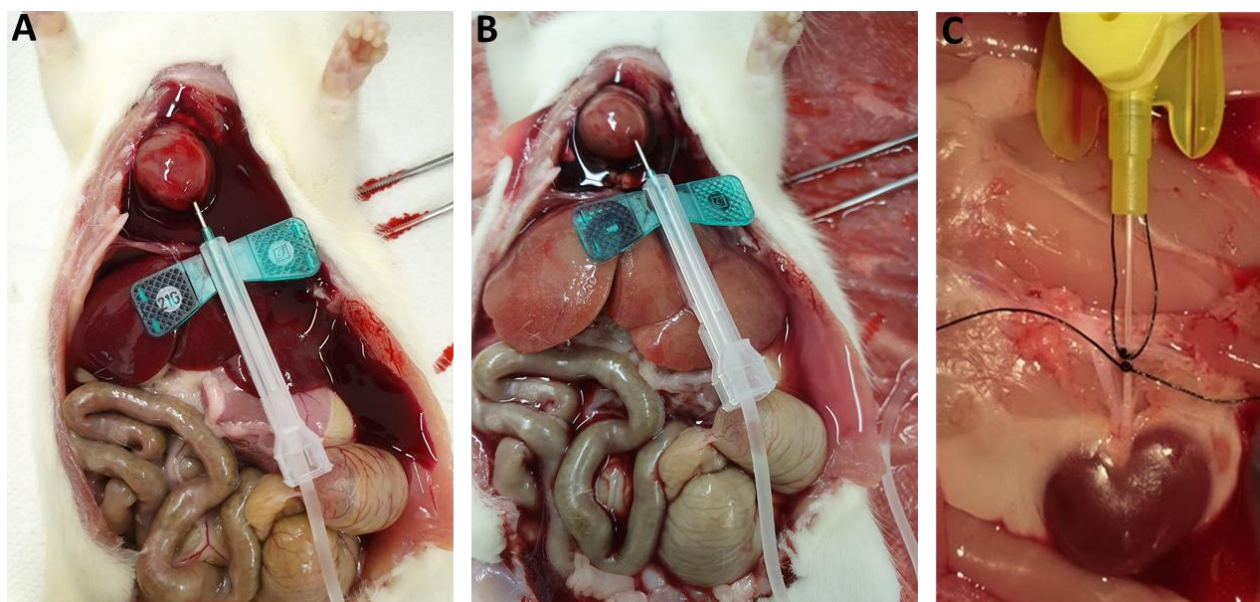


**Figure S 6: Rat kidney harvest and preparation.** (A) The photo shows a butterfly cannula inserted into the left ventricle of the heart for transcatheter perfusion with a heparin in PBS solution (B) Evidence of successful blood removal through transcatheter perfusion is indicated by the reduced red color observed on the liver signifying the displacement of blood from the vascular system through a cut in the right atrium of the heart (not shown) (C) in vivo cannulated kidney

### 12.6.2 Perfusion reactor

The perfusion bioreactor comprises four primary components: a perfusion chamber, a peristaltic pump, a reservoir for chemical reagents, and a reservoir for collecting perfusate (Figure S 7). Each perfusion chamber is a 500 ml laboratory wide-neck glass bottle with a screw cap enabling hose connection. A pair of main hoses is attached to the perfusion chamber: one for perfusion and the other for collecting perfusate. The cannulated kidney within the chamber is linked to the perfusion hose, facilitating the pumping of chemical reagents into the kidney. Simultaneously, the perfusate is gathered through the perfusate hose and directed into the perfusate collection reservoir. Both hoses are integrated into two different channels of the peristaltic pump.

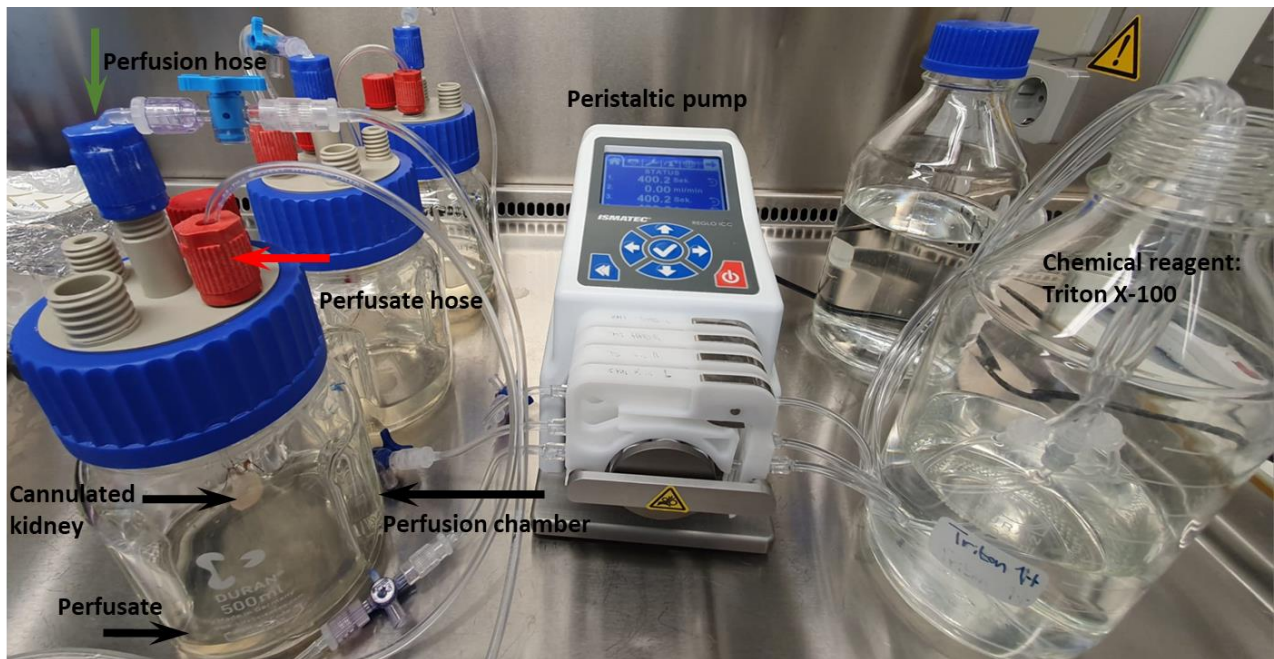


**Figure S 7: Illustration of the perfusion decellularization bioreactor setup during decellularization of three rat kidneys using the FTC-Prf protocol.** The setup includes a perfusion chamber connected to a peristaltic pump. The perfusion chamber includes a perfusion hose (green arrow) through which the chemical reagent is perfused into the cannulated kidney. The perfusate is pumped out from the chamber through the perfusate hose (red arrow) and collected in a glass bottle (not shown) using the peristaltic pump

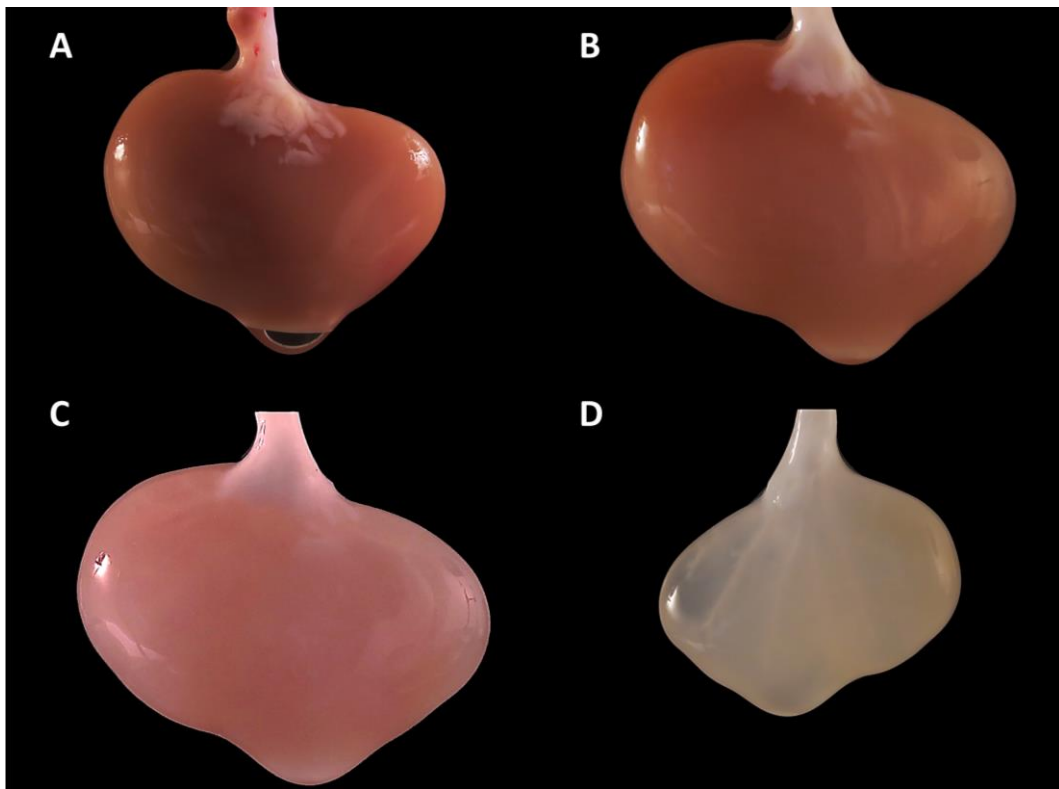


**Figure S 8: Representative images of a whole rat kidney decellularized with the CHEM-Prf protocol after perfusion with: (A) Trypsin, (B) Triton X-100, (C) SDC, (D) SDS**

## 12.7 Further morphological evaluation of the seeded cells with SEM

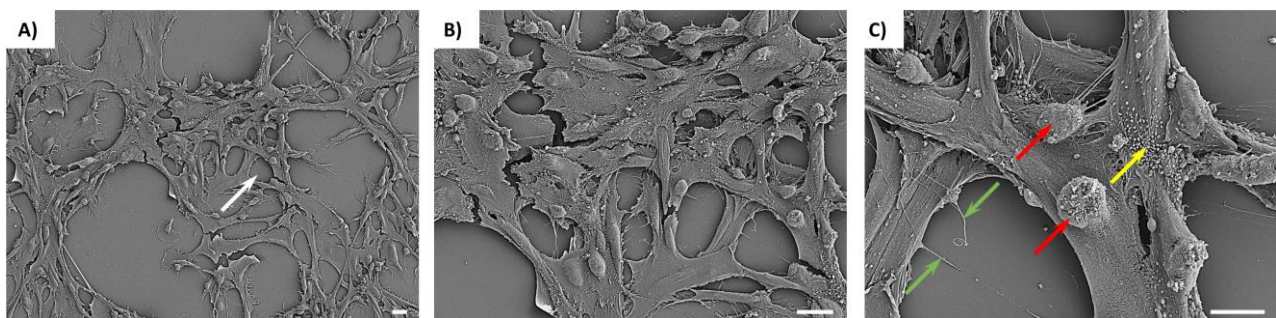


**Figure S 9: SEM of RPTEC/TERT1 cells in 2D (cover glass in 24 well plate).** Representative images are taken from different locations. Magnifications: (A) 200x, (B) 500x and (C) 1500x. The white arrow in image A represents the magnified areas in images B and C. Cells demonstrate a fully extended and flattened shape. Large round structures possibly indicate aggregated cells that are not well seated or are detaching cells (red arrows). Filopodia extending out of the cell body (green arrows) and knob-like, round structures that could be microvilli (yellow arrow). Scale bars: (A) 20  $\mu\text{m}$ , (B) 20  $\mu\text{m}$ , (C) 10  $\mu\text{m}$

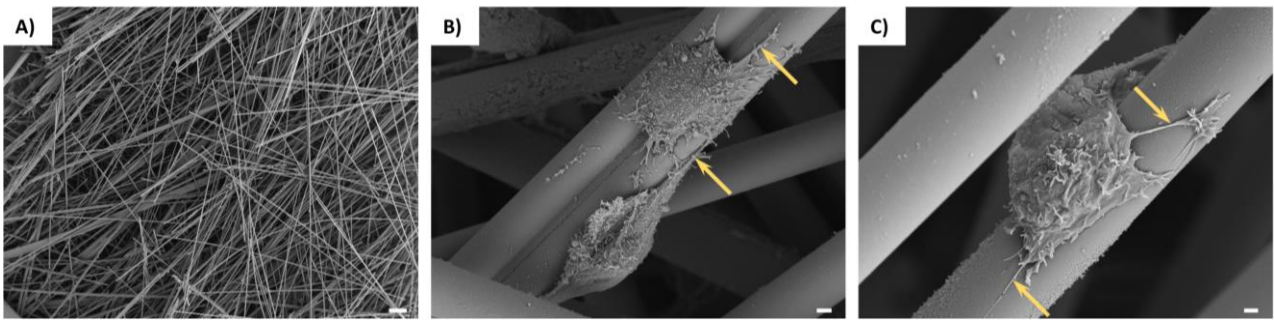


**Figure S 10: SEM of synthetic scaffolds (SYNTH)** made from glass microfibers recellularized with RPTEC/TERT1 cells. Representative images are taken from different locations and three different magnifications: (A) 50x, (B) 2000x and (C) 4000x. (A) Macroscopic depiction of SYNTH scaffolds in a non-magnified image. (B-C) Cells in the seeded state demonstrate a flattened structure. Filopodia extending out of the cell body (yellow arrows). Scale bars: (A) 100  $\mu\text{m}$ , (B) 2  $\mu\text{m}$ , (C) 1  $\mu\text{m}$

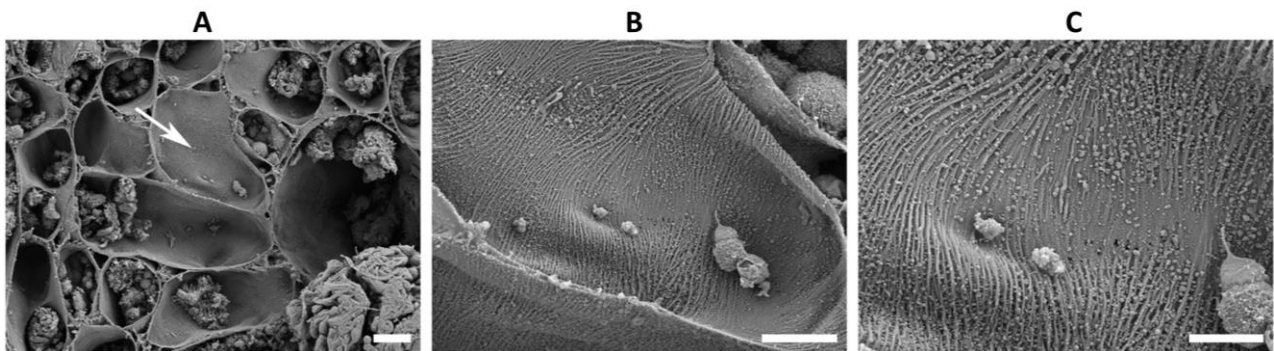


**Figure S 11: SEM of the ultrastructure of the luminal basal membrane** underlying the epithelial cells in the tubules of the native kidney. A representative area of an untreated native kidney slice is shown at three different magnifications: (A) 500x, (B) 1000x and (C) 2000x. The white arrow in image A represents the magnified area in images B and C clearly showing the striated appearance of the tubule walls. Scale bars: (A) 20  $\mu\text{m}$ , (B) 10  $\mu\text{m}$ , (C) 5  $\mu\text{m}$

## 12.8 Resazurin standard curve

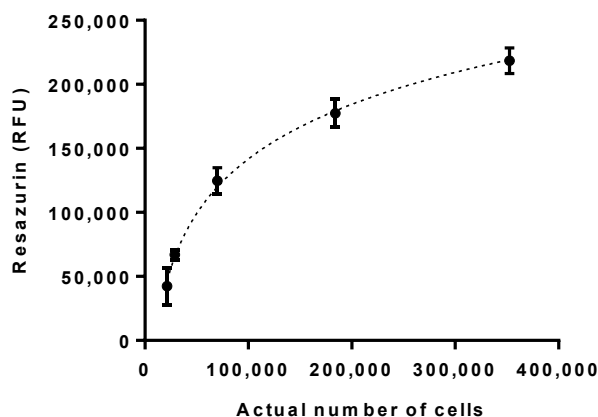


**Figure S 12: Resazurin standard curve showing the logarithmic relationship between fluorescence values and the number of cells.** The logarithmic regression line, determined using GraphPad Prism, demonstrates the growth pattern of the cells. Values are expressed as mean  $\pm$  SD ( $n = 5$ )

## 12.9 Further fluorescence analysis of recellularized scaffolds

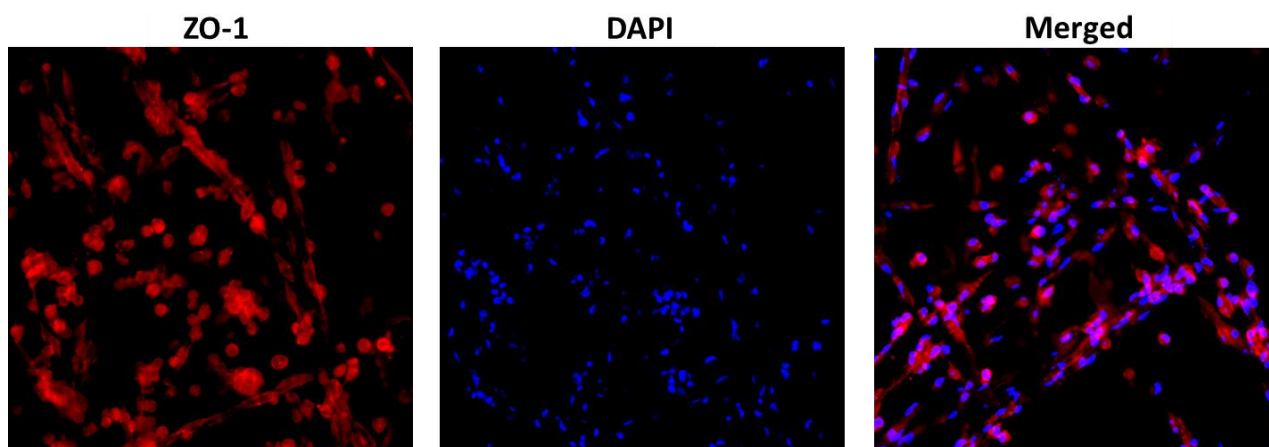


**Figure S 13: Representative images of ZO-1 staining on seeded SYNTH scaffolds.** RPTEC/TERT1 cells on whole mount synthetic scaffolds (SYNTH) stained with ZO-1, demonstrated offering a favorable environment for promoting the production of ZO-1. Anti ZO-1 (red) and DAPI for cell nuclei (blue) are shown individually and merged

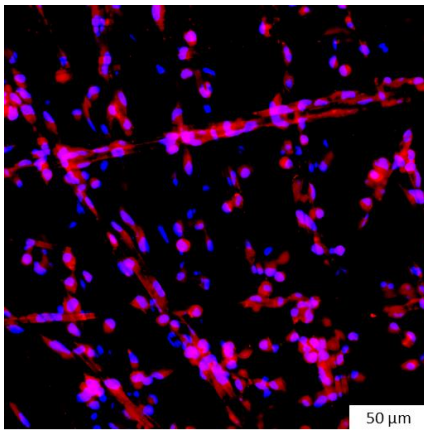


**Figure S 14: Representative images of Col-IV staining on seeded SYNTH scaffolds.** Seeded RPTEC/TERT1 cells on whole mount synthetic scaffolds (SYNTH) stained with Col-IV, showing a non-uniform distribution of cells without distinct alignments resembling kidney functional units. Anti Col-IV (red) and DAPI for cell nuclei (blue) are merged together

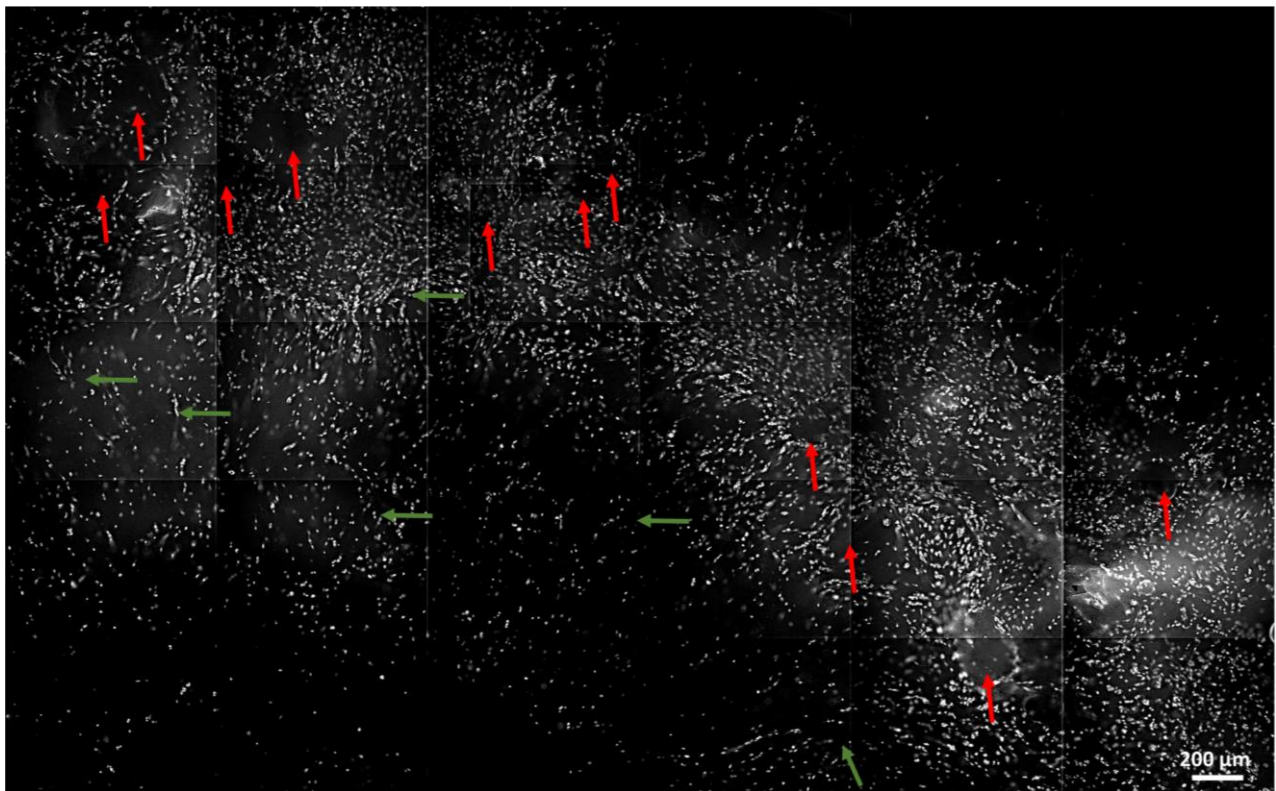


**Figure S 15: RPTEC/TERT1 cells in PCKS-Imm showing distinctive circular cell alignment** in the renal cortex (red arrows) similar to the Bowman capsules, along with linear migration to the medulla (green arrows), resembling collecting duct formation. Whole mount scaffolds were stained with Hoechst 33342 for cell nuclei. Images were captured using WiScan Hermes fluorescence microscope. PCKS-Imm were decellularized using the CHEM-Imm protocol

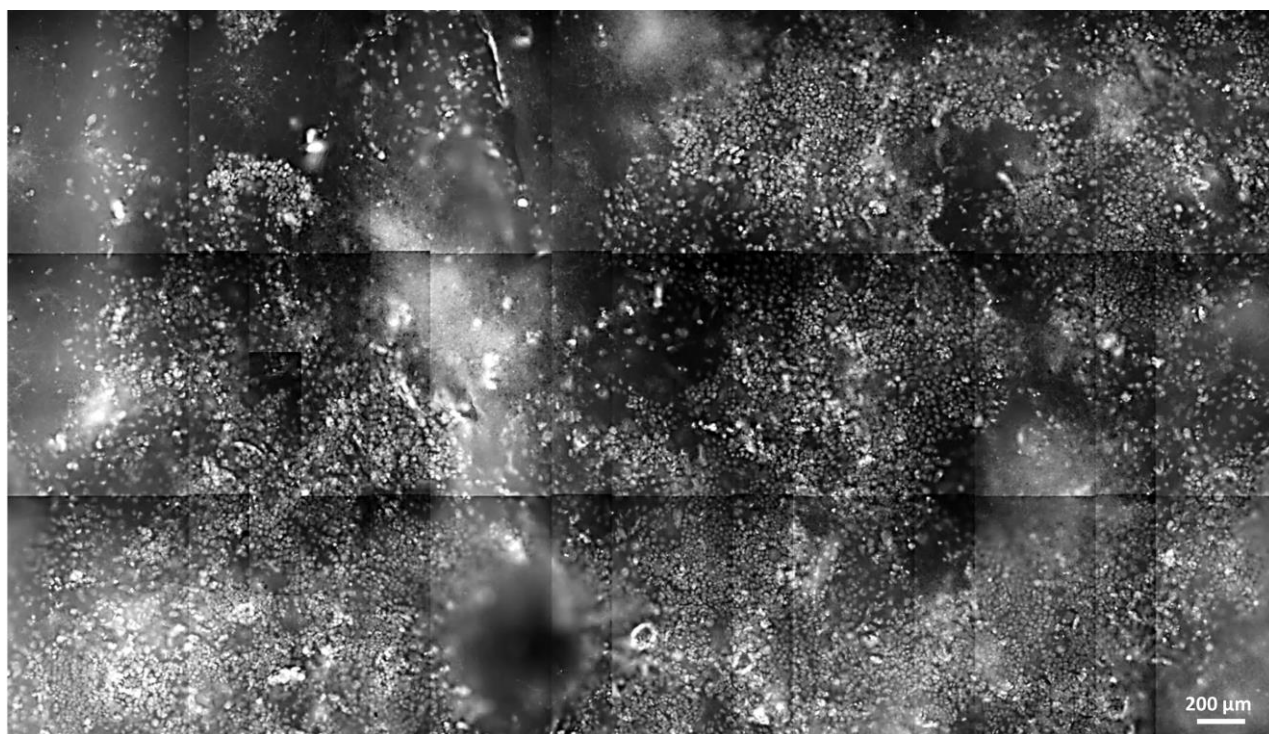


**Figure S 16: Caco-2 (intestinal epithelial cells) in PCKS-Imm did not exhibit cellular alignments** within the scaffold and rather covered mostly the entire scaffold surface. Whole mount scaffolds were stained with Hoechst 33342 for cell nuclei. Images were captured using WiScan Hermes fluorescence microscope. PCKS-Imm were decellularized using the CHEM-Imm protocol

### 12.10 Isolation of peripheral blood mononuclear cells (PBMCs)

PBMCs were isolated from Buffy coats using a protocol that incorporates a density gradient medium and subsequent centrifugation. Initially, 20 ml of Buffy coats was diluted in a 1:1 ratio with 20 ml of PBS and gently layered onto 10 ml of a density gradient medium (Ficoll™). It is imperative to avoid mixing the separation medium with the Buffy coats. Subsequently, the mixture underwent centrifugation at 800 g for 20 min at RT, with careful adjustments to the centrifuge settings (ACC: 3, DEC: 0) to prevent the mixing of distinct phases. During centrifugation, cells with higher density, such as granulocytes and erythrocytes, settled through the density gradient medium. The PBMCs localized at the interface between the density gradient medium and the plasma. Following centrifugation, plasma was removed using a suction pump, and the PBMCs were transferred to a 15 ml tube. The cells underwent three washes with PBS at a 1:2 ratio (7.5 ml of cell suspension and 15 ml of PBS) and were centrifuged at 300 g and RT for 5 min after each wash. After each washing step, the supernatant was discarded. Subsequently, the pellet was resuspended and quantified.

The isolated PBMCs were cryopreserved until their use by storing them in nitrogen at -164 °C. For the cryopreservation process, the PBMCs were aliquoted and centrifuged at 300 g for 5 min and RT. The supernatant was discarded, and the cell pellet was resuspended in a freezing medium consisting of 90% FBS and 10% dimethyl sulfoxide (DMSO).

Thawing of cryopreserved PBMCs was performed in a 37 °C water bath. Following thawing, an initial 1 ml of cell culture thawing medium (RPMI 1640 Medium + 20% FBS) was added to the cells. They were then transferred to 4 ml of culture medium. To eliminate DMSO, the cell suspension underwent centrifugation at 300 g for 5 min at RT. The resulting cell pellet was resuspended in culture medium.

## 13 Acknowledgments

I would like to express my gratitude to everyone who contributed to the success of this work. My special thanks go to Prof. Steffen Mitzner for providing me with the opportunity to pursue my doctoral studies at the department of Extracorporeal Therapy Systems (EXTHER) at Fraunhofer Institute for Cell Therapy and Immunology (IZI). Interesting discussions and thought-provoking insights, played a crucial role in the accomplishment of this work. I also extend my sincere appreciation to Prof. Rainer Bader and Dr. Kirsten Peters, members of the thesis advisory committee for their valuable insights and commitment.

A very special thanks goes to my supervisor Dr. Reinhold Wasserkort for always having an open door for all possible or impossible problems that can arise during a doctoral journey. I appreciate his frequent, sometimes challenging, and seemingly endless but always fruitful discussions on the topic and various matters beyond. These conversations have often shed new perspectives and provided insights that have proven to be crucial to the success of this work. Thank you for your continuous support and valuable contributions during the entire process.

In addition to all those mentioned so far, my gratitude extends to all the staff and colleagues at the EXTHER department. I want to express heartfelt appreciation to the colleagues who provided invaluable assistance when I needed support in developing and establishing crucial methods for this journey: Dr. Jacqueline Hofrichter, Dr. Anne Breitrück and Dr. Sandra Doss. Their support, collective expertise, and collaborative spirit are significant to the success of this work. I am truly grateful for their commitment and the positive impact they have had on the overall success of this project. I would also like to thank Dr. Andreas Körtge for his crucial support in overcoming technical challenges throughout this project.

A special acknowledgment goes to my, Bachelor's and Master's students, Lea Kramer, Sophie-Charlotte Nelz, Sarina Lichtwark and Anna Stender as well as my student assistants Valentine Junge, Nele Karras, Anne Schölzel, Antonia Delft and Louisa Zschenderlein for their valuable contributions and support. Special thanks go to the technical staff, particularly Helga Weiss-Reining.

I would like to extend my gratitude to the entire HOGEMA project consortium team. Special thanks go to Mathias Lorenz (Wismar University of Applied Sciences) for providing us with the ultrasonic

## 13 Acknowledgments

---

bath system (UBS). Additionally, I appreciate Christopher Pohl from (Universitätsklinikum Greifswald) for his invaluable support in establishing the artificial intelligence method.

I express my gratitude to Dr. Anke Hoffmann, Nicole Teßendorf, and Tom Hornemann from the Toxicology and Immuno-toxicology Unit at the Fraunhofer IZI. Their assistance with the histological preparation of paraffin blocks for the decellularized precision-cut kidney slices (PCKS) is greatly appreciated. Additionally, I extend my thanks to Dr. Kristin Reiche and Dr. Markus Kreuz from the Bioinformatics Unit at the same institute for their insightful consultation on statistical analysis.

I extend my appreciation to Prof. Brigitte Vollmar (UMR, Rudolf-Zenker-Institute for Experimental Surgery) for her support in teaching me the technique of cannulating rat kidneys in vivo. I am also grateful to Prof. Robert David (UMR, Regenerative medicine in cardiac surgery) for generously granting me permission to utilize the confocal fluorescence microscope.

I want to express my appreciation to my friends outside the laboratory who provided an escape from the "everyday madness" bringing me back to reality.

I offer my regards and sincere gratefulness to everyone who supported me in any way during the completion of this thesis. To my fiancée, Etaf Abu Zir, your incredible support over the last ten months has been a driving force in completing this thesis. Thank you for standing by me, understanding the demands of this journey, and providing continuous encouragement. Last but not least, I also extend my deepest thanks to my parents, who have been a constant source of support and guidance throughout my entire life, making this journey possible.

## 14 Declaration

Ich versichere hiermit, dass ich die vorliegende Arbeit mit dem Thema:

*Establishment of a Human 3D Kidney Tissue Model Using Decellularized Rat Kidney Slices*

selbstständig verfasst und keine anderen Hilfsmittel als die angegebenen benutzt habe. Die Stellen, die anderen Werken dem Wortlaut oder dem Sinn nach entnommen sind, habe ich in jedem einzelnen Fall durch Angabe der Quelle kenntlich gemacht.

Ich erkläre hiermit weiterhin, dass ich meine wissenschaftlichen Arbeiten nach den Prinzipien der guten wissenschaftlichen Praxis gemäß der gültigen „Regeln zur Sicherung guter wissenschaftlicher Praxis und zur Vermeidung wissenschaftlichen Fehlverhaltens“ an der Universität Rostock angefertigt habe.

Rostock, 04.01.2024

Unterschrift

# Curriculum Vitae

## Education

<b>Doctor of Philosophy (Medical Biotechnology)</b> <i>University Medicine Rostock, University of Rostock</i> Establishment of a Human 3D Kidney Tissue Model Using Decellularized Rat Kidney Slices	<b>04/2019 – 11/2024</b> Rostock, Germany
<b>Master of Science (Life Science Engineering)</b> <i>Friedrich-Alexander-University Erlangen-Nuremberg</i> <b>Master thesis:</b> 1.3 (Very good), awarded a scholarship Development of Seeding Techniques for Scaffolds from Decellularized Muscles	<b>10/2013 – 02/2017</b> Erlangen, Germany
<b>Bachelor of Science (Pharmaceutical-Chemical Engineering)</b> <i>German Jordanian University (GJU)</i> <b>Bachelor thesis:</b> 92% (Excellent), published Implementation of „Cleaner Production“ on the Pharmaceutical Industry in Jordan	<b>10/2005 – 12/2010</b> Amman, Jordan

## Career Accomplishments

<b>Research Scientist, (Post-Doc. since 12/2024)</b> <i>Fraunhofer Institute for Cell Therapy and Immunology (IZI)</i> <ul style="list-style-type: none"><li>Development of a method for enriching uremia toxins using extracellular vesicles</li><li>Development of a liquorpheresis method for enriching Alzheimer-specific proteins</li><li>Networking coordination: promoting internal collaboration</li></ul>	<b>Since 04/2023</b> Rostock, Germany
<b>Research Scientist, Ph.D. candidate</b> <i>Fraunhofer Institute for Cell Therapy and Immunology (IZI)</i> <ul style="list-style-type: none"><li>PhD project: Conducting experimental work to establish the 3D kidney model</li><li>Development of a novel kidney support method (patent submitted)</li><li>Development of a method for the cultivation of liver tissue slices</li></ul>	<b>12/2018 – 03/2023</b> Rostock, Germany
<b>Student assistant</b> <i>Max-Planck-Institute for the Science of Light</i> Monitoring of heterogeneous catalytic reactions within hollow-core photonic crystal fibers (HC-PCF) using absorption spectroscopy	<b>11/2014 – 04/2015</b> Erlangen, Germany
<b>OPERATIONAL EXCELLENCE SENIOR OFFICER</b> <i>Hikma Pharmaceuticals PLC</i> Initiation and development of a new capacity planning model	<b>01/2012 – 09/2013</b> Amman, Jordan
<b>PRODUCTION ENGINEER, FESTE ARZNEIFORMEN</b> <i>Arab Pharmaceutical Manufacturing (Hikma Pharmaceuticals PLC)</i> Initiation of the "Lean Manufacturing" project	<b>02/2011 – 12/2011</b> Sult, Jordan

## Scholarships & Awards

- Poster Prize, PhD Day, Fraunhofer IZI, 2022
- Master thesis scholarship funded by the Bavarian State, 2016
- DAAD Scholarship for two German courses at the University of Bremen and Magdeburg-Stendal University, 2006

## Languages

- English: Fluent
- German: Fluent
- Arabic: Native Language